© Copyright 2019

Alexander J. Baird

Rapid Prediction of Infrastructure Damage and Loss Due to Earthquake-Induced Soil Liquefaction

Alexander J. Baird

A thesis

submitted in partial fulfillment of the

requirements for the degree of

Master of Science in Civil Engineering

University of Washington

2019

Committee:

Brett Maurer

Michael Gomez

Program Authorized to Offer Degree:

Civil and Environmental Engineering

University of Washington

Abstract

Rapid Prediction of Infrastructure Damage and Loss Due to Earthquake-Induced Soil Liquefaction

Alexander J. Baird

Chair of the Supervisory Committee:
Brett Maurer
Civil and Environmental Engineering

Semi-empirical models based on in-situ geotechnical tests have been the standard-of-practice for predicting soil liquefaction since 1971. Recently, geospatial prediction models utilizing free, readily-available data were proposed using satellite remote-sensing to infer subsurface traits without in-situ tests. Using 15,222 liquefaction case-histories from 24 earthquakes, this study assesses the performance of 23 models based on geotechnical or geospatial data using standardized metrics. Uncertainty due to finite sampling of case histories is accounted for and used to establish statistical significance. Geotechnical predictions are significantly more efficient on a global scale, yet successive models proposed over the last twenty years show little demonstrable improvement. In addition, geospatial models perform equally well, or better, for large subsets of the data – a provocative result considering the relative time- and cost-requirements underlying these predictions. Given the demonstrated potential of Geospatial models to predict soil liquefaction, efforts are made to extend the use of these models to also

predict the ensuing infrastructure damage and loss. Towards this end, the present study focuses on structures built atop shallow foundation systems. Utilizing damage-survey data and insurance loss-assessments for 62,000 such assets, functions for predicting liquefaction-induced damage and loss in near real-time are developed.

TABLE OF CONTENTS

LIST OF FIGURES

LIST OF TABLES

ACKNOWLEDGEMENTS

I would first like to thank my thesis advisor Professor Brett Maurer of the Civil and Environmental Engineering department at the University of Washington. Prof. Maurer was always available for questions and to provide guidance during my research and writing. I would also like to thank my other professors and classmates at the University of Washington who were a constant source of support and encouragement.

The presented study is based upon work supported by the National Science Foundation (NSF), US Geological Survey (USGS), and Pacific Earthquake Engineering Research Center (PEER) under Grant Nos. CMMI-1751216, G18AP-00006, and 1132-NCTRBM, respectively. I also wish to acknowledge the numerous researchers who contributed to the liquefaction case-history data studied herein. Much of this data was collected under the sponsorship of either the New Zealand Earthquake Commission (EQC) or one of the three aforementioned organizations. However, any opinions, findings, and conclusions or recommendations expressed in this paper are those of the authors and do not necessarily reflect the views of NSF, USGS, PEER, or EQC.

Chapter 1. INTRODUCTION

Liquefaction is a considerable hazard during an earthquake and is characterized by the reduction or loss of the strength and stiffness of soils induced by earthquake shaking or other rapid loading. The state-of-practice for predicting the occurrence and severity of soil liquefaction at regional-scale presently relies on (a) surficial geology maps that are typically too general to be accurate at site-specific scales; and/or (b) in-situ geotechnical tests that are typically too costly and time-consuming to be feasible over large areal extents. While semi-empirical models based on in-situ geotechnical test have been the standard-of-practice for predicting soil liquefaction since 1971, recent exploratory research has proposed liquefaction prediction-models based on free, remotely-sensed geospatial information. These "geospatial" models rely on satellite remote-sensing to infer subsurface traits without in-situ tests and could transform the assessment of liquefaction hazard by providing an inexpensive and rapid means of predicting hazards. At the same time, recent earthquakes have resulted in unprecedented data for both severity of ground failure due to liquefaction and the resulting infrastructure damage and loss. This study will use the large amount of data collected from the 2010-2016 Canterbury, New Zealand, Earthquake Sequence (CES) to rigorously study the performance of (a) traditional in-situ geotechnical liquefaction models based on cone penetration tests (CPT); and (b) geospatial models based on methods developed by Zhu et al. (2015, 2017). Additionally, the best performing geospatial models will be evaluated for predicting foundation damage and economic losses in the field.

This manuscript will follow the "journal style" with a brief summary of the liquefaction prediction models and methodology of performance analysis, followed by Chapters 2 and 3

covering two journal papers to study the topics discussed above. A brief conclusion will follow at the end with a bibliography and appendix for additional output figures.

1.1 LIQUEFACTION PREDICTION MODELS

Liquefaction prediction models can generally be deliminated in terms of complexity into three tiers: (1) wholly-empirical models that require only geologic or geospatial data and are accessible to a broad userbase (e.g., Youd and Hoose, 1977; Kramer, 2008; FEMA, 2013; Zhu et al., 2017); (T2) semi-mechanistic "simplified stress-based" models that require in-situ measurements and are generally limited to use by geoengineers (e.g., Kayen et al., 2013; Boulanger and Idriss, 2014); and (T3) wholly-mechanistic constitutive models. While "T3" models have grown in their use by geoengineers, they are limited by requirements in knowledge in computational mechanics, uncertainties about model adequacy, interpretation of results, and are still relatively rare in their application to predict liquefaction triggering. This study will focus on "T1" and "T2" models henceforth referred to as "geospatial models" and "geotechnical models".

1.1.1 *Geotechnical Models*

The "geotechnical models" have generally been based on a "simplified stress-based procedure" for evaluating the potential for liquefaction triggering. Generally, they compare an earthquake-induced cyclic stress ratios (CSR) with the cyclic resistance ratios (CRR) of the soil. The CRR is usually correlated to an in-situ soil parameter such as CPT penetration resistance, SPT blow count, or shear wave velocity, V_s. Six such liquefaction triggering models based on the CPT will be used in this study: Robertson and Wride (1998), Architectural Institute of Japan (2001), Moss et al. (2006), Idriss and Boulanger (2008), Boulanger and Idriss (2014), and Green et al. (2018). These models compute a factor of safety against liquefaction by relating CSR to CRR: Factor of Safety

= CRR / CSR. While this provides a simple method to access hazard and is widely used in practice, a further step is required as nearly all existing case-histories simply document whether surface manifestations of liquefaction are observed. Therefore, to evaluate predictions of liquefaction at-depth against surface observation, these six triggering models will be used in series with three separate manifestation models: Iwasaki et al. (1978), van Ballegooy et al. (2014), and Maurer et al. (2015a), who respectively proposed models named *LPI*, *LSN*, and LPI_{ISH}. These geotechnical models are discussed in greater detail in Sections 2.3 and 2.8.

1.1.2 *Geospatial Models*

The "geospatial models" are methods developed to approach regional liquefaction-mapping based on broadly available geospatial parameters which can be derived from satellite remote sensing. The models were advanced considering the relationship between geologic depositional environments and liquefaction susceptibility (Youd and Perkins, 1978). Various geospatial models have been proposed based on exploratory variables used as proxies for earthquake loading, soil density, and soil saturation, such as: peak ground velocity (PGV) from ShakeMap, slope-derived V_{S30}, modeled water table depth, distance to coast, distance to river, distance to the closest water body, and precipitation (Zhu et al., 2015, 2017). These models have also been trained on observations of ground failure and thus inherently combine both liquefaction triggering and manifestation Geospatial models are discussed in greater detail in Sections 2.9 and 3.5.

1.2 ROC Analyses

In order to evaluate the different models' performance, a standardized and objective method is needed to analyze model efficacy (i.e., the ability to predict whether sites have liquefaction manifestations). To this end, receiver-operating-characteristics (ROC) analyses are adopted as they

provide a method to relate the distributions of "positives" (e.g. liquefaction is observed) and "negatives" (e.g. no liquefaction is observed) using the overlap when the frequency of the distributions is expressed as a function of a diagnostic model index (e.g., *LPI*, *LSN*, etc.). In simplest terms, ROC analyses relate the probabilities of the model predicting a true-positive (i.e. manifestation are observed as predicted) and false-positive (i.e. manifestations are predicted but not observed). Further detail on ROC analysis methods are discussed in Section 2.10 and 2.11.

1.3 Fragility and Vulnerability Functions

Once the relative-efficacy of geospatial and geotechnical models has been evaluated, the best performing geospatial models are used to further develop functions for predicting damage and loss for different types of infrastructure. A common method to represent this relation is known as fragility functions, which simply are a mathematical function that expresses the probability that some undesirable event occurs (i.e., liquefaction manifestation reaches a limit state: minor, moderate, or severe) as a function of some measure of environmental excitation or capacity of an asset (i.e. LPI, LSN, etc.). Conversely, when a degree of loss (i.e. repair costs, life-safety impacts, or loss of functionality) is measured as a function of environmental excitation, the function can be called a vulnerability function. These two terms should not be confused, vulnerability functions measures losses while fragility functions measure a probability of occurrence. These functions are discussed in further detail in Sections 3.11 and 3.12.

Chapter 2. FIELD ASSESSMENT OF LIQUEFACTION PREDICTION MODELS BASED ON GEOTECHNICAL VS. GEOSPATIAL DATA, WITH LESSONS FOR EACH

2.1 INTRODUCTION

Semi-empirical models based on in-situ geotechnical tests have been the standard-of-practice for predicting soil liquefaction since 1971. More recently, prediction models based on free, readily-available data were proposed. These "geospatial" models rely on satellite remote-sensing to infer subsurface traits without in-situ tests. Using 15,222 liquefaction case-histories from 24 earthquakes, this study assesses the performance of 23 models based on geotechnical or geospatial data using standardized metrics. Uncertainty due to finite sampling of case histories is accounted for and used to establish statistical significance. Geotechnical predictions are significantly more efficient on a global scale, yet successive models proposed over the last twenty years show little demonstrable improvement. In addition, geospatial models perform equally well for large subsets of the data – a provocative finding given the relative time- and cost-requirements underlying these predictions. Through this performance comparison, lessons for improving each class of model are elucidated.

2.2 BACKGROUND

Since the inception of the so-called "simplified stress-based procedure" for predicting liquefaction triggering (Seed & Idriss, 1971; Whitman, 1971), variants based on several in-situ geotechnical measurements have been developed. These include cone penetration test (CPT) indices, standard penetration test (SPT) blow counts, and shear-wave velocity (Vs), among others.

In conjunction with such measurements, “simplified” liquefaction triggering models have been used in virtually every seismic zone on Earth. The outputs from these triggering models are also often used cooperatively with other models that predict surface manifestations, such as ground settlement (e.g., Cetin et al., 2009), lateral spreading (e.g., Zhang et al., 2004), liquefaction ejecta (e.g., Maurer et al., 2017), and foundation movements (e.g., Bray and Macedo, 2017; Bullock et al., 2018). While this approach to modelling liquefaction occurrence and consequence is popular worldwide, it requires field measurements that can be costly and time consuming to perform, especially over large areal extents. More recently, “geospatial” models were proposed to predict liquefaction using data that is freely available via satellite remote-sensing (Zhu et al., 2015, 2017). Like the aforementioned geotechnical approach, geospatial models characterize liquefaction demand using common ground-motion intensity measures (IMs). But, in lieu of characterizing liquefaction resistance via in-situ measurements, geospatial models use surface parameters to infer subsurface traits. Examples of such parameters include surface slope, mineralogy, roughness, and wetness; distance to and elevation above rivers, streams, and other water bodies; and compound-topographic-index, which can all be derived from satellite data. Geospatial models are particularly suited for applications in which time- and cost-considerations outweigh the required, expected model accuracy (e.g., regional earthquake simulations; planning and policy development; post-event response and reconnaissance; and hazard assessments in regions that lack geotechnical test equipment). Implicit to this statement, of course, is the assumption that geotechnical models are more accurate than geospatial models. But are they?

The efficacies of these two model classes (i.e., geotechnical and geospatial) have not been directly compared using a consistent set of case histories and standardized performance metrics. Such an assessment could: (1) elucidate pathways to improve each model class (i.e., what can each

class teach the other?); (2) provide a baseline for measuring future improvements; and (3) inform ensemble-modeling approaches that statistically coalesce multiple predictions (e.g., Bradley et al., 2018). In addition, while numerous "simplified" geotechnical models have been proposed over the last twenty years, the popular question of "which model performs best?" remains contentious – the answer obscured, in part, by prior paucity and inconsistency of test cases, as well as use of differing, non-standard, non-objective performance metrics. Further, though often ignored, the performance of any model is intimately tied to the site-specific consequences, or "economies" of misprediction. We should thus ask not only "which model performs best?" but also "which model performs best for particular misprediction economies?"

Accordingly, the objective of this study is to rigorously assess and compare the performance of 18 geotechnical models and 5 geospatial models using a total of 15,222 liquefaction case-histories compiled from 24 earthquakes in 9 countries. As part of this assessment, standardized and objective metrics will be used to evaluate model performance, both in an overall, comprehensive sense, as well as for particular misprediction economies that may be encountered.

2.3 GEOTECHNICAL AND GEOSPATIAL LIQUEFACTION MODELS

The hierarchy of liquefaction prediction-models may be loosely defined by three tiers: (T1) wholly-empirical models that require only geologic or geospatial data and are accessible to a broad userbase (e.g., Youd and Hoose, 1977; Kramer, 2008; FEMA, 2013; Zhu et al., 2017); (T2) semi-mechanistic "simplified stress-based" models that require in-situ measurements and are generally limited to use by geoengineers (e.g., Kayen et al., 2013; Boulanger and Idriss, 2014); and (T3) wholly-mechanistic constitutive models, which typically require many soil and model parameters, and which are generally limited to use by geoengineers trained in computational mechanics (e.g., Cubrinovski and Ishihara, 1998; Byrne et al., 2004; Ziotopoulou and Boulanger, 2016). While

advances to "T3" models and the enabling technologies have grown their use, their application to predicting liquefaction triggering remains relatively rare. This is due to the required inputs and operator skill, but also to uncertainties about model adequacy and the interpretation of results (NRC, 2016). As such, these models are not evaluated in this study, but are mentioned to provide proper context to the assessment of "T1" and "T2" models that is presented herein.

For brevity, the "T2, simplified stress-based models" are henceforth referred to as "geotechnical models." Six such liquefaction triggering models will be used in this study: Robertson and Wride (1998), Architectural Institute of Japan (2001), Moss et al. (2006), Idriss and Boulanger (2008), Boulanger and Idriss (2014), and Green et al. (2018). All six are based on the CPT, which offers significant advantages over other in-situ tests (NRC, 2016). However, because triggering models predict liquefaction at-depth within a soil profile, an evaluation of their performance requires direct investigation of the subsurface (i.e., to assess the agreement between predicted and actual responses in various strata). This might be accomplished proactively using downhole instrument-arrays (e.g., Holzer et al., 2007) or reactively using vision penetrometers (Raschke and Hryciw, 1997) or geoslicers (Nakata and Shimazaki, 1997). Yet, such investigations are generally expensive, exceedingly rare, and may not result in definitive interpretations (e.g., Takada and Atwater, 2004). Thus, nearly all existing case-histories simply document whether manifestations of liquefaction were observed at the surface. Accordingly, to evaluate predictions of liquefaction at-depth against surface observations, the six triggering models will each be used in series with three separate manifestation models: Iwasaki et al. (1978), van Ballegooy et al. (2014), and Maurer et al. (2015a), who respectively proposed models named *LPI*, *LSN*, and LPI_{ISH}. It must therefore be understood that "geotechnical model" refers to the combined use of a liquefaction triggering model with a liquefaction manifestation model. There is simply no practical

or objective way to isolate and assess the independent performance of triggering models. While *LPI*, *LSN*, and LPI_{ISH} were each proposed as general "ground failure" predictors, they have been calibrated almost exclusively on the observed occurrence or nonoccurrence of liquefaction ejecta.

The 18 CPT-based geotechnical models (6 triggering models · 3 manifestation models) will be tested against the performance of 5 "T1" geospatial models. While several types of "T1" model exist, those of Zhu et al. (2015, 2017) are arguably the most rigorously-formulated and well-trained to date; they were also recently implemented into US Geological Survey (USGS) post-earthquake data products to provide automated content on possible earthquake impacts (e.g., Allstadt et al., 2019). These models were trained on observations of ground-failure and thus inherently merge liquefaction triggering and manifestation. Three of the five models to be assessed are region specific - developed specifically for Canterbury, New Zealand – and will be referred to as regional geospatial models (RGMs). The remaining two were trained on successively larger datasets from global earthquakes and will be referred to as global geospatial models (GGMs). A summary of the 23 models to be evaluated, and the symbols henceforth used to identify them, is provided in Table 2.1. Additional model details are provided subsequently in the *Methodology*.

Table 2.1 Summary of Geotechnical and Geospatial Liquefaction Models Evaluated in this Study

Geotechnical Models (18)				**Geospatial Models (5)**	
Triggering Model	**Symbol**	**Manifestation Model**	**Symbol**	**Triggering/Manifestation Model**	**Symbol**
Robertson & Wride (1998)	RW98	Iwasaki et al. (1978)	*LPI*	Zhu et al. (2015) Regional 1	*RGM1*
Arch. Institute Japan (2001)	AIJ01			Zhu et al. (2015) Regional 2	*RGM2*
Moss et al. (2006)	Mea06	van Ballegooy et al. (2014)	*LSN*	Zhu et al. (2015) Regional 3	*RGM3*
Idriss & Boulanger (2008)	IB08				
Boulanger & Idriss (2014)	BI14	Maurer et al. (2015a)	LPI_{ISH}	Zhu et al. (2015) Global	*GGM1*
Green et al. (2018)	Gea18			Zhu et al. (2017) Global	*GGM2*

2.4 DATA

This study analyzes 15,222 liquefaction case histories resulting from 24 earthquakes, as summarized in Table 2.2. However, because a majority of these cases were compiled from three earthquakes in the Canterbury region of New Zealand, results are separately presented for these and the other 21 earthquakes, henceforth respectively referred to as the "Canterbury dataset" and "global dataset." The details of these case-history datasets are discussed next.

Table 2.2 Summary of Liquefaction Case Histories Analyzed

Date	Earthquake	Country	Magnitude (M_w)	Number of Case Histories
16/6/1964	Niigata	Japan	7.60	3
9/2/1971	San Fernando	USA	6.60	2
4/2/1975	Haicheng	China	7.00	2
27/7/1976	Tangshan	China	7.60	10
15/10/1979	Imperial Valley	USA	6.53	7
9/6/1980	Victora (Mexicali)	Mexico	6.33	5
26/4/1981	Westmoreland	USA	5.90	9
26/5/1983	Nihonkai-Chubu	Japan	7.70	2
28/10/1983	Borah Peak	USA	6.88	3
2/3/1987	Edgecumbe	New Zealand	6.60	23
24/11/1987	Elmore Ranch	USA	6.22	2
24/11/1987	Superstition Hills	USA	6.54	8
18/10/1989	Loma Prieta	USA	6.93	67
17/1/1994	Northridge	USA	6.69	3
16/1/1995	Hyogoken-Nambu	Japan	6.90	21
17/8/1999	Kocaeli	Turkey	7.51	16
20/9/1999	Chi-Chi	Taiwan	7.62	34
8/6/2008	Achaia-Ilia	Greece	6.40	2
4/4/2010	El Mayor-Cucapah	Mexico	7.20	3
4/10/2010	Darfield	New Zealand	7.10	5371
22/2/2011	Christchurch	New Zealand	6.20	4806
11/3/2011	Tohoku	Japan	9.00	7
20/5/2012	Emilia	Italy	6.10	45
14/2/2016	Christchurch	New Zealand	5.70	4771
			Total	**15,222**

2.5 CANTERBURY EARTHQUAKE DATASET

Earthquakes occurring over the last decade in the Canterbury region of New Zealand have resulted in case-history data of unprecedented quantity and quality. A comprehensive summary of these earthquakes, to include tectonic and geologic settings, seismology, and effects, is provided

by Quigley et al. (2016). The present study compiles case-histories from the Mw7.1, 4 Sept. 2010 Darfield earthquake, the Mw6.2, 22 Feb. 2011 Christchurch earthquake, and the Mw5.7, 14 Feb. 2016 Christchurch (or "Valentine's Day") earthquake. This effort built upon a series of successive compilations (Maurer et al., 2014a, 2015b, 2019), augmenting the largest of these by more than 50% and resulting in a total of 14,948 case histories. These consist of classifications of liquefaction manifestations, ground-motion intensity measures, geotechnical and hydrological data, and readily available geospatial information. These components are succinctly summarized as follows.

2.5.1 *Liquefaction Manifestations*

All liquefaction models will be evaluated on their abilities to predict free-field surface manifestations on level ground – specifically liquefaction ejecta - rather than any other indicator, such as evidence from ground-motions, foundation movements, or lateral spreading. Sites with these indicators were expressly removed from the study because the models to be evaluated are not intended to predict them. Observations of the occurrence and severity of liquefaction ejecta were compiled by the authors following each of the three earthquakes and classified as "none," "minor," "moderate," and "severe" using criteria from Green et al. (2014). This was accomplished using ground-reconnaissance reports and high-resolution satellite imagery compiled in the New Zealand Geotechnical Database (CERA, 2012). Cases in which manifestations could not be reliably classified are not included in this study. To facilitate model assessment, the cases are reclassified binomially as "No Manifestation" and "Manifestation," where the latter are sites with at least "minor" manifestations per Green et al. (2014). Of the resulting 14,948 case histories compiled from Canterbury, 65% are "No Manifestation" and 35% are "Manifestation."

2.5.2 *Ground-Motion Intensity Measures*

The 23 liquefaction models use either peak ground acceleration, *PGA* (all geotechnical models and some geospatial models) or peak ground velocity, *PGV* (some geospatial models). For this study, *PGA*s were estimated with the Bradley (2013) procedure, which has been used in previous Canterbury earthquake research (e.g., Maurer et al., 2014b; van Ballegooy et al. 2015), and which geostatistically merges *PGA*s recorded at strong-motion stations with *PGA*s estimated by ground-motion prediction equations. *PGV*s were estimated using USGS ShakeMap (Worden and Wald, 2016), consistent with the formulation of geospatial liquefaction models that use *PGV*. While other methods for estimating these IMs are available, a prior analysis of alternatives (Baird et al., 2018) indicates the findings of this study should be unaffected by the methods adopted here.

2.5.3 *Geotechnical, Geospatial, and Hydrological Data*

This study analyzes CPT soundings available in the New Zealand Geotechnical Database (CERA, 2012) and performed at sites where liquefaction manifestations were classified as described above. In the process of compiling case-histories, CPTs were rejected: (1) if the depth of "pre-drill" significantly exceeded the depth of the ground water table; and (2) if inferred to have prematurely terminated on shallow gravels from a geospatial autocorrelation analysis (Anselin, 1995). Prior to processing, CPT tip- and sleeve-measurements were aligned using cross-correlation (Buck et al., 2002). Extended coverage of CPT data and the exclusion criteria summarized above is provided in Maurer et al. (2014a, 2015b). Ground water table (GWT) depths were sourced from the robust, event-specific regional models of van Ballegooy et al. (2014). These models, which reflect seasonal and localized fluctuations across the region, were derived using monitoring data from ~1000 piezometers and provide a best-estimate of GWT depths immediately prior to each earthquake. Various geospatial parameters – to be identified subsequently in the *Methodology* –

were computed at each case-history location following the exact methods of Zhu et al. (2015; 2017) (i.e., the developer of the geospatial models to be evaluated).

2.6 GLOBAL EARTHQUAKE DATASET

To compare findings in Canterbury with regions worldwide, 274 liquefaction case histories are compiled from 21 global earthquakes and assessed in parallel. These cases are sourced from the literature, to include observations of manifestation severity, CPT soundings, and estimation of GWT depth and ground-motion IMs, as generally reported by original investigators. When available, recent refinements are adopted from the literature. Whereas liquefaction was intensively cataloged via reconnaissance and remote sensing in Canterbury, the global cases are often documented in less detail, occasionally with scant information about the nature or severity of expression. Accordingly, while the same criteria (Green et al., 2014) were used to binomially classify manifestations based on ejecta (while excluding cases with other indicators of liquefaction), there is inevitably some uncertainty. Of the 274 global cases, 58% are "Manifestation" and 42% are "No Manifestation." To properly recognize all sources of data used to compile this dataset, a reference list appears in the Appendix, parsed by earthquake; a table of relevant data for each case-history is also provided in an electronic supplement. In this regard, the case history assemblages of Moss et al. (2005) and Boulanger and Idriss (2014) are acknowledged for greatly assisting the present study. Lastly, various geospatial parameters (identified in the *Methodology*) – were computed at each case-history location per Zhu et al. (2015; 2017).

2.7 METHODOLOGY

The 23 liquefaction models to be evaluated in this study were identified in Table 1. Additional model details are now presented, followed by methods that will be used to analyze performance.

2.8 GEOTECHNICAL MODEL METHODOLOGY

CPTs were analyzed for each of the 15,222 case histories using six triggering models, all of which compute factor-of-safety against liquefaction (FS_{liq}) vs. depth. While the reader is referred to the model publications for complete details, two facts pertinent to this study are as follows. First, prior to using any of the six models, liquefaction-susceptible soils were inferred from the CPT soil-behavior-type index (I_c) (Robertson and Wride, 1998), such that soils with $I_c < 2.50$ were assumed susceptible. This criterion was developed specifically for Christchurch soils from lab tests on more than 2,500 samples (Maurer et al., 2019). However, because an I_c threshold of 2.50 is within the range of generic values commonly used in practice (i.e., 2.4-2.6), this criterion is also used in all analyses of the global dataset. Second, for liquefaction-susceptible soils, the IB08, BI14, and Gea18 models compute liquefaction resistance as a function of fines-content (*FC*). Accordingly, *FC* was estimated for the Canterbury dataset using a Christchurch-specific $I_c - FC$ correlation (Maurer et al., 2019), and for the global dataset using a generic $I_c - FC$ correlation (Boulanger and Idriss, 2014), with the former estimating *FC* to be ~10% higher for a given I_c.

Next, the outputs from triggering analysis were input to the *LPI*, *LSN*, and LPI_{ISH} manifestation models. The Liquefaction Potential Index (*LPI*) is defined as (Iwasaki et al., 1978):

$$LPI = \int_0^{20\,m} F(FS_{liq}) \cdot w(z)\,\mathrm{d}z \tag{2.1}$$

where $F(FS_{liq})$ and $w(z)$ are functions that weight the respective influences of FS_{liq} and depth, z, on surface manifestation. Specifically, $F(FS_{liq}) = 1 - FS_{liq}$ for $FS_{liq} \leq 1$ and $F(FS_{liq}) = 0$ otherwise; $w(z) = 10 - 0.5z$. Thus, *LPI* assumes that surface manifestation depends on the thickness of all liquefied strata in a profile's upper 20 m, their proximity to the ground surface, and the amount by which FS_{liq} in each stratum is less than 1.0. Given this definition, *LPI* can range from zero to 100.

A modified *LPI* was proposed by Maurer et al. (2015a) and inspired by Ishihara (1985), who recognized the role of the non-liquefied capping stratum, or "crust," on suppressing surface manifestations. Using data from Japanese earthquakes, Ishihara (1985) proposed limit-state curves for binomially predicting manifestations as a function of the crust thickness (H_1), among other factors. Using these curves, Maurer et al. (2015a) modified *LPI* to better capture the observed influence of H_1. In consideration of its provenance, the result was termed LPI_{ISH} and is defined by:

$$LPI_{ISH} = \int_{H_1}^{20\ m} F(FS_{liq}) \cdot w(z)\ \mathrm{d}z \tag{2.2}$$

where

$$(FS_{liq}) = \begin{cases} 1 - FS_{liq} & if\ FS_{liq} \leq 1\ \cap\ H_1 \cdot m(FS_{liq}) \leq 3 \\ 0 & otherwise \end{cases} \tag{2.3}$$

$$m(FS_{liq}) = \exp\left(\frac{5}{25.56(1-FS_{liq})}\right) - 1 \tag{2.4}$$

In Eq. (2.2), $F(FS_{liq})$ and $w(z)$ have the same objective as in *LPI*, but are functionally different, such that $F(FS_{liq})$ accounts for the crust thickness via the parameter H_1 and $w(z)$ is defined by $w(z) = 25.56 \cdot z^{-1}$. Maurer et al. (2015a) recommended a minimum H_1 of 0.4 m be used, even if liquefiable soils are present at shallower depths. Given this constraint, LPI_{ISH} can range from zero to 100.

The Liquefaction Severity Number (*LSN*) is an adaptation of methods for estimating post-liquefaction volumetric strain (e.g., to predict ground settlement), modified to include a power-law depth weighting function (van Ballegooy et al., 2014):

$$LSN = \int_0^{20\ m} \varepsilon_v \cdot w(z)\ \mathrm{d}z \tag{2.5}$$

where ε_v is post-liquefaction volumetric strain (%) and $w(z) = 10 \cdot z^{-1}$. For a given value of FS_{liq}, ε_v is inversely related to the soil's initial relative density (D_r). By corollary, and assuming ε_v a sufficient index of liquefaction response, surface manifestations should diminish as the D_r of

liquefying soil increases. While there are several approaches to estimating ε_v (Geyin and Maurer, 2019a), van Ballegooy et al. (2014) used that of Zhang et al. (2002), which we thus also adopt. *LSN* values can far surpass 100 when liquefiable soils are present at the immediate surface, but typically are between zero and 100. These values are not quantities of predicted ground settlement, but rather, are index values á la *LPI* and LPI_{ISH} that correlate to the likelihood of surface manifestation.

2.9 GEOSPATIAL MODEL METHODOLOGY

The five geospatial models have the general form $P(X) = (1 + e^{-X})^{-1}$ where X is a series of geospatial variables and model coefficients, and $P(X)$ is the likelihood of surface manifestation. In conjunction with this equation, the three region-specific and two global geospatial models are defined in Table 2.3. The variables are as follows: PGA_M = magnitude-weighted peak ground acceleration (g) using the weighting of Youd et al. (2001); *PGV* = peak ground velocity (cm/s); d_{r3} = distance (km) to a stream of order three or greater (Strahler, 1952); V_{s30} = shear-wave velocity of the upper 30-m (m/s), inferred from surface topography (Wald and Allen, 2007); d_r = shortest distance to a river (km) cataloged by Lehner et al. (2006); *CTI* = compound topographic index (Beven and Kirkby, 1979); d_c = distance to coast (km); *precip* = mean annual precipitation (mm) (Fick and Hijmans, 2017); *ND* = d_c divided by the distance from the coast to the edge of the sedimentary basin; and *wtd* = water table depth (m). *GGM2* has variants for coastal and noncoastal locations, the distinguishing threshold being d_c = 20 km. All variables were computed in accordance with Zhu et al. (2015; 2017), to which the reader is referred for additional information.

Table 2.3. Geospatial Liquefaction Model Equations

Model	***Model Parameter X***
RGM1	$2.053 + 1.267 \cdot \ln(PGA_M) - 0.239 \cdot d_{r3} - 9.191 \cdot ND$
RGM2	$0.316 + 1.225 \cdot \ln(PGA_M) + 0.145 \cdot CTI - 9.708 \cdot ND$
RGM3	$25.45 + 2.476 \cdot \ln(PGA_M) - 0.323 \cdot d_{r3} - 4.241 \cdot \ln(V_{s30})$
GGM1	$24.10 + 2.067 \cdot \ln(PGA_M) + 0.355 \cdot CTI - 0.4784 \cdot \ln(V_{s30})$
GGM2 (Coastal)	$12.435 + 0.301 \cdot \ln(PGV) - 2.615 \cdot \ln(V_{s30}) + 5.556 \times 10^{-4} \cdot precip - 0.0287 \cdot (d_c)^{0.5} + 0.0666 \cdot d_r - 0.0369 \cdot d_r \cdot (d_c)^{0.5}$
GGM2 (Inland)	$8.801 + 0.334 \cdot \ln(PGV) - 1.918 \cdot \ln(V_{s30}) + 5.408 \times 10^{-4} \cdot precip - 0.2054 \cdot d_w - 0.0333 \cdot wtd$

2.10 PERFORMANCE-EVALUATION METHODOLOGY

Standardized and objective methods are needed to analyze model efficacy (i.e., the ability to predict whether sites have liquefaction manifestations). Receiver-operating-characteristic (ROC) analyses, which are widely used in biostatistics and medical diagnostics (e.g., Fawcett, 2006; Zou, 2007) are adopted for this purpose. In any ROC analysis, the distributions of "positives" (e.g., liquefaction manifestation is observed) and "negatives" (e.g., no liquefaction manifestation is observed) overlap when the frequency of the distributions is expressed as a function of a diagnostic model index (e.g., *LPI*, *LSN*, etc.). To demonstrate, two such distributions are shown in Figure 2.1a, plotted as a function of *LPI*. ROC curves plot the rates of true-positive predictions (R_{TP}) (i.e., manifestations are observed as predicted) and false-positive predictions (R_{FP}) (i.e., manifestations are predicted but not observed) as a function of model-index "thresholds." These thresholds are used to predict outcomes, such that model values above and below a threshold are respectively predicted to be positive and negative outcomes. Figure 2.1b illustrates the relationship among the positive and negative distributions, the threshold values, and the ROC curve. Low thresholds result in a high R_{FP}, while high thresholds result in a low R_{TP}, equivalent to a high rate of false-negative predictions (R_{FN}), where $R_{FN} = 1 - R_{TP}$. In general, neither of these situations is desirable.

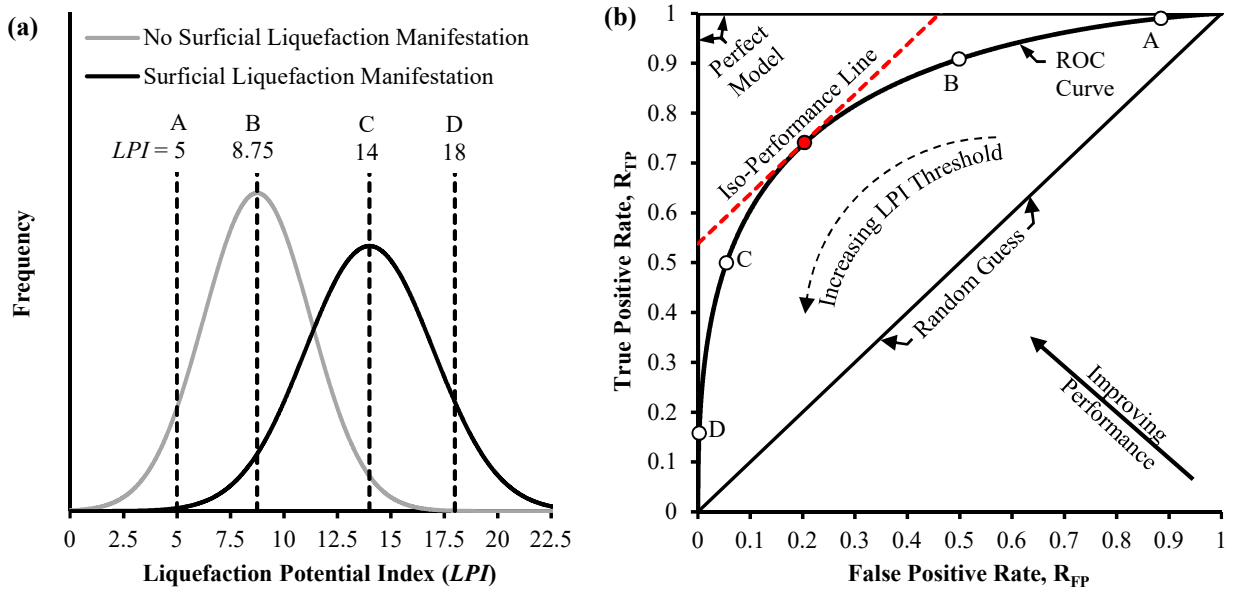

Figure 2.1. ROC analyses: (a) frequency distributions of liquefaction manifestation and no liquefaction manifestation as a function of *LPI*; (b) corresponding ROC curve, and illustration of how a ROC curve is used to assess the efficiency of a diagnostic test.

The optimum threshold may be defined as that which minimizes the prediction cost:

$$Cost = C_{FP} \text{ x } R_{FP} + C_{FN} \text{ x } R_{FN} \tag{2.6}$$

where C_{FP} and R_{FP} are respectively the cost and rate of false-positive predictions and C_{FN} and R_{FN} are respectively the cost and rate of false-negative predictions. Examples of false-positive costs include superfluous spending on design and construction (e.g., ground improvement costs), while false-negative costs are those resulting from liquefaction (e.g., property damage and lost productivity, among others). Normalizing by C_{FN}, Eq. 2.6 is alternatively expressed as:

$$\text{Cost'} = Cost/C_{FN} = R_{FP} \text{ x } CR + R_{FN} \tag{2.7}$$

where $CR = C_{FP}/C_{FN}$ and is the "cost ratio" representing different misprediction economies. Low-*CR* scenarios with are those where the costs of liquefaction far outweigh the costs of mitigation (e.g., a critical facility), while high-*CR* scenarios are those where the costs of mitigation far outweigh the costs of liquefaction (e.g., a car park). In Eqs. 2.6-2.7, R_{FN} and R_{FP} are defined by:

$$R_{FN} = Q_{FN} / (Q_{FN} + Q_{TP}) \quad (2.8)$$

$$R_{FP} = Q_{FP} / (Q_{FP} + Q_{TN}) \quad (2.9)$$

where Q_{TP}, Q_{FP}, Q_{TN}, and Q_{FN} are respectively the quantities of true positives, false positives, true negatives, and false negatives. The denominators of Eqs. 2.8 and 2.9 equal the total number of sites with and without observed liquefaction manifestations, respectively. It follows from Eqs. 2.6-2.7 that two points in ROC space, (R_{FP1}, R_{TP1}) and (R_{FP2}, R_{TP2}), have equivalent performance if:

$$\frac{R_{TP1} - R_{TP2}}{R_{FP1} - R_{FP2}} = \frac{C_{FP}}{C_{FN}} = CR = m \quad (2.10)$$

Eq. (2.10) defines the slope, *m*, of an iso-performance line, such that all points defining the contour have equal *Cost'* (Provost and Fawcett, 2001). Thus, each *CR* corresponds to a unique contour in ROC space. One such line is shown in Figure 2.1b. With 1:1 slope, it corresponds to the case where false positives and false negatives have equal costs. Points tangent to this line on the ROC curve correspond to threshold values at which *Cost'* is minimized.

To evaluate model efficacy, two different ROC-based methods will be used. The first will quantify comprehensive performance via the area under a ROC curve (*AUC*). While no single parameter fully characterizes performance, *AUC* is commonly used for this purpose due to its statistical significance (e.g., Fawcett, 2006). Here, *AUC* is the probability that sites with manifestations have higher computed index values than sites without manifestations. Better prediction models thus have higher *AUC*. As shown in Figure 2.1b, random guessing is depicted in ROC space by a 1:1 line through the origin, for which *AUC* = 0.5. A perfect model, for which *AUC* = 1.0, plots as a point at (0,1), indicating the existence of a threshold value that perfectly separates the two distributions (e.g., all cases with manifestation have *LPI* above the threshold; all cases without manifestation have *LPI* below the threshold). To account for finite-sampling of case histories, bootstrap simulations will be performed to quantity ROC uncertainty, and in turn, to

compute confidence intervals on each model's *AUC*. This will illustrate the sensitivity of model performance to the particular case-histories compiled for analysis. To assess whether differences in *AUC* could arise from chance (i.e., due to finite sampling), tests of statistical significance will be performed per the method of DeLong et al. (1988), which is specific to ROC analyses. All models will be compared to one another to determine which, if any, are statistically better.

While *AUC* is widely used, it reflects overall performance across all misprediction economies. As a result, the model with highest *AUC,* the model with lowest misprediction rate ($R_{FN} + R_{FP}$), and the model most optimal when $C_{FN} \neq C_{FP}$ could conceivably all be different. This is shown in Figure 2.2a, where models A and B have identical *AUC*. If $CR = 1/5$, iso-performance lines have slope $m = 1/5$ and define points with equal prediction cost. What that cost *is* depends on the lines' R_{TP}-intercepts and is given by Eq. 2.6 (the greater the R_{TP}-intercept, the lower the cost). Since an iso-performance line tangent to curve B has a greater R_{TP}-intercept than one tangent to curve A, model B is more optimal. That is, B is better in the "conservative" region, where models correctly classify most positives, but at the expense of high R_{FP}. Conversely, and by the same logic, A is optimal when $CR = 5$ and is better in the "liberal" region, where models correctly classify most negatives, but at the expense of low R_{TP}. Lastly, when $CR = 1$, A and B perform equally well. Similarly, a model with higher *AUC* could be less efficient in a specific region of ROC space than a model with lower *AUC*. This is shown in Figure 2.2b: model A has higher *AUC* and is optimal when $CR > 0.27$, but model B is optimal for all other *CR*. Thus, *AUC* reflects overall performance, but not the nuances described above.

Accordingly, a second ROC-based analysis will identify the optimal model as a function of *CR*. *Cost'* will be computed by Eq. 2.7 for each model over the domain $0 < CR < 2$; that with lowest *Cost'* at a given *CR* is most optimal. This is equivalent to the graphical analysis shown in

Figure 2.2a and discussed above. Together, these methods will assess model performance, both in a comprehensive sense, and for various misprediction economies of interest.

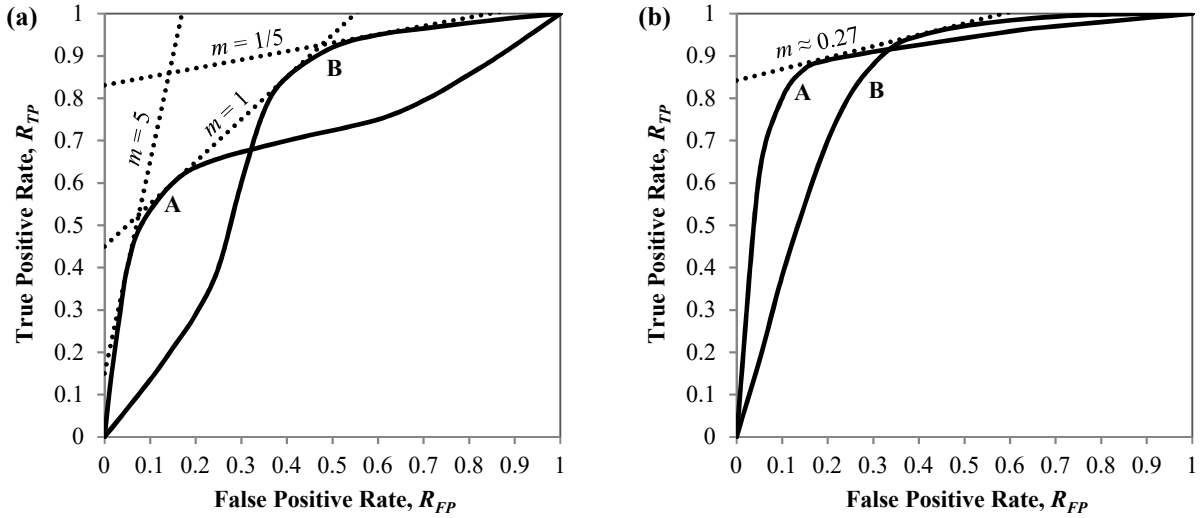

Figure 2.2. ROC analyses demonstrating that: (a) classifiers with equivalent *AUC* can perform very differently in specific regions of ROC space; (b) classifiers with higher *AUC* can, in specific regions of ROC space, perform worse than classifiers with lower *AUC*.

2.11 Results and Discussion

Utilizing the data and methodology above, 23 models were used to predict liquefaction manifestations for 15,222 well-documented case histories. To illustrate how ROC analyses and bootstrap simulations will be used to study model-performance, results for one model are first presented in detail; summary statistics from replicate analyses of the remaining 22 models will then be provided. In Figures 2.3a and 2.3b, ROC analyses of the BI14 – *LPI* geotechnical model (i.e., the BI14 triggering model used with the *LPI* manifestation model) are presented for the Canterbury and global datasets, respectively. In each case, a total of 10,000 bootstrap simulations were performed, from which 95%-confidence intervals (CIs) were computed. The 50th percentile ROC curve is equivalent to that resulting from an analysis of all case-histories without resampling. Two observations are made from this figure: (1) on average, the BI14-*LPI* model performs better

on the Canterbury dataset than the global dataset, with respective median AUCs of 0.83 versus 0.77; and (2) finite-sample uncertainty is considerably greater for the global dataset. The 95% CI on AUC is 0.828 to 0.841 for the Canterbury dataset, and 0.709 to 0.826 for the global dataset. Each of these observations will be discussed further in the context all models.

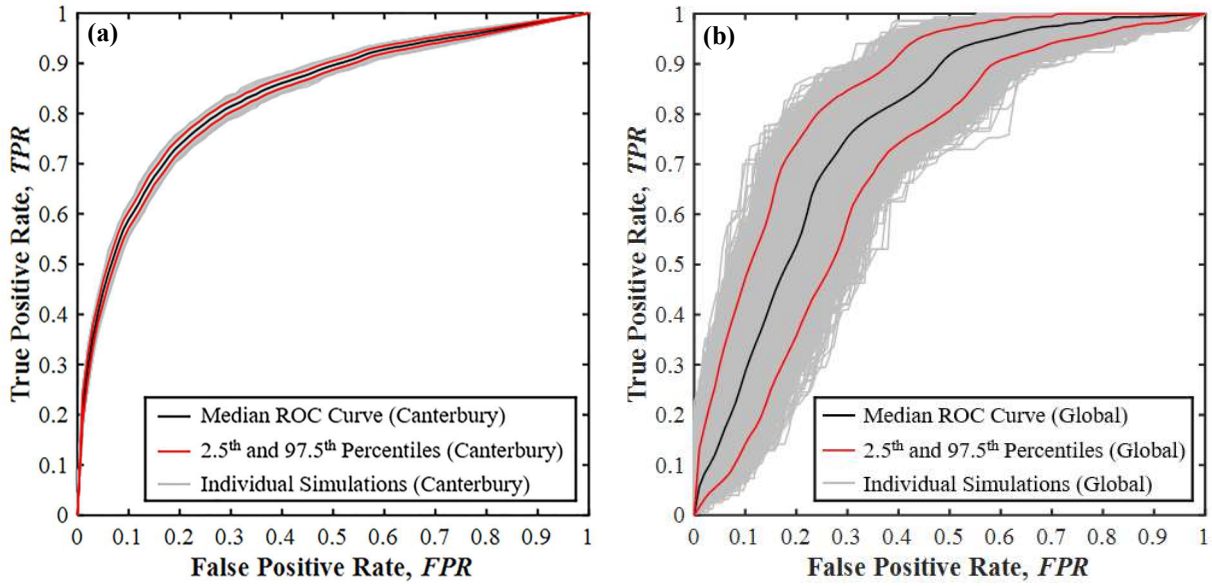

Figure 2.3 ROC analysis of BI14-*LPI* model performance in predicting liquefaction surface manifestation for the: (a) Canterbury dataset; and (b) global dataset.

From replicate ROC analyses of all 23 prediction models, *AUC* summary statistics are compiled and presented in Figures 2.4a and 2.4b for the Canterbury and global datasets, respectively. Shown are each model's median *AUC* and 95% CI, with results ordered by the year in which each model was proposed. In this regard, geotechnical models are dated in accordance with the triggering model but are grouped/symbolized by manifestation model. Thus, Figure 2.4 allows for assessments to be made regarding the evolution of performance (i.e., prediction efficiency) through twenty years of model research and development.

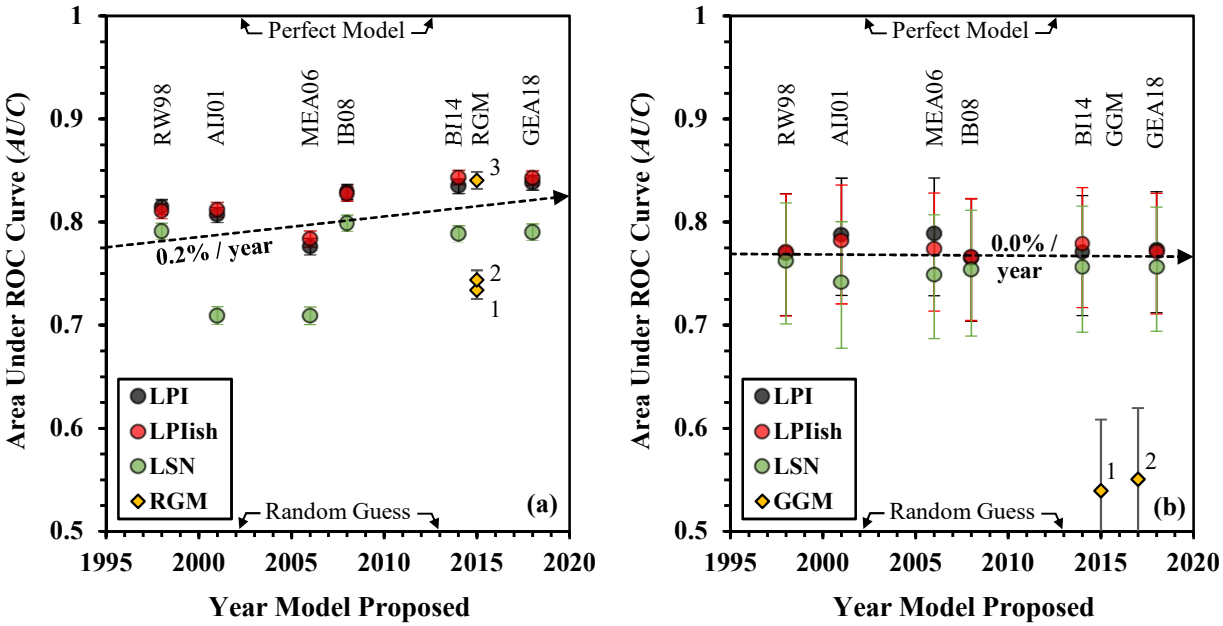

Figure 2.4 Summary of liquefaction-model performance – quantified by *AUC* – for 23 models, ordered by year proposed: (a) Canterbury dataset; and (b) global dataset. Markers denote median *AUC*; bars are 95% confidence intervals; all model acronyms are identified in Table 1. Trendlines developed from linear regression and do not include RGM or GGM data points.

With respect to Figure 2.4, several observations are made as follows. *First*, the two trends identified in Figure 2.3 for the BI14-*LPI* model are true of most geotechnical models. That is, their performance on their Canterbury dataset tends to be somewhat better and is significantly less variable, relative to the global dataset. Considering all 18 geotechnical models, the average *AUC*s are respectively 0.80 and 0.77 for the Canterbury and global datasets, indicating the models are somewhat nearer to perfection (*AUC* = 1.0) than to random guessing (*AUC* = 0.5). The average 95% CIs are respectively 0.015 and 0.118 for the Canterbury and global datasets. These differences may be attributable to the global dataset's greater seismologic, geologic, and geomorphic diversity and/or because the global field-data (e.g., ground-motion IMs, CPTs) were collected over a 50-year period using different means and methods. There are also significantly fewer global case-histories. All else being equal, greater finite-sample uncertainty is thus expected in analyses of the

global data. *Second*, as shown in Figure 2.4, trendlines were fit to the *AUC* values for all geotechnical models; these regressions did not include the regional or global geospatial models, which will be discussed momentarily. Through 20-years of model development, the trendlines suggest improvements to *AUC* of 0.2% and 0.0% per year for the Canterbury and global datasets, respectively. It should be noted that: (i) the BI14 and Gea18 triggering models, when developed, were trained on case-history datasets in which 20% of data was from the Canterbury earthquakes, so their evaluation in Figure 2.4a is not completely unbiased, unlike the other models; and (ii) geotechnical models, in general, were developed with training on case-history data, some of which also composes the global dataset compiled herein to test performance. Specifically, the overlap between data originally used to train the models, and data used to test the models herein, ranges from 0% (RW98) to 75% (e.g., BI14), with most models having >50% overlap. Accordingly, whether a trend of improvement should be expected in Figure 2.4b is debatable. Nonetheless, successive models proposed over the last twenty years show little or no demonstrable improvement for the two datasets analyzed, as shown in Figure 2.4. This is despite: (i) ever-increasing data that can be used to test, train, and validate models; and (ii) greater knowledge of liquefaction mechanics, embodied by new and revised model components (e.g., magnitude scaling; depth-stress reduction; overburden correction). It is surmised that greater performance-variation could result if the models were tested on data outside the parameter space of that used to train them (e.g., liquefaction-susceptible soils having atypical density, depth, fines-content, age, etc.). Of course, liquefaction case-histories tend to have much in common, so such data is not easily attained.

Third, it can be seen in Figure 2.4a that the three regional geospatial models perform remarkably well for the Canterbury dataset, with average *AUC* of 0.77 (versus 0.83 for all geotechnical models). One geospatial model – RGM3 – outperforms 16 of the 18 geotechnical

models. This result is provocative considering the relative complexity of the geotechnical models and the costs of their requisite inputs. While differences in model specificity must be acknowledged (RGM3 is region-specific, while the geotechnical models are not), it is nonetheless perplexing that a model which uses freely-available surface parameters could outperform established geotechnical models that use subsurface measurements. However, as shown in Figure 2.4b, geospatial models do not perform as well on the global dataset, with global models GGM1 and GGM2 having *AUC*s of 0.54 and 0.55, respectively (the models have 95% CIs of 0.47 to 0.61 and 0.48 to 0.62, respectively). Thus, while the geospatial models *do* tend to be useful (e.g., performing better than random guessing for the compiled test cases), the geotechnical models are significantly more efficient. This is unsurprising when considering: (i) the diversity of geomorphology, topography, climate, etc. present in the global dataset; and (ii) the difficulty, given this diversity, of accurately inferring below-ground conditions from above-ground parameters. Inherently, the geotechnical models - being based on direct measurements of the subsurface - should have greater portability across environs. Nonetheless, the results from Canterbury in Figure 2.4a demonstrate the provocative potential of geospatial modeling. As more test data becomes available, and as better geospatial predictors are identified, improved global performance should result. In contrast, considering the 20-year trendlines in Figure 2.4, it appears that geotechnical models should not be expected to soon improve greatly, if the status quo continues. Neither fine-tuning of model parameters, nor incremental growth in training data, are likely to inflect these trends upwards. Arguably, this would occur only through wholesale innovation (e.g., disruptive changes to the in-situ characterization method, or to the fundamental modeling approach). *Fourth*, the top-performing models, as quantified via *AUC*, are: (i) Canterbury dataset: BI14-LPI_{ISH} (AUC = 0.843), Gea18-LPI_{ISH} (AUC = 0.843), and RGM3 (AUC = 0.841); and (ii) global dataset: Mea06-

LPI (*AUC* = 0.788), AIJ01-*LPI* (*AUC* = 0.788), and AIJ01- LPI_{ISH} (*AUC* = 0.782). Thus, the top-performing models are different for the two datasets. However, given the uncertainties of *AUC* values – particularly for the global dataset - it should be determined whether the measured differences in performance are statistically significant.

Using the method of DeLong et al. (1988), P-values were computed to compare each of the 23 models to all others. These values are presented in Tables 2.4 and 2.5 for the Canterbury and global datasets, respectively, and are the probabilities that *AUC* samples for two models could have come from the same distribution (i.e., that the observed difference in performance arose from chance, and not because one model is better than another). Large P-values can be expected when (i) differences between two *AUC* values are small; and (ii) the uncertainty of one or more of the *AUC* values is large. The popular significance level of 0.05 of adopted herein, such that P-values below this level indicate that models have significantly different performance. Using this criterion, Tables 2.4 and 2.5 compare all model pairs and identify which model, if any, is statistically better.

Table 2.4 P-Value Matrix to Compare Model Performance for the Canterbury Dataset

Statistically Better	↑	LPI						LPI_{ISH}						LSN						RGM		
←		*RW98*	*AIJ01*	*Mea06*	*IB08*	*BI14*	*Gea18*	*RW98*	*AIJ01*	*Mea06*	*IB08*	*BI14*	*Gea18*	*RW98*	*AIJ01*	*Mea06*	*IB08*	*BI14*	*Gea18*	*1*	*2*	*3*
LPI	*RW98*		0.000	0.000	0.000	0.000	0.000	0.000	0.018	0.000	0.000	0.000	0.000	0.000	0.000	0.000	0.000	0.000	0.000	0.000	0.000	0.000
	AIJ01			0.000	0.000	0.000	0.000	0.177	0.001	0.000	0.000	0.000	0.000	0.000	0.000	0.000	0.000	0.000	0.000	0.000	0.000	0.000
	Mea06				0.000	0.000	0.000	0.000	0.000	0.000	0.000	0.000	0.000	0.000	0.000	0.000	0.000	0.000	0.000	0.000	0.000	0.000
	IB08					0.000	0.000	0.000	0.000	0.000	0.013	0.000	0.000	0.000	0.000	0.000	0.000	0.000	0.000	0.000	0.000	0.002
	BI14						0.000	0.000	0.000	0.000	0.000	0.000	0.000	0.000	0.000	0.000	0.000	0.000	0.000	0.000	0.000	0.082
	Gea18							0.000	0.000	0.000	0.000	0.004	0.023	0.000	0.000	0.000	0.000	0.000	0.000	0.000	0.000	0.362
LPI_{ISH}	*RW98*								0.530	0.000	0.000	0.000	0.000	0.000	0.000	0.000	0.000	0.000	0.000	0.000	0.000	0.000
	AIJ01									0.000	0.000	0.000	0.000	0.000	0.000	0.000	0.000	0.000	0.000	0.000	0.000	0.000
	Mea06										0.000	0.000	0.000	0.000	0.000	0.000	0.000	0.023	0.002	0.000	0.000	0.000
	IB08											0.000	0.000	0.000	0.000	0.000	0.000	0.000	0.000	0.000	0.000	0.000
	BI14												0.271	0.000	0.000	0.000	0.000	0.000	0.000	0.000	0.000	0.943
	Gea18													0.000	0.000	0.000	0.000	0.000	0.000	0.000	0.000	0.823
LSN	*RW98*														0.000	0.000	0.000	0.043	0.399	0.000	0.000	0.000
	AIJ01															0.760	0.000	0.000	0.000	0.000	0.000	0.000
	Mea06																0.000	0.000	0.000	0.000	0.000	0.000
	IB08																	0.000	0.000	0.000	0.000	0.000
	BI14																		0.000	0.000	0.000	0.000
	Gea18																			0.000	0.000	0.000
RGM	*1*																				0.026	0.000
	2																					0.000
	3																					

As seen in Table 2.4, instances of large P-values are rare for the Canterbury dataset, which can be partly attributed to the large quantity of case histories. Moreover, nearly every model performs significantly different than all others. Notable observations from Table 2.4 are: (i) among all geotechnical and geospatial models evaluated, no model is statistically better than all others; but (ii) three models are either statistically better, or not statistically different, than all others. In other words, three models are not bested by any others. These are BI14-LPI_{ISH}, Gea18-LPI_{ISH}, and RGM3. Most striking is the fact that no geotechnical model is statistically better than geospatial model RGM3.

Table 2.5 P-Value Matrix to Compare Model Performance for the Global Dataset

Statistically Better	↑	LPI						LPI_{ISH}						LSN						GGM	
←		*RW98*	*ALJ01*	*Mea06*	*IB08*	*BI14*	*Gea18*	*RW98*	*ALJ01*	*Mea06*	*IB08*	*BI14*	*Gea18*	*RW98*	*ALJ01*	*Mea06*	*IB08*	*BI14*	*Gea18*	*1*	*2*
LPI	*RW98*		0.166	0.046	0.446	0.933	0.682	0.898	0.467	0.759	0.696	0.435	0.894	0.571	0.224	0.263	0.244	0.377	0.369	0.000	0.000
	ALJ01			0.978	0.105	0.211	0.255	0.245	0.439	0.368	0.137	0.500	0.248	0.092	0.004	0.031	0.032	0.051	0.052	0.000	0.000
	Mea06				0.040	0.135	0.162	0.120	0.657	0.135	0.066	0.441	0.186	0.026	0.020	0.004	0.009	0.021	0.021	0.000	0.000
	IB08					0.355	0.101	0.582	0.338	0.565	0.887	0.144	0.521	0.857	0.346	0.420	0.400	0.569	0.555	0.000	0.000
	BI14						0.358	0.975	0.525	0.824	0.678	0.379	0.944	0.596	0.259	0.290	0.231	0.328	0.329	0.000	0.000
	Gea18							0.870	0.598	0.931	0.466	0.511	0.855	0.461	0.205	0.220	0.140	0.224	0.224	0.000	0.000
LPI_{ISH}	*RW98*								0.458	0.759	0.490	0.472	0.973	0.544	0.181	0.240	0.245	0.380	0.367	0.000	0.000
	ALJ01									0.582	0.301	0.815	0.475	0.247	0.005	0.074	0.113	0.163	0.157	0.000	0.000
	Mea06										0.527	0.787	0.819	0.361	0.077	0.070	0.165	0.250	0.240	0.000	0.000
	IB08											0.053	0.353	0.790	0.285	0.368	0.354	0.521	0.504	0.000	0.000
	BI14												0.076	0.319	0.134	0.154	0.097	0.158	0.154	0.000	0.000
	Gea18													0.557	0.206	0.256	0.215	0.325	0.313	0.000	0.000
LSN	*RW98*														0.258	0.154	0.142	0.362	0.321	0.000	0.000
	ALJ01															0.657	0.551	0.461	0.470	0.000	0.000
	Mea06																0.678	0.493	0.510	0.000	0.000
	IB08																	0.451	0.498	0.000	0.000
	BI14																		0.792	0.000	0.000
	Gea18																			0.000	0.000
GGM	*1*																				0.779
	2																				

In contrast to the Canterbury dataset, few P-values are below 0.05 for the global dataset, indicating that performance-differences between models are typically not statistically significant. Notable observations from Table 2.5 are: (i) all geotechnical models are statistically better than both global geospatial models; and (ii) no model is statistically superior. The previously identified top-performing model globally – Mea06-*LPI* – is statistically better than nine other models, but is statistically indifferent from eight others, including the top-performing models in Canterbury (BI14-LPI_{ISH} and Gea18-LPI_{ISH}). Thus, once statistical significance is considered, the global results are largely inconclusive due to the large finite-sample uncertainties of *AUC* values. Consequently, the top-performing geotechnical models in Canterbury may also be the top-

performing models globally, but more global case-history data would be needed to confirm this, or to draw further conclusions about model performance.

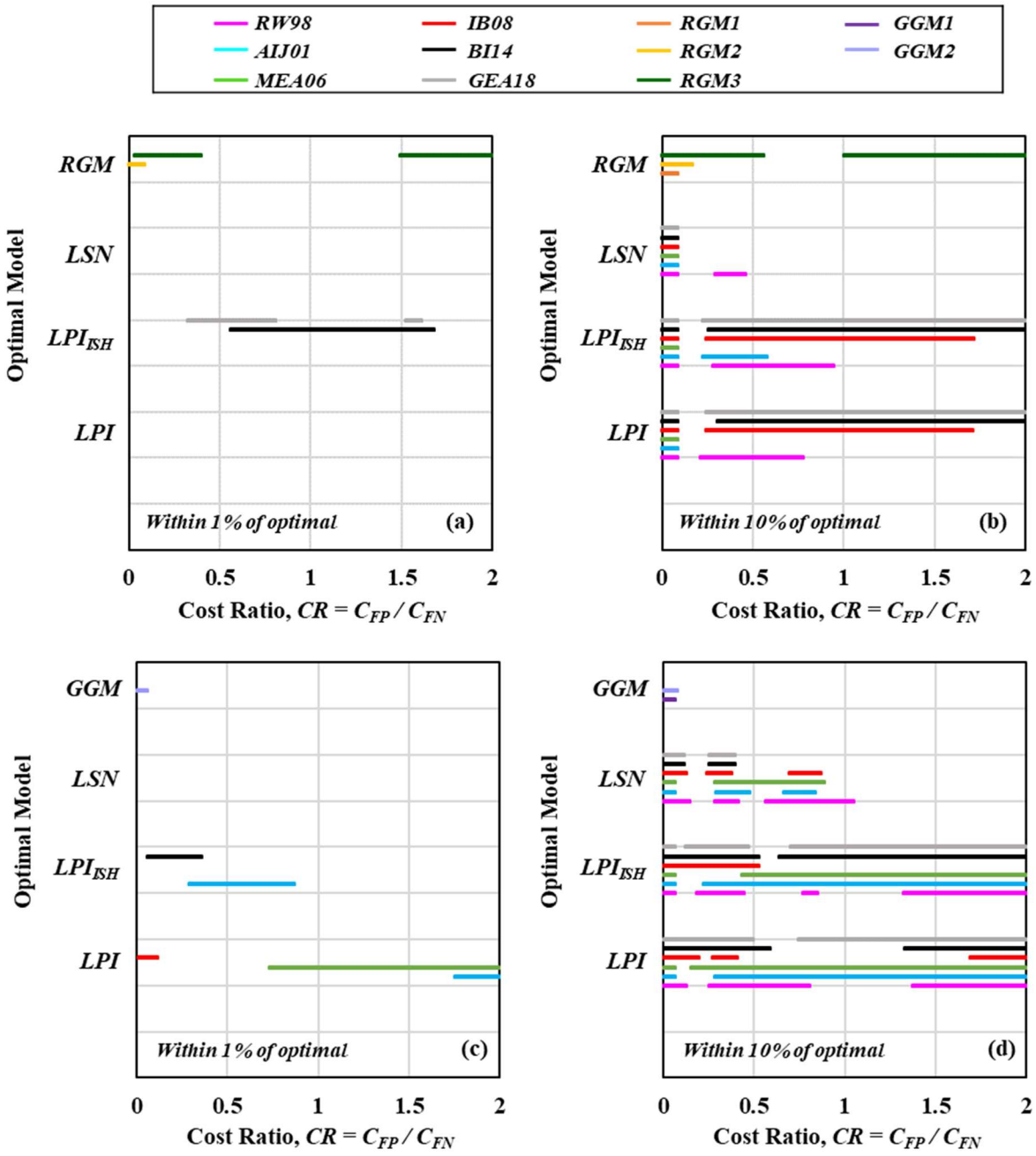

Figure 2.5 Optimal liquefaction model as a function of *CR*, as determined from ROC analyses of the Canterbury dataset, wherein "optimal" models are those within (a) 1% of optimal and (b) 10% of optimal; analogous analyses are presented in panels (c) and (d) for the global dataset.

As discussed, AUC is widely used to study diagnostic model behavior, but it reflects overall performance across all misprediction economies. To identify the most efficient model for particular economies, Cost' is computed for each model at different CR values. The model with lowest Cost' is identified in Figure 2.5 for CRs ranging from 0 to 2. Also, because multiple models could have nearly equivalent efficiency, and thus, be equally optimal, any model whose Cost' is within 1% of minimum is likewise identified as "optimal." To assess the sensitivity of results to this criterion, analyses are repeated by relaxing the threshold to 10%. Results for the Canterbury and global datasets are shown in Figures 2.5a,b and 2.5c,d, respectively. Several observations are made from Figure 2.5 as follows. It can be seen that while the models with highest AUC tend to appear in Figure 2.5 (i.e., they are optimal for some range of misprediction economies), the results convey more nuanced information than AUC alone. For example, as seen in Figure 2.5a, geospatial models RGM2 and RGM3 are the best-performing models in the conservative, or "northeast", region of ROC space, considering the Canterbury dataset. Thus, for scenarios in which CFN far exceeds CFP, the geospatial models perform best, meaning they are very efficient at predicting liquefaction, but at the expense of a high rate of false-positives. Conversely, it can be seen in Figure 2.5a that models BI14-LPI_{ISH} and Gea18-LPI_{ISH} are optimal in the range of $0.25 < CR < 1.75$, or scenarios in which CFN and CFP are relatively more similar. It can also be seen that models with relatively low AUC are sometimes optimal in specific regions of ROC space. Most striking, for example, is that geospatial model GGM2 is the most optimal model for the global dataset at low CR values. This is despite the fact that its AUC, or overall prediction efficiency, was significantly lower than all geotechnical models. Extending the threshold for identifying optimal models to 10%, it can be seen that each of the 23 models evaluated is "optimal" for some region of ROC space. Thus, Figure 2.5 provides greater insight as to when a model is likely to perform well.

2.12 CONCLUSIONS

Semi-empirical models based on in-situ geotechnical tests have been the standard-of-practice for predicting soil liquefaction since 1971. More recently, prediction models based on free, readily-available data were proposed. These "geospatial" models rely on satellite remote-sensing to infer subsurface traits without in-situ tests. Using 15,222 liquefaction case-histories from 24 earthquakes, this study evaluated the performance of 23 models based on geotechnical or geospatial data using standardized and objective metrics of performance. Uncertainty due to finite sampling of case histories was accounted for and used to establish statistical significance. Geotechnical predictions were found to be significantly more efficient on a global scale, yet successive models proposed over the last twenty years show little demonstrable improvement. Moreover, geospatial models performed equally well for the Canterbury dataset, either outperforming or matching the performance of every geotechnical model. This is a surprising finding given the relative time- and cost-requirements underlying these predictions. While further research is needed to improve the portability of geospatial models across diverse environs, this assessment demonstrated their provocative potential.

2.13 GLOBAL DATASET REFERENCES

The sources of data used in the compilation of the global dataset are listed as follows, parsed by event: **1964 Mw7.6 Niigata, JPN** - Ishihara and Koga (1981), Farrar (1990), Moss et al. (2003); 1971 Mw6.6 San Fernando, USA - Bennett et al., (1998), Toprak and Holzer (2003); **1975 Mw7.0 Haicheng, CHN** - Arulandan et al. (1986), Shengcong and Tatsuoka (1984); **1976 Mw7.6 Tangshan, CHN** - Shibata and Teparaska (1988), Moss et al. (2009; 2011); **1979 Mw6.53 Imperial Valley, USA** - Diaz-Rodriguez (1984), Diaz-Rodriguez and Armijo-Palacio (1991),

Moss et al. (2003); **1981 Mw5.9 Westmoreland, USA** - Bennett et al. (1984), Seed et al. (1984), Cetin et al. (2000), Moss et al. (2005); **1983 Mw7.7 Nihonkai-Chubu, JPN** - Farrar (1990); **1983 Mw6.88 Borah Peak, USA** - Andrus (1986), Andrus & Youd (1987), Moss et al. (2003); **1987 Mw6.6 Edgecumbe, NZ** - Christensen (1995), Moss et al. (2003); **1987 Mw6.54 Superstition Hills, USA** - Bennett et al. (1984), Cetin et al. (2000), Toprak and Holzer (2003), Moss et al. (2005), Holzer and Youd (2007); **1989 Mw6.93 Loma Prieta, USA** - Mitchell et al. (1994), Pass (1994), Bennett & Tinsely (1995), Boulanger et al. (1995; 1997), Kayen et al. (1998), Toprak & Holzer (2003), Youd and Carter (2005); **1994 Mw6.69 Northridge, USA** - Abdel-Haq & Hryciw (1998), Bennett et al., (1998), Holzer et al. (1999), Moss et al. (2003); **1995 Mw6.9 Hyogoken-Nambu, JPN** - Suzuki et al. (2003); **1999 Mw7.51 Kocaeli, TUR** - PEER (2000a), Youd et al. (2009); **1999 Mw7.62 Chi-Chi, TWN** - Lee et al. (2000), PEER (2000b); **2008 Mw6.4 Achaia-Ilia, GRC** - Batilas et al. (2014); **2008 Mw7.2 El Mayor-Cucapah, MEX** - Moss et al. (2005); CESMD (2016), Turner et al. (2016); **2011 Mw9 Tohoku, JPN** - Cox et al. (2013), Boulanger and Idriss (2014); **2012 Mw6.1 Emilia, ITA** - Papathanassiou et al. (2015), Facciorusso et al. (2015), Servizio Geologico (2016).

Chapter 3. ON THE EXTENSION OF GEOSPATIAL LIQUEFACTION MODLES TO PREDICT GROUND FAILURE, INFRASTRUCUTRE DAMAGE, AND ECONOMIC LOSS

3.1 INTRODUCTION

In Chapter 2, the efficacies of 23 liquefaction-prediction models were investigated using 15,222 case-histories compiled from 24 earthquakes. These case-histories were parsed into two datasets: the Canterbury dataset, containing case-histories from three events in Canterbury, New Zealand, and the global dataset, containing case-histories from 21 globally-distributed events. While semi-empirical models based on the cone penetration test (CPT) performed significantly better on the global dataset, geospatial models performed as well or better in Canterbury than all 18 geotechnical models evaluated. Thus, while the global portability of the geospatial models must be improved, their performance in Canterbury showcases a provocative potential. Given the demonstrated efficiency of geospatial models to predict liquefaction in Canterbury, Chapter 3 explores their extension to also predict the magnitude of ground settlement, the occurrence and severity of damage to shallow-foundation systems, and the ensuing economic loss for such systems. If successful, geospatial models would provide a means to predict liquefaction-induced damage and loss in near real-time (e.g., within seconds of an earthquake occurring). This analysis is facilitated by unprecedented infrastructure-performance and loss data resulting from the Canterbury earthquakes. In particular, this study will utilize 62,009 foundation-damage surveys and 53,940 insurance loss assessments. The geospatial models perform fairly well in predicting some large-scale failure mechanisms (e.g., global settlement), however they are not good predictors for other small-scale failure mechanisms (e.g., dishing, hogging). Additionally, the

geospatial models are poor relations for less estimates, especially when trying to predict higher asset losses.

3.2 BACKGROUND

Soil liquefaction is a common cause of ground failure during earthquakes and is responsible for tremendous damage to infrastructure. Its effects were vividly observed during the 2010-2016 Canterbury, New Zealand, Earthquake Sequence (CES) which induced pervasive liquefaction in the city of Christchurch and its environs causing ~$10B in infrastructure damage (Parker and Steenkamp, 2012). As the CES illustrates, accurate prediction of infrastructure damage and loss due to liquefaction is critical for regional hazard-mapping, city planning, engineering design, regulatory policy, and emergency response. The state-of-practice approaches for predicting the occurrence and severity of soil liquefaction at a regional-scale rely on (a) surficial geology maps that are typically too general to be accurate at site-specific scales; and/or (b) in-situ geotechnical tests that are typically too costly and time-consuming to be feasible over large areal extents. More recently, liquefaction-prediction models were proposed based on free, remotely-sensed geospatial information (Zhu et al., 2015, 2017). In contrast to geotechnical methods, "geospatial" liquefaction models can evaluate liquefaction potential rapidly, at infinitely many locations, anywhere in the world. This is made possible using geospatial proxies of soil properties relevant to liquefaction (e.g., proxies of soil density, soil type, saturation, and thickness of liquefiable deposit) and seismic parameters that are easily obtained or estimated (e.g., peak ground acceleration). Examples of such proxies include, among others: topographic slope; surface mineralogy; distance to water bodies; and compound-topographic-index, which can all be derived from satellite remote sensing.

Chapter 2 compared the efficacy of numerous models based on geotechnical and geospatial data. Specifically, six CPT-based liquefaction-triggering models (Robertson and Wride, 1998;

Architectural Institute of Japan, 2001; Moss et al., 2006; Idriss and Boulanger, 2008; Boulanger and Idriss, 2014; Green et al., 2018) were each used in series with three liquefaction manifestation models (Iwasaki et al., 1978; van Ballegooy et al., 2014; and Maurer et al., 2015) for a total of 18 distinct geotechnical models. These were compared to five geospatial models proposed by Zhu et al. (2015, 2017), three of which were proposed specifically for Canterbury, New Zealand, and two of which were proposed for global application. Based on an analysis of approximately 15,000 case histories from the CES, geospatial models performed as well or better than the geotechnical models. In particular, the best-performing geospatial model was "Regional Geospatial Model 3" (Zhu et al., 2015). In this regard, all models were evaluated on their ability to predict whether sites had manifestations of liquefaction at the surface (specifically liquefaction ejecta). However, the physical damage and monetary loss resulting from liquefaction, rather than its occurrence, are of greatest concern to planners, insurers, and owners of infrastructure assets. Hazard-management decisions are made based on damage and loss, not on factors of safety or probabilities of liquefaction. In this regard, the severity of ground deformation, rather than the binomial observation of liquefaction, would provide a more useful assessment of damage-potential for civil infrastructure. This study will also utilize post-earthquake foundation-damage surveys performed during the CES. These will be used to develop fragility functions that predict the severity of liquefaction-induced foundation damage using geospatial liquefaction models. Lastly, insurance-loss assessments will be used to formulate vulnerability functions that predict economic losses using geospatial liquefaction models. Collectively, these extensions of geospatial modelling would allow for the rapid (i.e., near real-time) prediction of ground failure, infrastructure damage, and economic loss following an earthquake.

3.3 DATA

This study analyzes post-earthquake foundation-damage surveys of 62,009 lightweight structures founded on several types of shallow-foundation system and overlying potentially liquefaction soils. These surveys were performed throughout the 2010-2016 Canterbury earthquake sequence by a team of more than 200 engineers. The surveys were performed under the auspices of the New Zealand Earthquake Commission (EQC) and were compiled by Taylor & Tonkin, Ltd. As part of these efforts, insurance loss assessments were performed for approximately 53,940 structures built atop shallow foundations. The details of these datasets and some derived relations are discussed next.

3.4 CANTERBURY EARTHQUAKE (CES) DATASET

Earthquakes occurring over the last decade in the Canterbury region of New Zealand have resulted in case-history data of unprecedented quantity and quality, presenting a unique opportunity to advance the science of liquefaction modelling. A comprehensive summary of these earthquakes, to include tectonic and geologic settings, seismology, and effects, is provided by Quigley et al. (2016). Of interest in this study, the case-histories from the M_w7.1, 4 Sept. 2010 Darfield earthquake, the M_w6.2, 22 Feb. 2011 Christchurch earthquake, the M_w5.7, the M_w5.9, 13 Jun. 2011 Christchurch earthquake, and the M_w5.9, 23 Dec. 2011 Christchurch earthquake were compiled. Previous studies referenced herein also utilized case histories from the 14 Feb. 2016 Christchurch (or “Valentine’s Day”) earthquake. The data for each earthquake includes parameters utilized in liquefaction model calculations such as ground-motion intensity measures, geotechnical and hydrological data, and readily available geospatial information.

3.5 GEOSPATIAL MODELS AND DATA

There are a variety of geospatial models which correlate different explanatory variables and the probability of liquefaction. Model performances for the Christchurch, New Zealand region was analyzed in Chapter 2 using receiver operating characteristic (ROC) analyses and results are presented in Table 2.4. As shown in Figure 3.1 the best performing geospatial models include (1) a model developed for use worldwide and is referred to herein as "Global Geospatial Model" or abbreviated as "2017 GGM2" and (2) a model developed specifically for use in Canterbury, New Zealand, and is referred to herein as the "Region-Specific Geospatial Model" or abbreviated as "2015 RGM3".

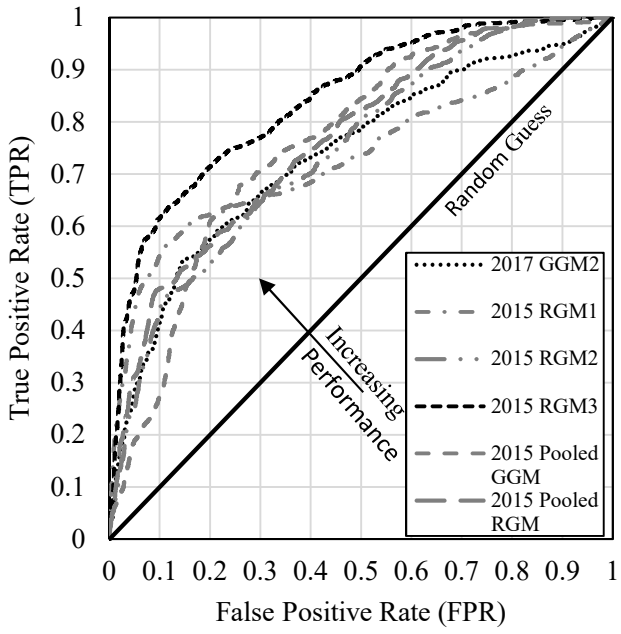

Figure 3.1 ROC analyses comparison of Geospatial Liquefaction Models

These two geospatial models were developed by Zhu et al. (2015; 2017) and have the general form:

$$P(X) = (1 + e^{-X})^{-1} \tag{3.11}$$

where X is a series of geospatial variables and model coefficients, and $P(X)$ is the probability of liquefaction manifestation and is used as an index for comparison (GLI). In conjunction with Eq. (3.11), these models are respectively defined by:

Global Geospatial Model (Zhu et al., 2017), "2017 GGM2":

Location within 20 km from coast:

$$X = 12.435 + 0.301 \cdot \ln(PGV) - 2.615 \cdot \ln(V_{s30}) + 5.556 \times 10^{-4} \cdot precip - 0.0287 \cdot (d_c)^{0.5} + 0.0666 \cdot d_r - 0.0369 \cdot d_r \cdot (d_c)^{0.5} \quad (3.12)$$

Location further than 20 km from coast:

$$X = 8.801 + 0.334 \cdot \ln(PGV) - 1.918 \cdot \ln(V_{s30}) + 5.408 \times 10\text{-}4 \cdot precip - 0.2054 \cdot dw - 0.0333 \cdot wtd \quad (3.13)$$

Regional Geospatial Model (Zhu et al., 2014a), "2015 RGM3":

$$X = 25.45 + 2.476 \cdot \ln(PGA_M) - 0.323 \cdot d_{r3} - 4.241 \cdot \ln(V_{s30}) \quad (3.14)$$

where PGA_M is magnitude-weighted *PGA (g)* computed using a magnitude scaling factor*;* PGV is the peak ground velocity (cm/s) (USGS, 2018); V_{s30} is shear-wave velocity (cm/s) of the upper 30-m of the soil profile, estimated from topographic slope; *dc* is the distance to coast (km); *dr* is the distance to rivers (km); *precip* is the mean annual precipitation (mm); *dw* is the distance to nearest water body (calculated as minimum of *dr* and *dc*); *wtd* is the water table depth extracted from global dataset modeled by Fan *et al.* (2013);and d_{r3} is the distance to a stream of order three or greater, as defined by the Strahler stream-ordering method. These parameters were computed per the exact methodologies described in Zhu et al. (2015; 2017), to which the reader is referred for additional information.

3.6 GROUND FAILURE

The geospatial liquefaction models to be used herein were previously evaluated in Chapter 2 on their abilities to binomially predict liquefaction ejecta on free-field level ground. Observations of the occurrence and severity of liquefaction ejecta were compiled by the authors following the

Sept. 2010, Feb. 2011, and Feb. 2016 earthquakes and classified using the Green et al. (2014) criteria, which ranks the manifestations as “none,” “minor,” “moderate,” and “severe.” This was accomplished using ground reconnaissance and high-resolution aerial and satellite imagery captured immediately after each event (CGD, 2012). Cases in which manifestations could not be reliably classified were removed (e.g., where ground reconnaissance and aerial imagery disagreed, or where aerial imagery was inconclusive) and resulted in a total of 14,948 case histories.

3.7 LIQUEFACTION INDUCED SETTLEMENTS

The CES also resulted in many measurements of ground deformations due to liquefaction, made possible by airborne and satellite mounted LIDAR and InSAR systems, which only recently have become widely accessible. These systems have allowed ground deformations to be measured at unprecedented regional extents following liquefaction events. Using these systems, settlements were measured at each location used in section 3.6 to develop fragility curves for predicting manifestation severity. These measured settlements are plotted against the geospatial model-index values, for both GGM2 and RGM3, in Figures 3.2 and 3.3, respectively.

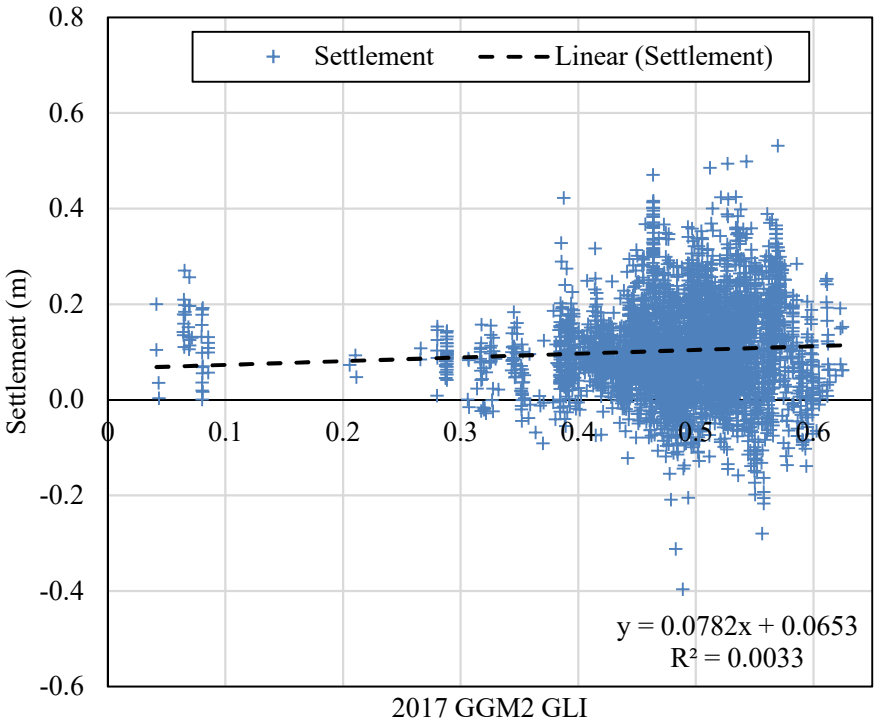

Figure 3.2 GGM2 model index vs. measured ground settlement

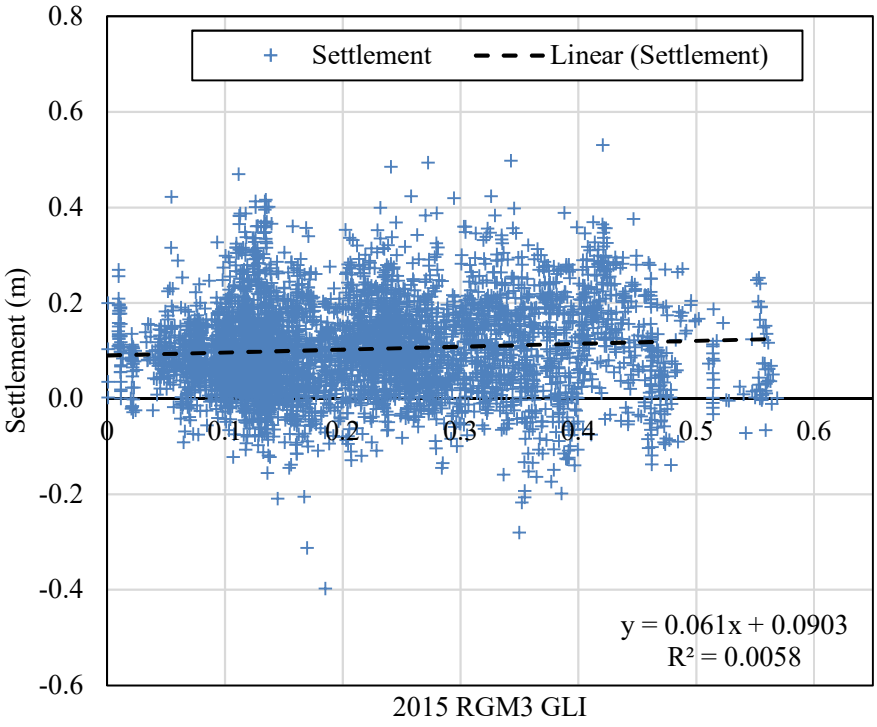

Figure 3.3 RGM3 model index vs. measured ground settlement

As seen in Figures 3.2 and 3.3, the abilities of the geospatial models to predict ground settlement is relatively poor. While there is a slightly positive correlation between geospatial model predictions and ground settlement, the correlations are very weak. This could be attributable to large measurement uncertainty in the observed settlement (σ = 7 cm). Thus, the geospatial models can predict the occurrence and severity of liquefaction ejecta in Canterbury but are much less capable of predicting the magnitude of ground settlement.

3.8 FOUNDATION DAMAGE INSPECTIONS

Inspections were performed at sites around Christchurch, New Zealand and the surrounding area following the CES events spanning from September 2010 to December 2011. Some properties were inspected only once and others were inspected multiple times, but in total 62,009 unique sites were inspected for building damage. The assets were categorized by foundation type, including (1) timber floors on piles, (2) timber on internal piles with perimeter concrete footings, (3) concrete slab on grade, and (4) mixed foundations. The foundations were visually inspected for different modes, or mechanisms, of damage. Each mode of damage was also classified by severity as minor, moderate, or major. The modes of damage, and criteria for classifying their severity, are shown in Figure 3.4 below. For locations where more than one mode of damage was observed, the severity of each mode of damage was also recorded.

Type of Damage	Severity		
	Minor	Moderate	Major
Stretching 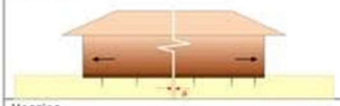	0 to 5mm	5 to 30mm	>30mm
Hogging 	0 to 20mm	20 to 50mm	>50mm
Dishing 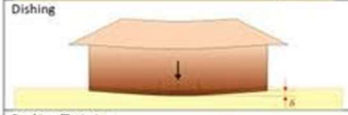	0 to 20mm	20 to 50mm	>50mm
Racking/Twisting 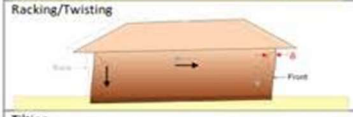	0 to 10mm	10 to 30mm	>30mm
Tilting 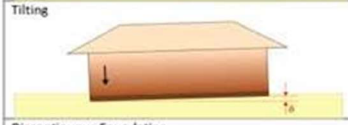	0 to 20mm	20 to 50mm	>50mm
Discontinuous Foundation 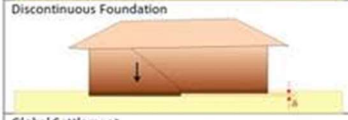	0 to 10mm	10 to 20mm	>20mm
Global Settlement 	0 to 50mm	50 to 100mm	>100mm

Figure 3.4 Foundation damage survey mechanism type and severity.

While many assets were inspected multiple times, most were not inspected in-between each of the individual earthquakes comprising the Canterbury sequence. In the cases where an inspection was performed multiple times at the same asset between events (i.e. an inspection was performed after the September 2010 event *and* after the February 2011 event), the damage inspections were compared to account for compounding damage estimates which might overpredict damage for the later event. Since the magnitude severities were general scales, future inspections with a higher severity than a previous survey were reduced by the previous survey severity (i.e., if damage was minor during a September 2010 inspection, and was moderate during a February 2011 inspection, it was assumed that the February 2011 earthquake was responsible for the difference). Additionally, some assets were only surveyed once, or were only surveyed after experiencing

multiple earthquake events, in which case the observe damage could have conceivably occurred in one of several earthquakes. For these cases, the damage severity was distributed out between the previous events by scaling by the liquefaction model probability for the event and relating to the surveyed severity:

$$Event\ Severity = Survey\ Severity * \frac{Event\ GLI}{\Sigma(Previous\ Event\ GLI's + Survey\ Event\ GLI)} \quad (3.15)$$

The result would, for example, distribute a "major" severity observed after three events into "minor" severities across each of the three events. This was done since it cannot accurately be related to which event caused the most damage, or if the series of events resulted in progressive damage.

3.9 Building Damage Surveys

Whereas insurance loss assessments are typically private and closely guarded, the unique role of the New Zealand government as a land insurer led to their assessment of losses for 53,940 infrastructure assets affected by liquefaction. This loss data is available for many parcel locations across Christchurch, New Zealand classified by different ranges of building damage ratios (BDR). The BDR is the ratio of repair cost for the damage divided by the replacement cost new (RCN) of the asset. This data was extracted from GIS parcel data provided by Taylor & Tonkin, Ltd. which was classified into BDR ranges:

Table 3.6 Geospatial Liquefaction Model Equations

BDR Range	Value Assigned for Vulnerability Function
0.0 - 0.10	0.05
0.11 - 0.20	0.15
0.21 - 0.30	0.25
0.31 - 0.40	0.35
0.41 - 0.50	0.35
0.51 - 0.75	0.625
>0.75	0.75
Unknown	*Removed

*Removed when developing the functions.

The mid-value of the BDR range was utilized to create vulnerability functions based on the GLI at the centroid of the parcels since the resolution of the geospatial parameters was generally considerably larger than the parcel size. Relating the loss to the GLI provides a straightforward relationship which can be used for rapid damage estimates.

3.10 METHODOLOGY

Additional model details and methodology are now presented, followed by the methods that will be adopted to study and compare model performance.

3.11 FRAGILITY MODEL METHODOLOGY

Fragility functions were developed using the approach outlined below, similar to that described by Porter et al. (2006) for predicting seismic-damage to structural elements. $F_{dm}(GLI)$ denotes the fragility function for damage state *dm*, defined as the probability that the foundation reaches or exceeds damage state *dm*, given a computed GLI, and idealized by a log-normal distribution (Eq. 3.16):

$$F_{dm}(GLI) = \Phi\left(\frac{ln(\frac{GLI}{x_m})}{\beta}\right) \quad (3.16)$$

where Φ denotes the Gaussian cumulative distribution function; x_m is the median of the distribution, and β is the logarithmic standard deviation (i.e., dispersion).

The manifestation severities for ground failure were thus analyzed to develop fragility functions using the two best-performing regional and global geospatial models (Figures 3.5a and 3.5b). These functions show the probability of exceeding three manifestation states (MS), where the MS classifications are the criteria used by Green et al. (2014). The dataset was also analyzed taking 10,000 bootstrap samplings to capture finite-sample uncertainty. It can be seen that both of the geospatial models evaluated are capable of predicting not only the binomial occurrence of liquefaction ejecta, but also its extent/intensity, which should better relate to liquefaction damage-potential.

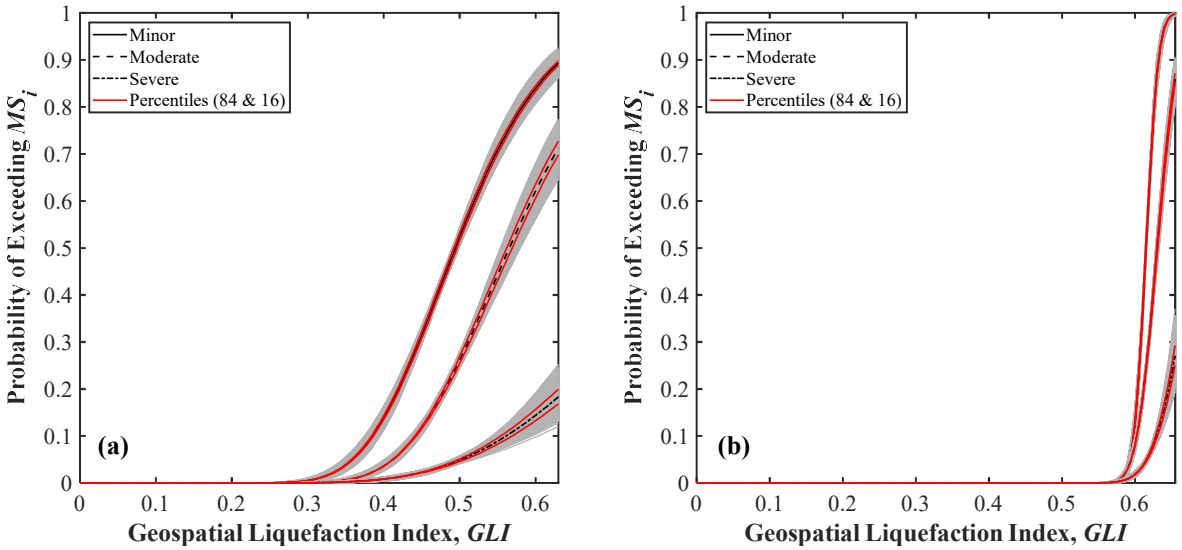

Figure 3.5 Fragility functions for predicting the severity of ground failure using the (a) GGM2 global geospatial model; and (b) RGM3 region-specific geospatial model.

Using the detailed survey inspection data, fragility functions of this form were also derived for the three severity states (minor, moderate, major) for each foundation type. Since RGM3 was the best performing in terms of *AUC* (see Chapter 2), its fragility functions for the compilation of all foundation types at different failure mechanism are shown in Figure 3.6 and are representative of the general trends across both models (further figures included in an Appendix). These functions generally had low probabilities of exceeding the damage states (DS) for the range of GLI values calculated for certain failure mechanisms (e.g., stretching, hogging, dishing). This is likely due to too few records observed and differences between surveys across events based on observed classification (e.g., tilting recorded at earlier survey and later survey classifying mechanism as global settlement with the same severity). However, a few of the failure mechanisms for larger failure types (e.g., global settlement) were generally better predicted by geospatial models. This held true for each of the shallow-foundation sub-types investigated.

Additionally, the worst severity observed over any failure mechanism was used to develop a set of fragility functions for a worst case for the foundation type. This would be more useful in predicting damage for building inventories. In most cases, this worst case for all failure mechanisms could not develop “minor” damage curves but it could reasonably capture higher damage severities.

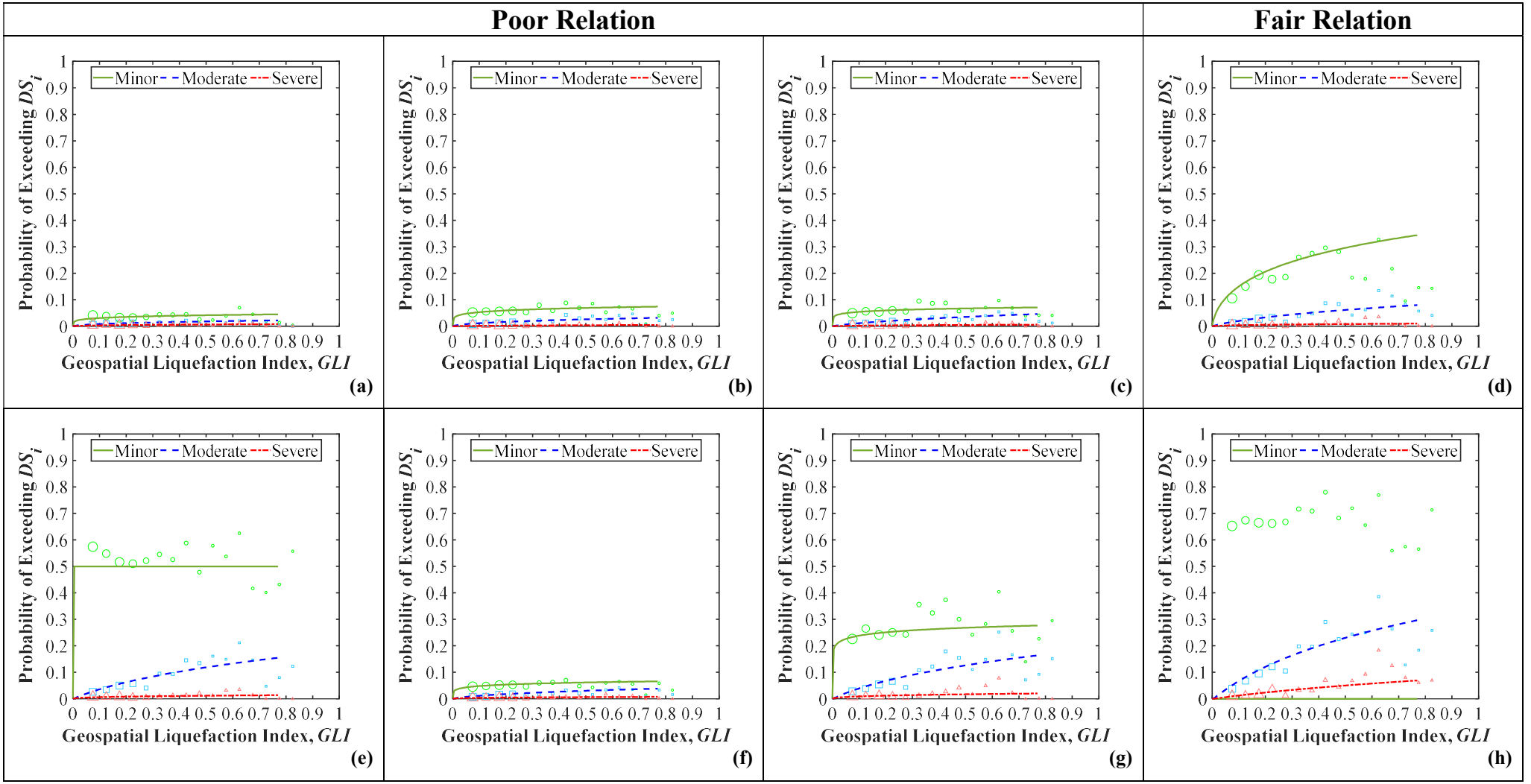

Figure 3.6 Fragility functions for predicting the probability of damage to shallow foundations (All variants) using regional geospatial model 2015 RGM3: (a) stretching failure; (b) hogging failure; (c) dishing failure; (d) global settlement failure; (e) twisting failure; (f) discontinuous foundation failure; (g) tilting failure; (h) the failure mode with greatest observed severity.

3.12 VULNERABILITY FUNCTION METHODOLOGY

While fragility functions can be a pragmatic tool for estimating damage to infrastructure, different assets (e.g., different types of buildings) have different sensitivities to ground deformation and it is thus ideal to use functions that directly predict damage and loss for the specific asset types (e.g., a particular type of foundation system). Considering loss, predictions are commonly made using a vulnerability function, which relates losses resulting from a hazard to parameters that characterize the hazard's demand. Specifically, for a site at which liquefaction resulted in losses: (1) the liquefaction response of the site must be characterized; (2) the design and value of infrastructure assets must be documented; and (3) the asset damage resulting from liquefaction must be quantified monetarily. Problematically, damage and loss are usually assessed by private insurance companies and are closely guarded by insurers (e.g., to protect proprietary data) and owners (e.g., to protect the value of real estate). The paucity of infrastructure-specific data has prevented earlier methods to predict liquefaction from being further developed to predict its downstream effects. With the new availability of the New Zealand dataset these downstream losses can finally be investigated.

There are a number of methods to develop vulnerability functions, the most desirable from a risk management viewpoint being those empirically derived from observations of the actual performance of assets in real earthquakes. Empirical observations can be too few or not provide enough detail as to distinguish between different damage manifestations, the resulting damage cost may still be relatable. The dataset of BDR records was compared to both models' calculated GLI and regression analysis was performed to formulate a vulnerability function. The results are shown in Figure 3.7 and 3.8 along with 84^{th} and 16^{th} percentiles for the data points. Additional graphs with comparisons of vulnerability functions by foundation type are also included in the appendix.

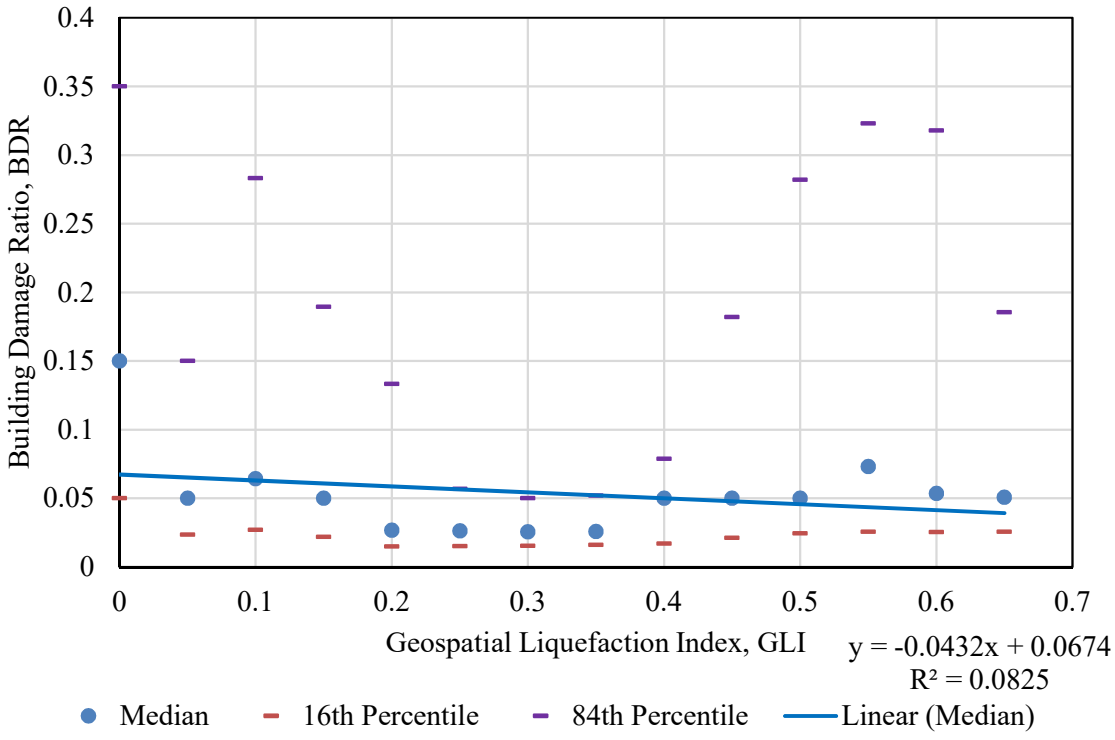

Figure 3.7 2017 GGM2 model GLI and BDR relation.

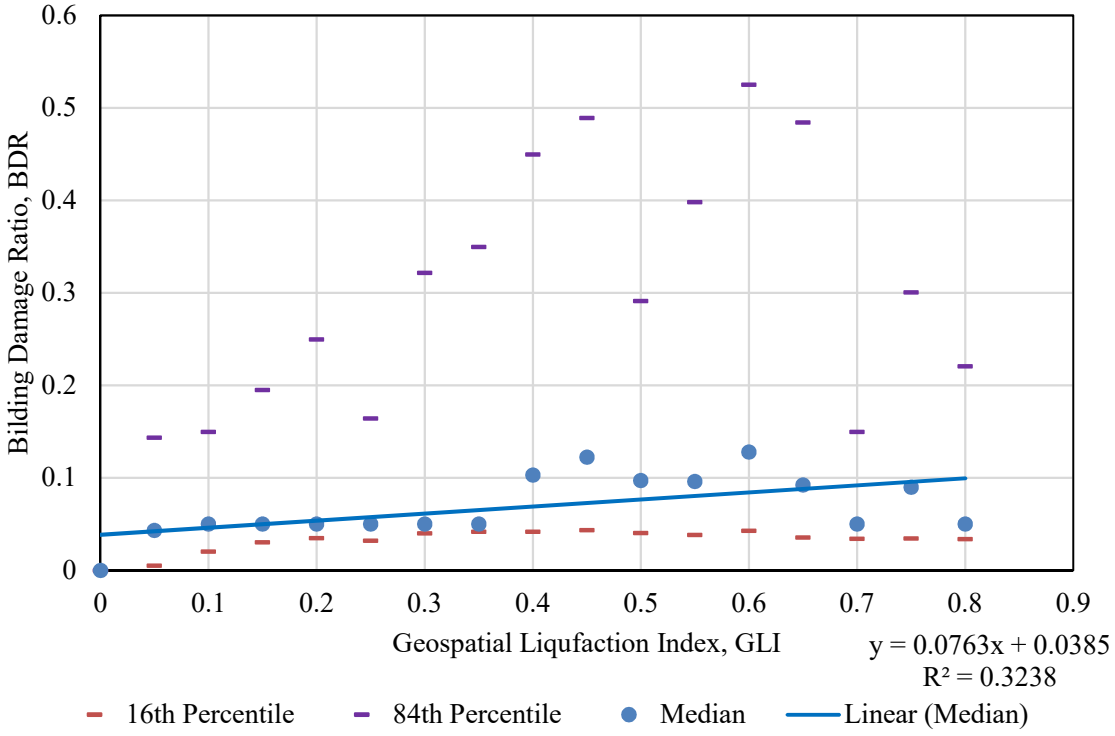

Figure 3.8 2015 RGM3 model GLI and BDR relation.

The data across the events varies considerably and the GLI relation is poor in capturing the higher range of BDR. Looking at the median data, the GLI relationship using the 2015 RGM3 model may be useful however in rapid prediction of low estimates of losses. It may be that the coarse resolution of the geospatial parameters is unable to fully capture the finer scale damage mechanisms that relate to higher BDR values.

3.13 Results and Discussion

The CES has provided an unprecedented quantity of high-quality liquefaction case history data and the opportunity to test the efficacity of liquefaction analytical models and their ability to predict infrastructure damage and loss. The development of geospatial models has opened an avenue for cost effective and rapid assessment of liquefaction potential. Their fair performance to predict the manifestation of liquefaction in the Christchurch, New Zealand region is encouraging. There is the potential for improvement as seen by their poorer performance in relating down to the finer scale of foundation failure mechanism, but they can capture larger failure types (e.g., global settlement). While the coarse resolution of the GLI can be improved, the 2015 RGM3 model shows potential and can be used for preliminary rapid damage estimates. As geospatial models are further refined and regional variations better accounted for, these relations should be able to improve and increase their portability around the globe.

Chapter 4. CONCLUSION

The previous two chapters have covered many topics with some key findings. *First*, geotechnical models were shown to be significantly more efficient on a global scale, however geospatial models performed equally well for the regional Canterbury dataset. Considering the time- and cost-requirements of geospatial models this result is provocative for their use to assess liquefaction hazards, however further research is needed to improve their portability. *Second*, successive geotechnical models proposed over the last twenty years show little or no demonstrable improvement for the two datasets analyzed and new innovation is needed if this trend is to improve. *Third*, when looking at the Canterbury dataset the geospatial models perform well in predicting the occurrence and severity of liquefaction ejecta but are less capable of predicting the magnitude of resulting ground settlement. They also preformed fairly well in predicting the severity of certain large-scale shallow foundation damage mechanisms (e.g., global settlement) but fail to capture other important damage mechanisms. *Fourth*, the geospatial models were rather poor predictors of high BDR values but can provide some low-end estimates for preliminary rapid damage estimates.

4.1 FURTHER RESEARCH

In the course of this research, a few topics were identified where further investigation is needed. When evaluating the performance of the geospatial and geotechnical models for the Canterbury dataset (Figure 4.1), it was observed that geotechnical models performed better than geospatial models at sites with relatively homogenous sand, but worse at profiles with interbedded silts and clays (Geyin et al., 2019b). Further study of why these layers of silty soils cause an overprediction of manifestations would be beneficial. Additionally, advances in available

geospatial data sources were analyzed for improving model efficiency (Figure 4.2) and there is potential for further refining the geospatial models (Baird et al., 2018).

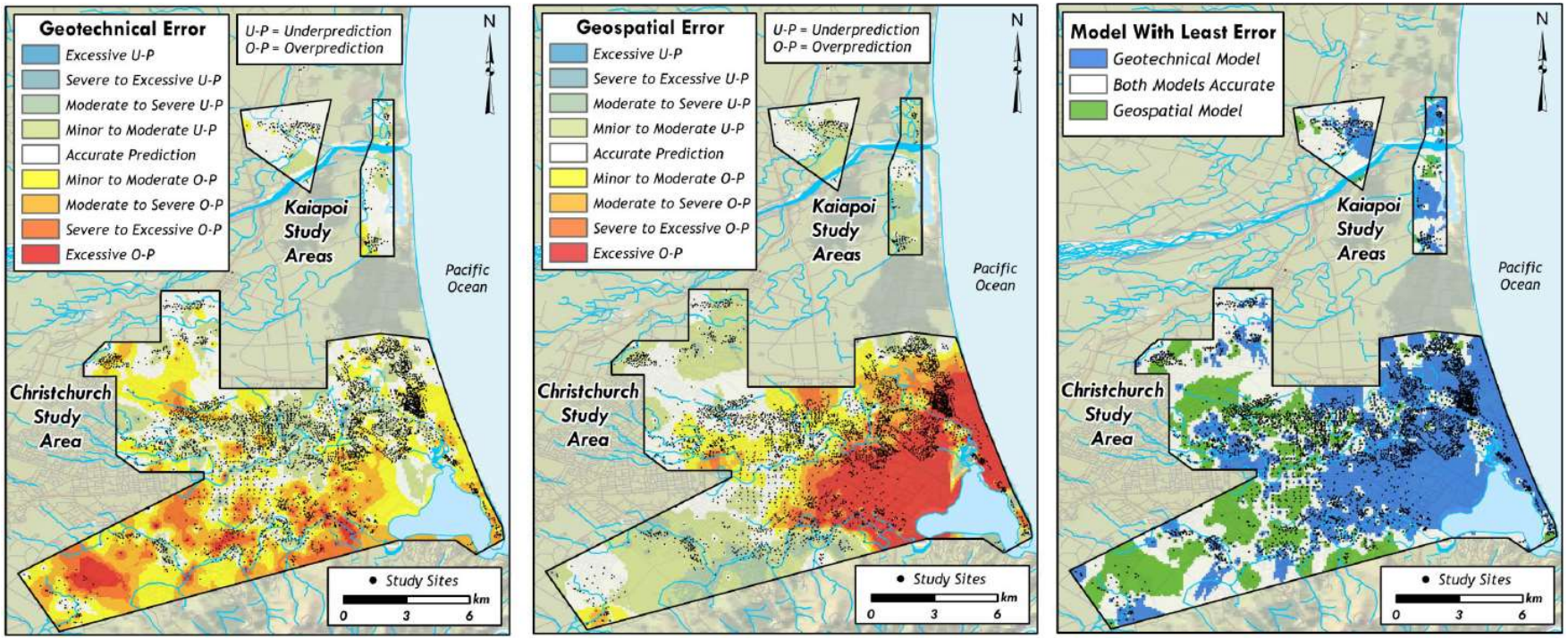

Figure 4.1 2015 RGM3 model GLI and BDR relation.

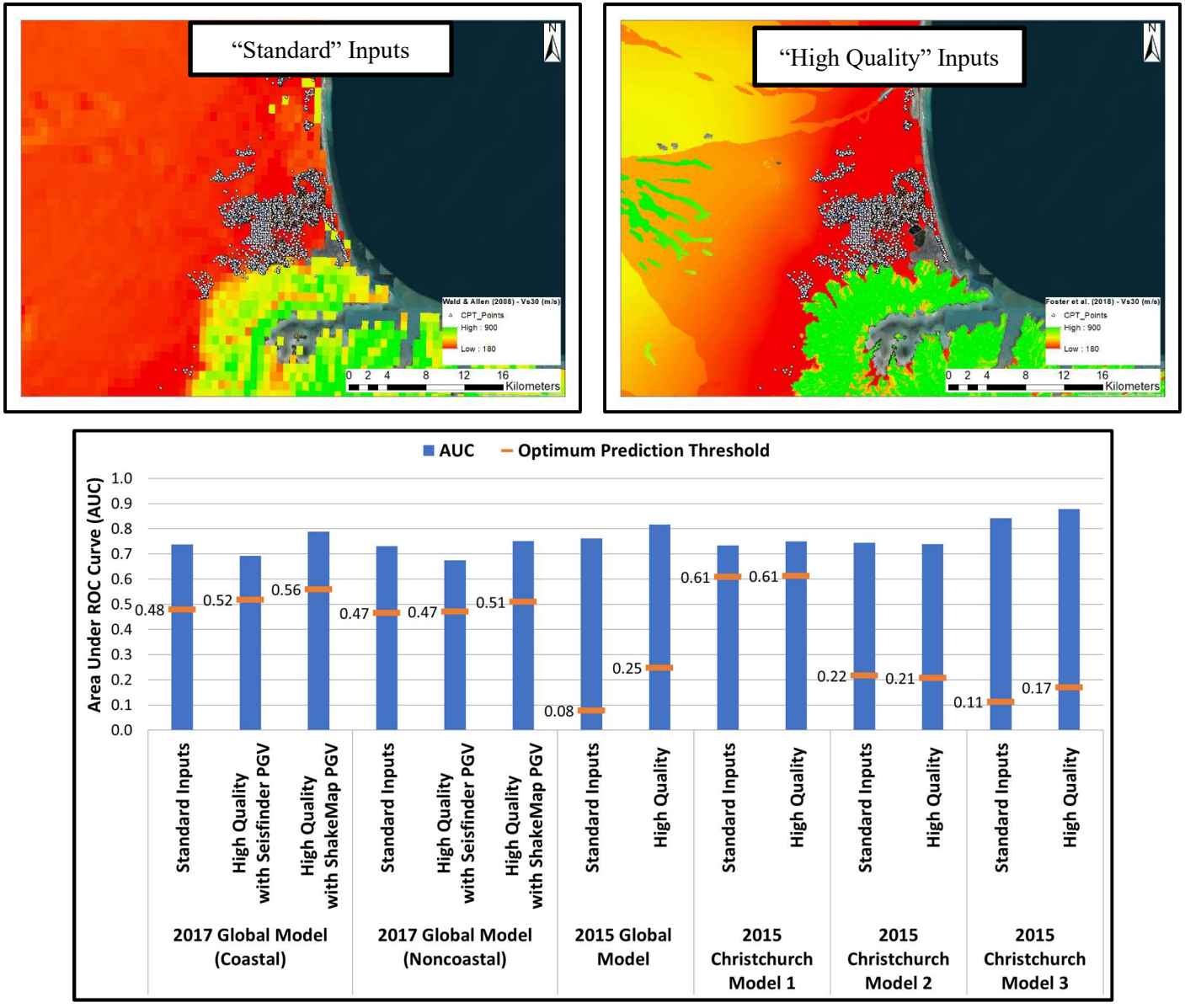

Figure 4.2 Alternate geospatial input parameters and model performance.

BIBLIOGRAPHY

Abdel-Haq, A., and Hryciw, R. D., 1998. Ground settlement in Simi Valley following the Northridge earthquake, *Journal of Geotechnical and Geoenvironmental*, **124**(1): 80-89.

Andrus, R.D., 1986. Subsurface investigations on a liquefaction induced lateral spread, Thousand Springs Valley, Idaho: liquefaction recurrence and a case history in gravel. M.S. Thesis, Dept. of Civil Engineering, Brigham Young University, Provo, Utah.

Allstadt, K.E., Thompson, E.M., Heame, M., Wald, D.J., Fee, J.M., Martinez, E.M., Hunter, E., and Brown, J.D., 2019. *Seismological Society of America Annual Meeting*, Seattle, WA.

Andrus, R. D. and Youd, T. L. 1987. Subsurface investigation of a liquefaction-induced lateral spread Thousand Springs Valley, Idaho. Misc. paper GL-87-8, U.S. Army Corps of Engineers.

Anselin, L., 1995. "Local Indicators of Spatial Association—LISA." *Geographical Analysis*, 27(2): 93–115.

Architectural Institute of Japan, 2001. *Recommendations for design of building foundations*, 486 p. [in Japanese]

Arulanandan, K., Yogachandran, C., Meegoda, N.J., Ying, L., and Zhauji, S., 1986. Comparison of the SPT, CPT, SV and electrical methods of evaluating earthquake induced liquefaction susceptibility in Ying Kou City during the Haicheng Earthquake. *Use of in situ tests in geotechnical engineering*, *Geotechnical Special Publication* **6**: 389–415.

Baird, A., Geyin, M., and Maurer, B.W., 2018. On the relationship between geospatial liquefaction-model performance and quality of geospatial data: a case study of the 2010-2016 Canterbury earthquakes, *New Zealand Centre for Earthquake Resilience Annual Meeting*, Sept 4-6; Taupo.

Batilas, A., Pelekis, P., Vlachakis, V., and Athanasopoulos, G. 2014. Soil Liquefaction/ Nonliquefaction in the Achaia-Ilia (Greece) 2008 Earthquake: field evidence, site characterization and ground motion assessment, *International Journal of Geoengineering Case histories*, **2**(4): 270-287.

Bennett, M.J., McLaughlin, P.V., Sarmiento, J.S., and Youd, T. L., 1984. Geotechnical investigation of liquefaction sites, Imperial Valley, California. U.S. Geological Survey, Open-File Report 84-252, 103 pp.

Bennett, M.J., and Tinsley, J.C., III, 1995. Geotechnical data from surface and subsurface samples outside of and within liquefaction-related ground failures caused by the October 17, 1989, Loma Prieta earthquake, Santa Cruz and Monterey Counties, California. U.S. Geological Survey Open-File Rep. 95-663, U.S. Geological Survey.

Bennett, M.J., Ponti, D.J., Tinsley, J.C., III, Holzer, T.L., and Conaway, C.H., 1998. Subsurface geotechnical investigations near sites of ground deformations caused by the January 17, 1994, Northridge, California, earthquake. U.S. Geological Survey, Open-file report 98-373, 148 pp.

Beven, K. J., and M. J. Kirkby, 1979. A physically based, variable contributing area model of basin hydrology, Hydrol. Sci. Bull. 24, 43–69.

Boulanger, R.W., Idriss, I.M., and Mejia, L.H., 1995. Investigation and evaluation of liquefaction related ground displacements at Moss Landing during the 1989 Loma Prieta earthquake. Report No. UCD/CGM-95/02, Center for Geotechnical Modeling, Dept. of Civil & Environmental Engineering, University of California, Davis, 231 pp.

Boulanger, R.W., Mejia, L.H., and Idriss, I.M., 1997. Liquefaction at Moss Landing during Loma Prieta earthquake. *Journal of Geotechnical and Geoenvironmental Engineering,* **123**(5): 453–67.

Boulanger, R.W. and Idriss, I.M., 2014. *CPT and SPT Based Liquefaction Triggering Procedures, Report No. UCD/CGM-14/01*, Center for Geotechnical Modeling, Department of Civil and Environmental Engineering, University of California, Davis, CA.

Bradley, B.A., 2013. "A New Zealand-specific pseudo-spectral acceleration ground-motion prediction equation for active shallow crustal earthquakes based on foreign models." Bulletin of the Seismological Society of America; 103(3): 1801-1822.

Bradley BA, Razafindrakoto HNT, Maurer BW, Motha J, Tarbali K, Lee RL., 2018. Simulation-based ground motion prediction of historical and future New Zealand earthquakes and consequent geohazard impacts. Geotechnical Earthquake Engineering and Soil Dynamics V. 10-13 June 2018. Austin, Texas. 15pp.

Bray, J.D. and Macedo, J., 2017. Simplified procedure for estimating liquefaction-induced building settlement, *Soil Dynamics and Earthquake Engineering*, **102**, 215-231.

Buck, J.R., Daniel, M.M, and Singer, A.C, 2002. *Computer Explorations in Signals and Systems Using MATLAB®,* 2nd Edition. Upper Saddle River, NJ: Prentice Hall.

Bullock, Z., Karimi, Z., Dashti, S., Porter, K., Liel, A.B., and Franke, K.W., 2018. A physics-informed semi-empirical probabilistic model for the settlement of shallow-founded structures on liquefiable ground, *Géotechnique*, doi.org/10.1680/jgeot.17.P.174.

Byrne, P.M., Park, S.S., Beaty, M., Sharp, M.K., Gonzalez, L., Abdoun, T., 2004. Numerical modeling of liquefaction and comparison with centrifuge tests, *Canadian Geotechnical Journal*, **41**(2), 193-211.

Canterbury Geotechnical Database (CDG), 2012. "Aerial Photography," Map Layer CGD0100 - 1 June 2012, retrieved [12/12] from https://canterburygeotechnicaldatabase. projectorbit.com

CERA (Canterbury Earthquake Recovery Authority), 2012. Purpose and scope of the Canterbury geotechnical database (renamed the New Zealand Geotechnical Database as of 2019). Retrieved from www.nzgd.org.nz.

CESMD (Center for Engineering Strong Motion Data), 2016. U.S. structural and ground response data. Retrieved from http://www.strongmotioncenter.org/

Cetin, K.O., Seed, R.B., Moss, R.E.S., Der Kiureghian, A.K., Tokimatsu, K., Harder, L.F., and Kayen, R.E., 2000. Field Performance Case Histories for SPT-Based Evaluation of Soil Liquefaction Triggering Hazard, Geotechnical Engineering Research Report No. UCB/GT-2000/09, Department of Civil Engineering, UC Berkeley.

Cetin, K.O., Bilge, H.T., Wu, J, Kammerer, A.M., and Seed, R.B., 2009. Probabilistic model for the assessment of cyclically induced reconsolidation (Volumetric) Settlements, *Journal of Geotechnical and Geoenvironmental Engineering*, **135**(3), 387-398.

Christensen, S.A., 1995. Liquefaction of cohesionless soils in the March 2, 1987 Edgecumbe earthquake, Bay of Plenty, New Zealand, and other earthquakes, Master of Engineering Thesis, Department of Civil Engineering, University of Canterbury, Christchurch, New Zealand.

Cox, B.R., Boulanger, R.W., Tokimatsu, K., Wood, C., Abe, A., Ashford, S., Donahue, J., Ishihara, K., Kayen, R., Katsumata, K., Kishida, T., Kokusho, T., Mason, B., Moss, R., Stewart, J., Tohyama, K., and Zekkos, D., 2013. Liquefaction at strong motion stations in Urayasu City during the 2011 Tohoku-Oki earthquake." *Earthquake Spectra*, **29**(S1): S55-S80.

Cubrinovski, M. and Ishihara, K., 1998. State concept and modified elastoplasticity for sand modeling, *Soils and Foundations*, **38**(4), 213-225.

DeLong, E.R., DeLong, D.M., Clarke-Pearson, D.L., 1988. Comparing the areas under two or more correlated receiver operating characteristic curves: a nonparametric approach. *Biometrics* **44**: 837-845

Diaz-Rodriquez, J.A., 1984. Liquefaction in the Mexicali Valley during the earthquake of June 9, 1980, *Eighth World Conference on Earthquake Engineering*, San Francisco, 223-230.

Diaz-Rodriquez, J.A., and Armijo-Palacio, G., 1991. Liquefaction potential of fine cohesionless soils using the CPT, *Soils and Foundations*, **31**(3): 111-119.

Facciorusso, J., Madiai, C., and Vannucchi, G., 2015. CPT-Based Liquefaction Case History from the 2012 Emilia Earthquake in Italy, *Journal of Geotechnical and Geoenvironmental Engineering,* **141**(12): 05015002.

Farrar, J.A., 1990. Study of in situ testing for evaluation of liquefaction resistance, R-90-06, U.S. Department of the Interior, Bureau of Reclamation, Research and Laboratory Services Division, Geotechnical Services Branch, Denver Office.

Fawcett, T., 2006. An introduction to ROC analysis, *Pattern Recognition Letters,* **27**(8): 861–874.

Federal Emergency Management Agency (FEMA), 2013. *Earthquake Model HAZUS-MH 2.1 Technical Manual*, Washington, D.C.

Fick, S. E., and Hijmans, R. J., 2017. WorldClim 2: new 1-km spatial resolution climate surfaces for global land areas. *International journal of climatology*, **37**(12): 4302-4315.

Geyin, M., and Maurer, B.W., 2019a. An analysis of liquefaction-induced free-field ground settlement using 1,000+ case-histories: observations vs. state-of-practice predictions. *Proceedings of Geocongress 2019, Geotechnical Special Publication*, In Press.

Geyin, M., Baird, A., and Maurer, B.W., 2019b. A Performance Comparison of Relatively Simple and Complex Models for Predicting Soil Liquefaction using 15,000+ Case Histories from 24 Earthquakes. *Geocongress 2019*. March 24-27. Philadelphia.

Green, R.A., Cubrinovski, M., Cox, B., Wood, C., Wotherspoon, L., Bradley, B., & Maurer, B.W., 2014. "Select Liquefaction Case Histories from the 2010-2011 Canterbury Earthquake Sequence." Earthquake Spectra, 30(1): 131-153.

Green, R.A., Cubrinovski, M., Cox, B., Wood, C., Wotherspoon, L., Bradley, B., Maurer, B., 2018. Select Liquefaction Case Histories from the 2010-2011 Canterbury Earthquake Sequence. Earthquake Spectra 2014; 30(1): 131-153.

Holzer, T.L., Bennett, M.J., Ponti, D.J., and Tinsley, J.C., 1999. Liquefaction and soil failure during 1994 Northridge earthquake, *Journal of Geotechnical and Geoenvironmental Engineering*, **125**(6): 438-452.

Holzer, T.L., and Youd, T.L., 2007. Liquefaction, ground oscillation, and soil deformation at the wildlife array, California, *Bulletin of the Seismological Society of America*, **97**(3): 961-976.

Idriss, I.M. and Boulanger, R.W., 2008. *Soil liquefaction during earthquakes*, Monograph MNO-12, Earthquake Engineering Research Institute, Oakland, CA, 261 pp.

Ishihara, K., 1985. Stability of natural deposits during earthquakes, *11th International Conference on Soil Mechanics and Foundation Engineering*, San Francisco, CA, USA, **1**: 321-376.

Ishihara, K., and Koga, Y., 1981. Case studies of liquefaction in the 1964 Niigata earthquake, *Soils and Foundations*, **21**(3): 35-52.

Iwasaki, T., Tatsuoka, F., Tokida, K., and Yasuda, S., 1978. A practical method for assessing soil liquefaction potential based on case studies at various sites in Japan, *2nd Intl Conf. Microzonation*, San Francisco, CA.

Kayen, R.E., Mitchell, J.K., Seed, R.B., and Nishio, S., 1998. Soil liquefaction in the east bay during the earthquake*, The Loma Prieta, California, Earthquake of October 17, 1989 – Liquefaction*. Thomas L. Holzer, editor, USGS Professional Paper 1551-B, B61-B86.

Kayen, R.E., Moss, R.E.S., Thompson, E.M., Seed, R.B., Cetin, O.K., Der Kiureghian, A., Tanaka, Y., and Tokimatsu, T., 2013. Shear wave velocity-based probabilistic and deterministic assessment of seismic soil liquefaction potential, *Journal of Geotechnical and Geoenvironmental Engineering*, **139**(3), 407-419.

Lee, D.H., Ku, C.S., and Juang, C.H., 2000. Preliminary investigation of soil liquefaction in the

1999 Chi-Chi, Taiwan, earthquake, *International Workshop on Annual Commemoration of Chi-Chi Earthquake, Vol. III – Geotechnical Aspect*, C.H. Loh and W.I. Liao, eds., National Center for Research on Earthquake Engineering, Taipei, Taiwan, pp. 140-151.

Lehner, B., Verdin, K., and Jarvis, A., 2006. HydroSHEDS Technical Documentation, World Wildlife Fund US, Washington, D.C.

Kramer, S.L., 2008. *Evaluation of Liquefaction Hazards in Washington State, Report No. WA-RD 668.1*, Washington State Transportation Center, Seattle, Washington.

Maurer, B.W., Green, R.A., Cubrinovski, M., and Bradley, B.A., 2014a. Evaluation of the liquefaction potential index for assessing liquefaction hazard in Christchurch, New Zealand. *Journal of Geotechnical and Geoenvironmental Engineering* **140**(7), 04014032.

Maurer, B.W., Green, R.A., Cubrinovski, M., and Bradley, B.A., 2014b. Assessment of aging correction factors for liquefaction resistance at sites of recurrent liquefaction, *10th U.S. National Conference on Earthquake Engineering,* July 20-26, Anchorage, USA.

Maurer, B.W., Green, R.A., and Taylor, O.D.S., 2015a. Moving towards an improved index for assessing liquefaction hazard: lessons from historical data. *Soils and Foundations* **55**(4), 778-787.

Maurer, B.W., Green, R.A., Cubrinovski, M., Bradley, B.A., 2015b. Fines-content effects on liquefaction hazard evaluation for infrastructure during the 2010-2011 Canterbury, New Zealand earthquake sequence. *Soil Dynamics and Earthquake Engineering*, **76**, 58-68.

Maurer, B.W., van Ballegooy, S., and Bradley, B.A., 2017. Fragility functions for performance-based damage assessment of soil liquefaction, *3rd International Conference on Performance-based Design in Earthquake Geotechnical Engineering,* July 16-19; Vancouver, Canada.

Maurer, B.W., Green, R.A., van Ballegooy, S., and Wotherspoon, L., 2019. Development of region-specific soil behavior type index correlations for evaluating liquefaction hazard in Christchurch, New Zealand. *Soil Dynamics and Earthquake Engineering*, **117**, 96-105.

Mitchell, J.K., Lodge, A.L., Coutinho, R.Q., Kayen, R.E., Seed, R.B., Nishio, S., and Stokoe, K. H., II, 1994. Insitu test results from four Loma Prieta earthquake liquefaction sites: SPT, CPT, DMT and shear wave velocity. Report No. UCB/EERC-94/04. Earthquake Engineering Research Center, UC Berkeley.

Moss, R.E.S., Seed, R.B., Kayen, R.E., Stewart, J. P., Youd, T.L., and Tokimatsu, K., 2003. Field case histories for CPT-based in situ liquefaction potential evaluation. Geoengineering Research Rep. UCB/GE-2003/04.

Moss, R.E.S., Collins, B.D., and Whang, D.H., 2005. Retesting of liquefaction/nonliquefaction case histories in the imperial valley. *EQ Spectra*, **21**(1): 179–196.

Moss, R.E.S, Seed, R.B., Kayen, R.E., Stewart, J.P., Der Kiureghian, A., and Cetin, K.O., 2006. "CPT-based probabilistic and deterministic assessment of in situ seismic soil liquefaction potential." Journal of Geotechnical and Geoenvironmental Engineering, ASCE, 132(8):1032-1051.

Moss, R.E.S., Kayen, R.E., Tong, L.-Y., Liu, S.-Y., Cai, G.-J., and Wu, J., 2009. Re-investigation of liquefaction and nonliquefaction case histories from the 1976 Tangshan earthquake. Rep. No. 209/102, Pacific Earthquake Engineering Research (PEER) Center, Berkeley, CA.

Moss, R.E.S., Kayen, R.E., Tong, L.-Y., Liu, S.-Y., Cai, G.-J., and Wu, J., 2011. Retesting of liquefaction and nonliquefaction case histories from the 1976 Tangshan earthquake, *Journal of Geotechnical and Geoenvironmental Engineering*, **137**(4): 334-343.

Nakata, T. and Shimazaki, K., 1997. Geo-slicer, a newly invented soil sampler, for high-resolution active fault studies. *Journal of Geography*, **106**(1): 59-69 (in Japanese).

National Research Council (NRC), 2016. *State of the Art and Practice in the Assessment of Earthquake-Induced Soil Liquefaction and its Consequences*, Committee on Earthquake Induced Soil Liquefaction Assessment (Members: Edward Kavazanjian, Jr., Chair, Jose E. Andrade, Kandian "Arul" Arulmoli, Brian F. Atwater, John T. Christian, Russell A. Green, Steven L. Kramer, Lelio Mejia, James K. Mitchell, Ellen Rathje, James R. Rice, and Yumie Wang), The National Academies Press, Washington, DC.

Papathanassiou, G., Mantovani, A., Tarabusi, G., Rapti, D., and Caputo, R., 2015. Assessment of liquefaction potential for two liquefaction prone areas considering the May 20, 2012 Emilia (Italy) earthquake, *Engineering Geology*, **189**:1-16.

Parker, M. and Steenkamp, D., 2012. "The economic impact of the Canterbury earthquakes." Bulletin of the Reserve Bank of New Zealand, 75(3): 13-25.

Pass, D.G., 1994. Soil characterization of the deep accelerometer site at Treasure Island, San

Francisco, California. MS thesis, University of New Hampshire.

PEER (Pacific Earthquake Engineering Research Center), 2000a. Documenting incidents of ground failure resulting from the 1999, Kocaeli, Turkey Earthquake. http://peer.berkeley.edu/ publications/turkey/adapazari/

PEER (Pacific Earthquake Engineering Research Center), 2000b. Documentation of soil conditions at liquefaction sites from 1999 Chi-Chi, Taiwan Earthquake. http://peer.berkeley. edu/ lifelines/research _projects/3A02/

Porter, K. A., Scawthorn, C. R., and Beck, J. L., 2006. "Cost-effectiveness of stronger woodframe buildings." Earthquake Spectra, 22: 239–266.

Provost, F. and Fawcett, T., 2001. "Robust classification for imprecise environments." Machine Learning, 42 (3): 203–231.Quigley, M., Hughes, M.W., Bradley, B.A., van Ballegooy S., Reid, C., Morgenroth, J., Horton, T., Duffy, B., Pettinga, J, 2016. The 2010-2011 Canterbury earthquake sequence: Environmental effects, seismic triggering thresholds, geologic legacy. *Tectonophysics*, **672-673**, 228-274.

Raschke, S.A., and Hryciw, R.D., 1997. Vision cone penetrometer for direct subsurface soil observation, *Journal of Geotechnical and Geoenvironmental Engineering*, **123**(11), 1074-1076.

Robertson, P.K. and Wride, C.E., 1998. "Evaluating cyclic liquefaction potential using cone penetration test." Canadian Geotechnical Journal 35(3): 442-459.

Seed, H.B. & Idriss, I.M., 1971. Simplified procedure for evaluating soil liquefaction potential, *ASCE Journal of Soil Mechanics and Foundations Division*, **97**(9), 1249–1273.

Seed, H. B., Tokimatsu, K., Harder, L. F. Jr., and Chung, R., 1984. The influence of SPT procedures in soil liquefaction resistance evaluations. Report No. UCB/EERC-84/15. Earthquake Engineering Research Center, University of California, Berkeley.

Servizio Geologico, 2016. Database of the Emilia-Romagna region: geological, seismic, and soil Survey." http://ambiente.regione.emiliaromagna.it/geologia/cartografia/webgis-banchedati/ (in Italian).

Shengcong, F. and Tatsuoka, F., 1984. Soil liquefaction during Haicheng and Tangshan earthquake

in China; a review, *Soils and Foundations*, **24**(4): 11-29.

Shibata, T., and Teparaska, W., 1988. Evaluation of Liquefaction Potential of Soils Using Cone Penetration Testing. *Soils and Foundations*, **28**(2): 49-60.

Strahler, A. N., 1952. Hypsometric (area-altitude) analysis of erosional topology, *Geological Society of America Bulletin*, **63**: 1117–1142

Suzuki, Y., Tokimatsu, K., Moss, R.E.S., Seed, R.B., and Kayen, R.E., 2003. CPT-based liquefaction case histories from the 1995 Hyogoken-Nambu (Kobe) earthquake, Japan. Geotechnical Engineering Research Report No. UCB/GE-2003/03.

Takada, K, and Atwater, B.F., 2004. Evidence for liquefaction identified in peeled slices of Holocene deposits along the lower Columbia River, Washington, *Bulletin of the Seismological Society of America*, **94**(2), 550-575.

Toprak, S., and Holzer, T.L., 2003. Liquefaction potential index: field assessment, *Journal of Geotechnical and Geoenvironmental Engineering* **129**(4): 315-322.

Turner, B., Brandenberg, S., and Stewart, J., 2016. "Case Study of Parallel Bridges Affected by Liquefaction and Lateral Spreading." *Journal of Geotechnical and Geoenvironmental Engineering*, **142**(7): 05016001.

U.S Geological Survey, 2018. ANSS Comprehensive Earthquake Catalog database available online at https://earthquake.usgs.gov/earthquakes/search/

van Ballegooy, S., Malan, P., Lacrosse, V., Jacka, M.E., Cubrinovski, M., Bray, J.D., O'Rourke, T.D., Crawford, S.A., and Cowan, H., 2014. Assessment of liquefaction-induced land damage for residential Christchurch, *Earthquake Spectra*, **30**(1), 31-55.

van Ballegooy, S., Green, R.A., Lees, J., Wentz, F., and Maurer, B.W., 2015. Assessment of various CPT based liquefaction severity index frameworks relative to the Ishihara (1985) H_1-H_2 boundary curves, *Soil Dynamics and Earthquake Engineering* **79**: 347-364.

Wald, D. J., and Allen, T. I., 2007. Topographic slope as a proxy for seismic site conditions and amplification, *Bulletin of the Seismological Society of America* **97**: 1379–1395.

Worden, C.B., and D.J. Wald, 2016. ShakeMap: technical manual, user's guide, and software guide, US Geological Survey, usgs.github.io/shakemap. DOI: 10.5066/F7D21VPQ.

Whitman, R.V., 1971. Resistance of soil to liquefaction and settlement, *Soils and Foundations,* **11**(4), 59–68.

Youd, T.L., and Hoose, S.N., 1977. Liquefaction Susceptibility and Geologic Setting, *Proceedings of the Sixth World Conference on Earthquake Engineering*, **3**, 2189-2194.

Youd, T. L., and D. M. Perkins, 1978. Mapping liquefaction-induced ground failure potential, J. Geotech. Eng. Div. 104, no. 4, Paper Number 13659, 433–446.

Youd, T.L., Idriss, I.M., Andrus, R.D., Arango, I., Castro, G., Christian, J.T., Dobry, R., Finn, W.D.L., Harder, L.F., Hynes, M.E. et al., 2001. Liquefaction resistance of soils: summary report from the 1996 NCEER and 1998 NCEER/NSF workshops on evaluation of liquefaction resistance of soils, *Journal of Geotechnical and Geoenvironmental Engineering*, **127**: 817–833

Youd, T.L., and Carter, B.L., 2005. Influence of soil softening and liquefaction on spectral acceleration, *Journal of Geotechnical and Geoenvironmental Engineering*, **131**(7): 811-825.

Youd, T.L., DeDen, D.W., Bray, J.D., Sancio, R., Cetin, K.O., and Gerber, T.M., 2009. Zero displacement lateral spreads, 1999 Kocaeli, Turkey, earthquake. *Journal of Geotechnical & Geoenvironmental Engineering*, **135**(1): 46-61.

Zhang, G., Robertson, P.K., and Brachman, R.W.I., 2002. "Estimating liquefaction-induced ground settlements from CPT for level ground." *Canadian Geotechnical Journal*, 39(5): 1168-1180.

Zhang, G., Robertson, P.K., and Brachman, R.W.I, 2004. Estimating liquefaction-induced lateral displacements using the standard penetration test or cone penetration test, *Journal of Geotechnical and Geoenvironmental Engineering*, **130**(8), 861-871.

Zhu, J., Daley, D., Baise, L.G., Thompson, E.M., Wald, D.J., and Knudsen, K.L., 2015. A geospatial liquefaction model for rapid response and loss estimation, *Earthquake Spectra* **31**(3), 1813-1837.

Zhu, J., Baise, L.G., and Thompson, E.M., 2017. An updated geospatial liquefaction model for global application, *Bulletin of the Seismological Society of America*, **107**(3), 1365-1385.

Ziotopoulou, K., and Boulanger, R.W., 2016. Plasticity modeling of liquefaction effects under sloping ground and irregular cyclic loading conditions, *Soil Dynamics and Earthquake Engineering*, **84**, 269-283.

Zou, K.H., 2007. Receiver operating characteristic (ROC) literature research. *On-line bibliography*, http://www.spl.harvard.edu/archive/spl-pre2007/pages/ppl/zou/roc.html

APPENDIX A

(1) Damage State vs. GLI by foundation

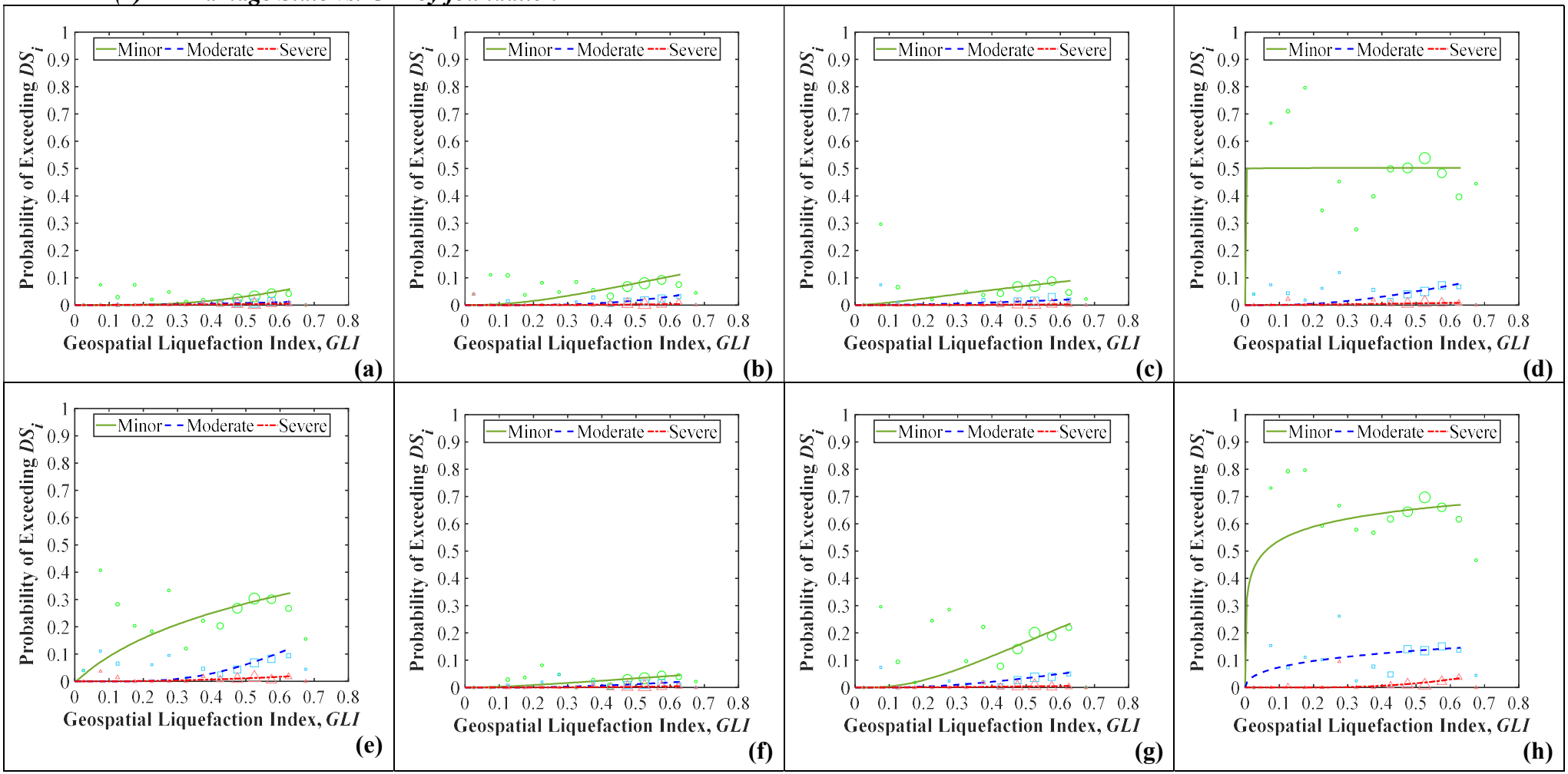

Figure 1 Fragility functions for predicting the probability of damage to Timber Floor on Pile foundations using regional geospatial model 2017 GGM2: (a) stretching failure; (b) hogging failure; (c) dishing failure; (d) twisting failure; (e) tilting failure; (f) discontinuous foundation failure; (g) global settlement failure; (h) the failure mode with greatest observed severity.

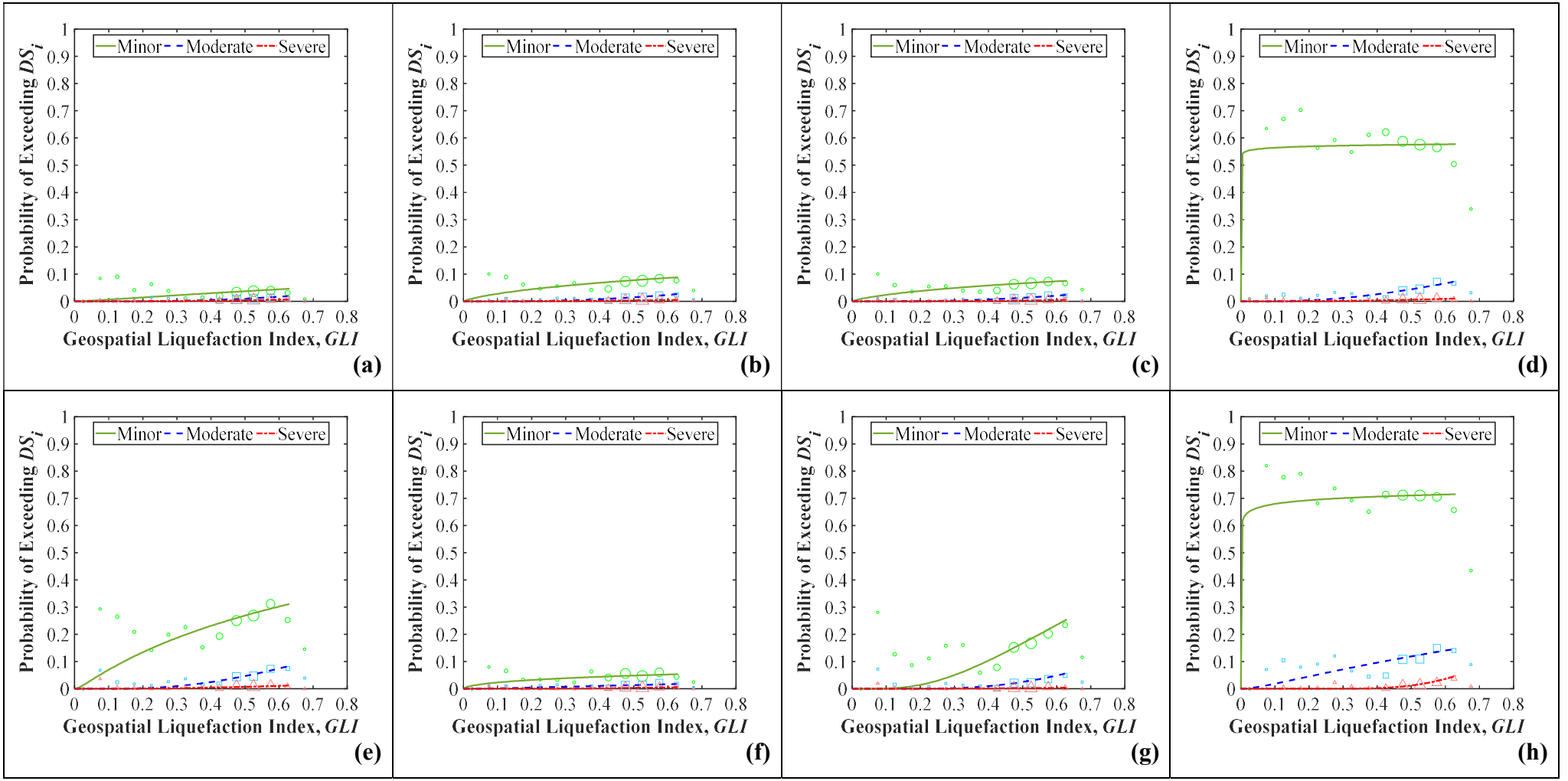

Figure 2 Fragility functions for predicting the probability of damage to Timber on Internal Piles with Perimeter Concrete Footing foundations using regional geospatial model 2017 GGM2: (a) stretching failure; (b) hogging failure; (c) dishing failure; (d) twisting failure; (e) tilting failure; (f) discontinuous foundation failure; (g) global settlement failure; (h) the failure mode with greatest observed severity.

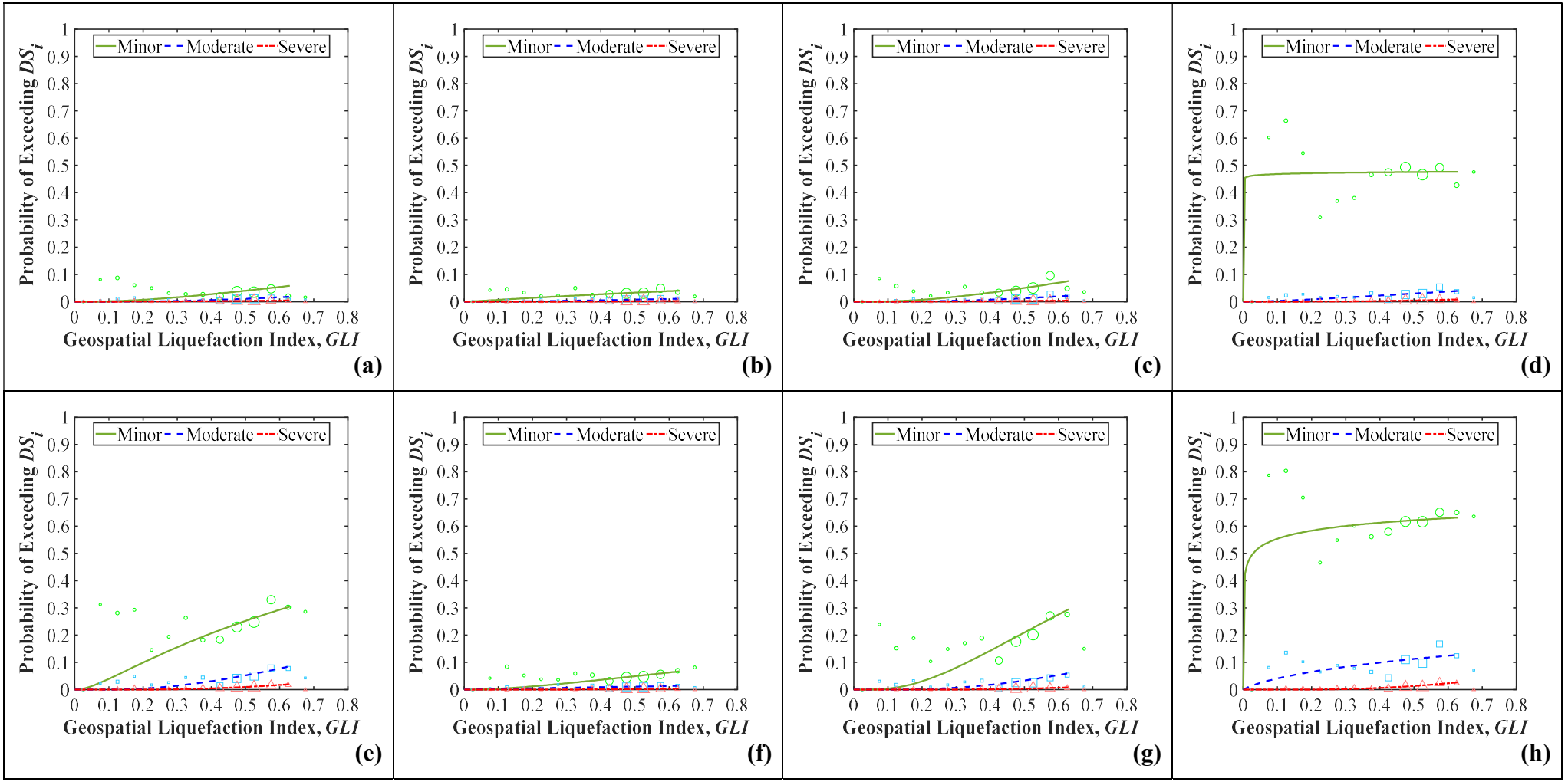

Figure 3 Fragility functions for predicting the probability of damage to Concrete Slab on Grade foundations using regional geospatial model 2017 GGM2: (a) stretching failure; (b) hogging failure; (c) dishing failure; (d) twisting failure; (e) tilting failure; (f) discontinuous foundation failure; (g) global settlement failure; (h) the failure mode with greatest observed severity.

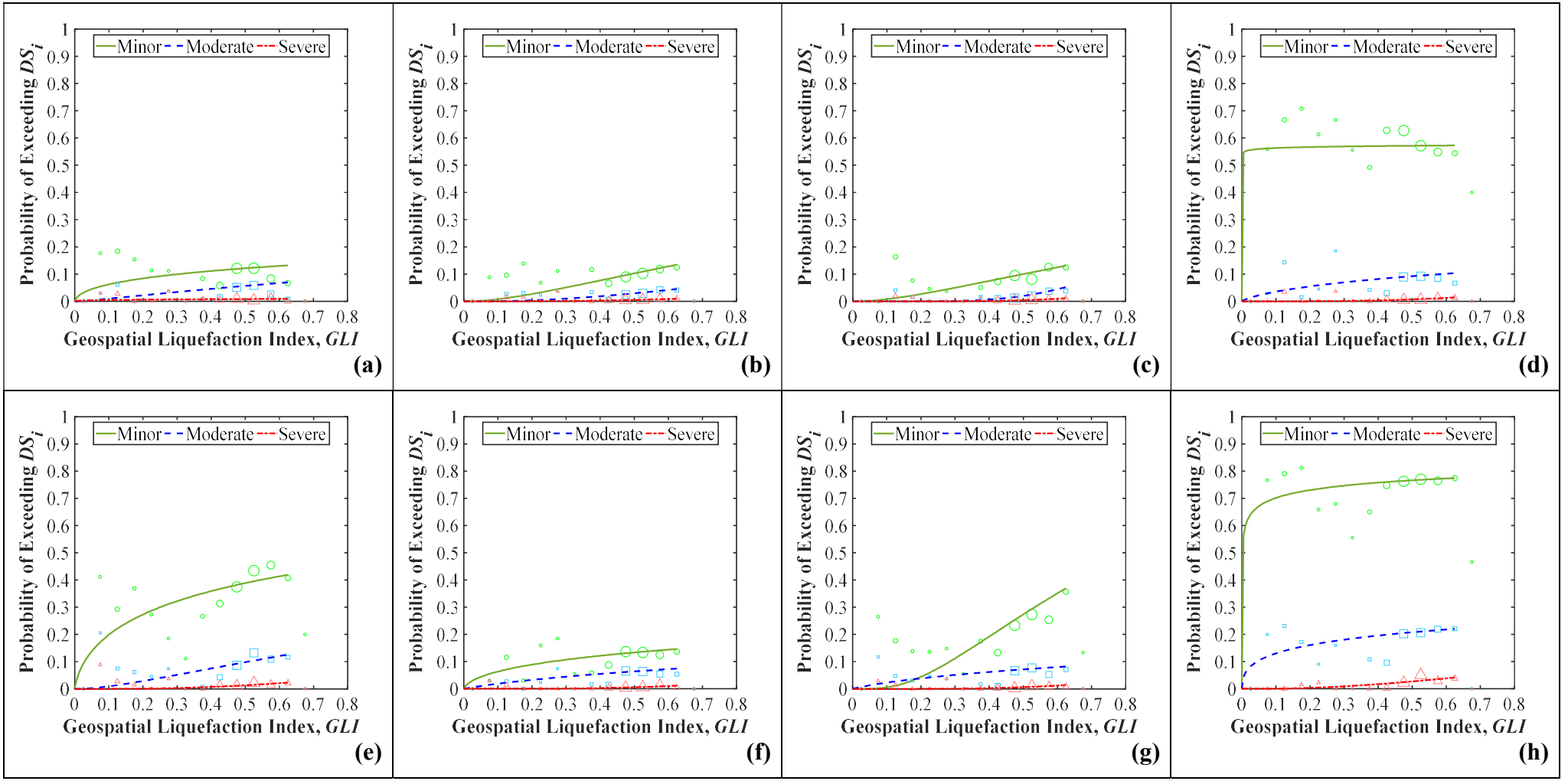

Figure 4 Fragility functions for predicting the probability of damage to Mixed foundations using regional geospatial model 2017 GGM2: (a) stretching failure; (b) hogging failure; (c) dishing failure; (d) twisting failure; (e) tilting failure; (f) discontinuous foundation failure; (g) global settlement failure; (h) the failure mode with greatest observed severity.

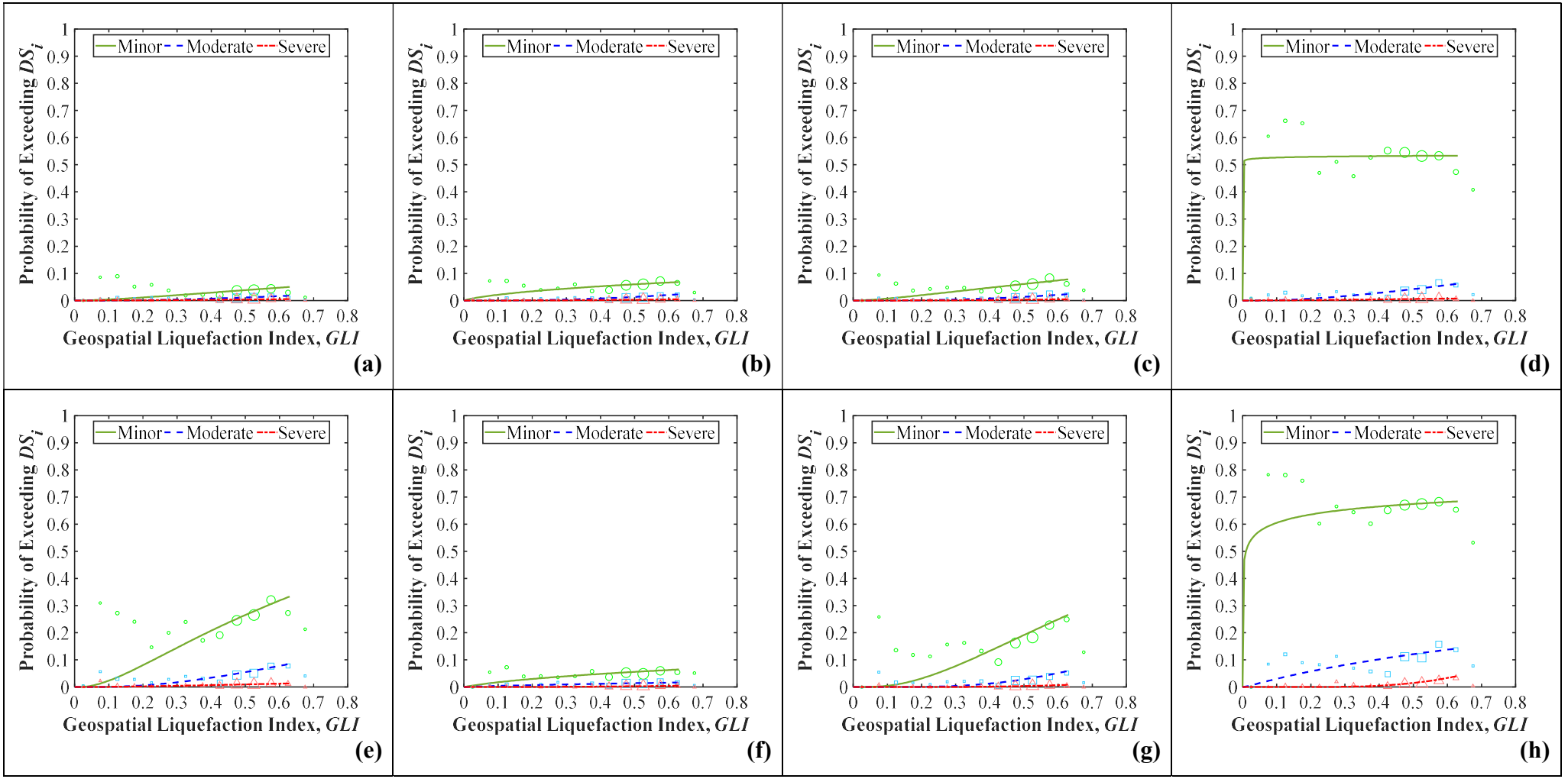

Figure 5 Fragility functions for predicting the probability of damage to shallow foundations (All variants) using regional geospatial model 2017 GGM2: (a) stretching failure; (b) hogging failure; (c) dishing failure; (d) twisting failure; (e) tilting failure; (f) discontinuous foundation failure; (g) global settlement failure; (h) the failure mode with greatest observed severity.

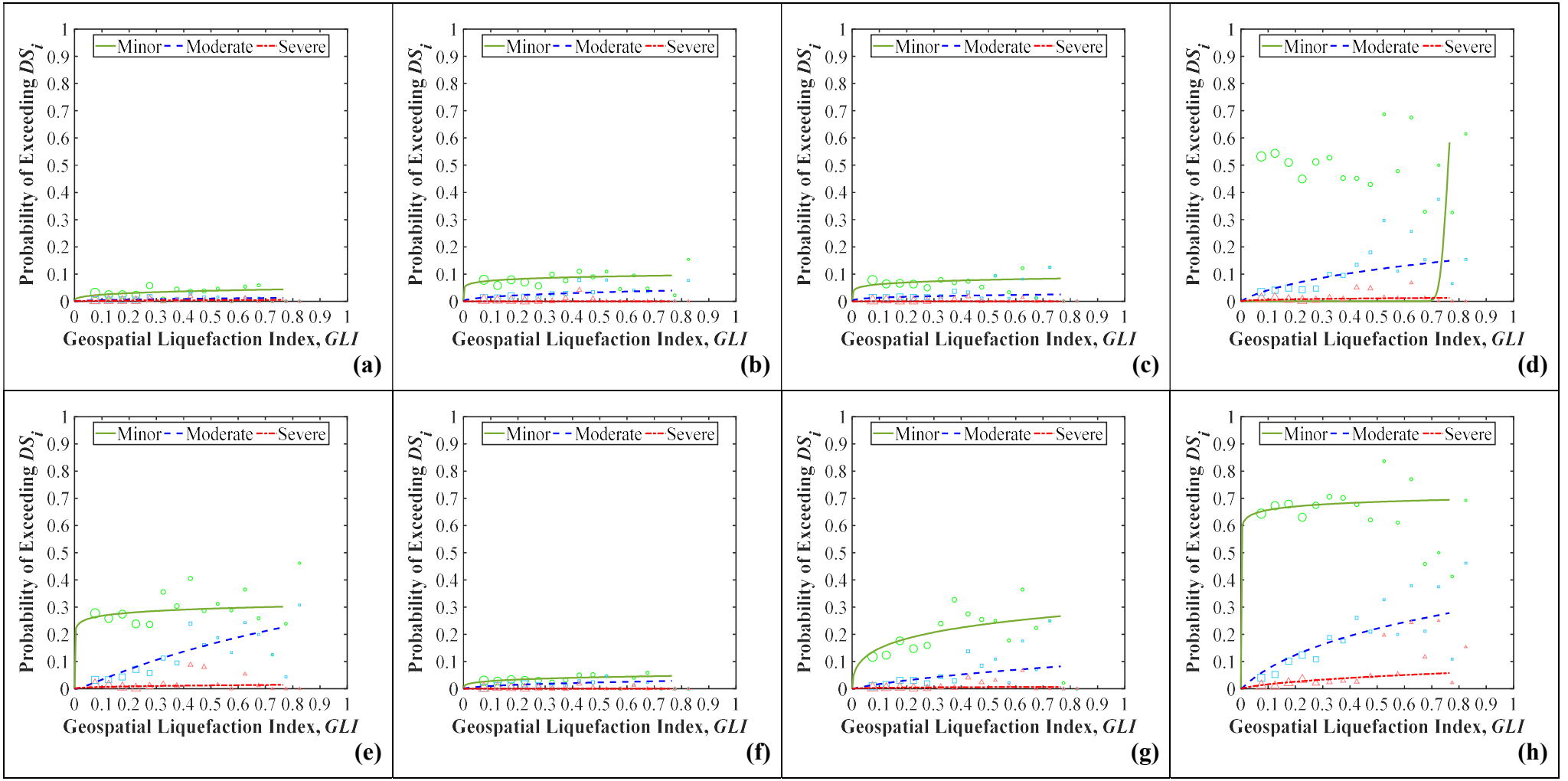

Figure 6 Fragility functions for predicting the probability of damage to Timber Floor on Pile foundations using regional geospatial model 2015 RGM3: (a) stretching failure; (b) hogging failure; (c) dishing failure; (d) twisting failure; (e) tilting failure; (f) discontinuous foundation failure; (g) global settlement failure; (h) the failure mode with greatest observed severity.

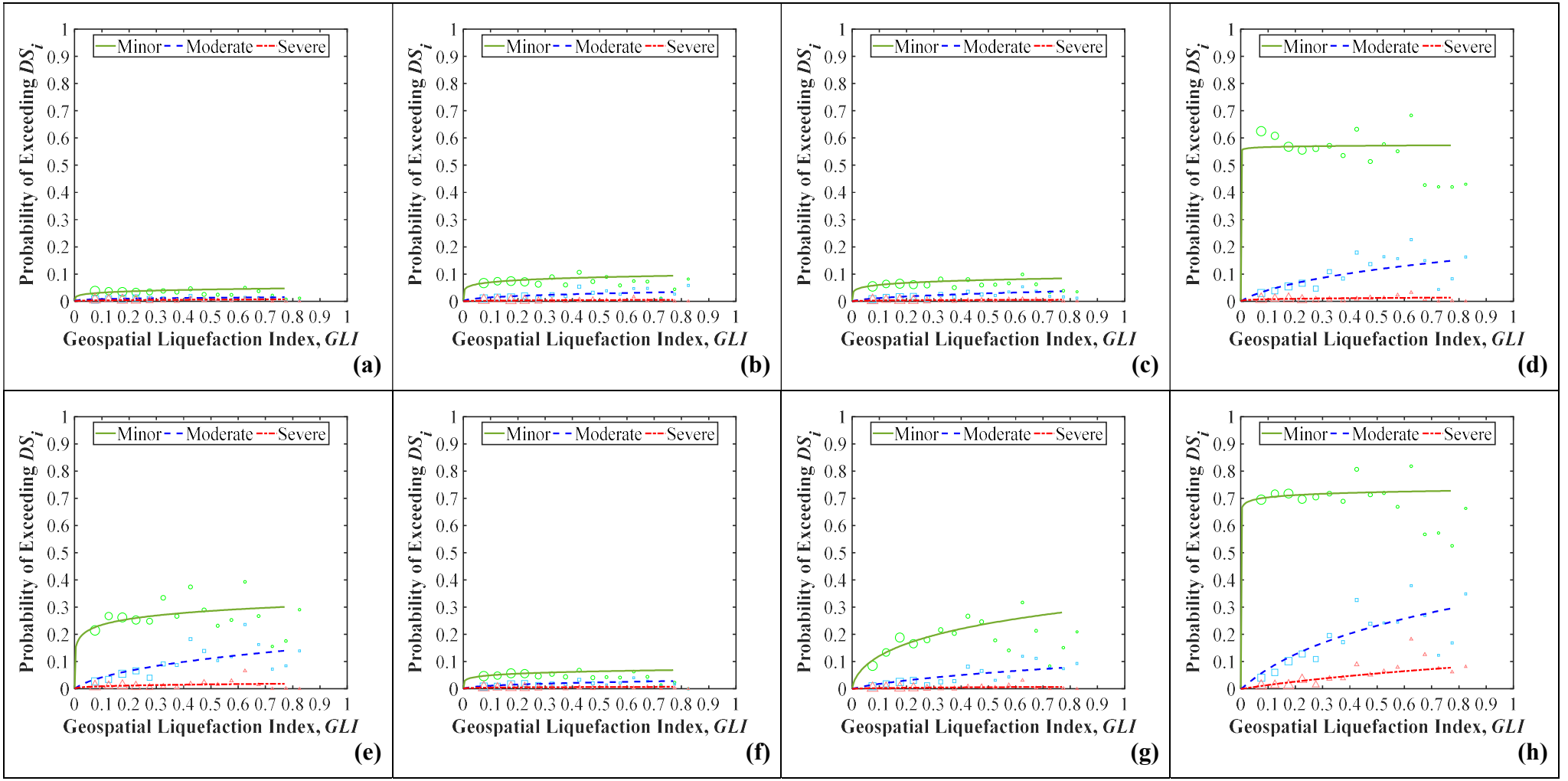

Figure 7 Fragility functions for predicting the probability of damage to Timber on Internal Piles with Perimeter Concrete Footing foundations using regional geospatial model 2015 RGM3: (a) stretching failure; (b) hogging failure; (c) dishing failure; (d) twisting failure; (e) tilting failure; (f) discontinuous foundation failure; (g) global settlement failure; (h) the failure mode with greatest observed severity.

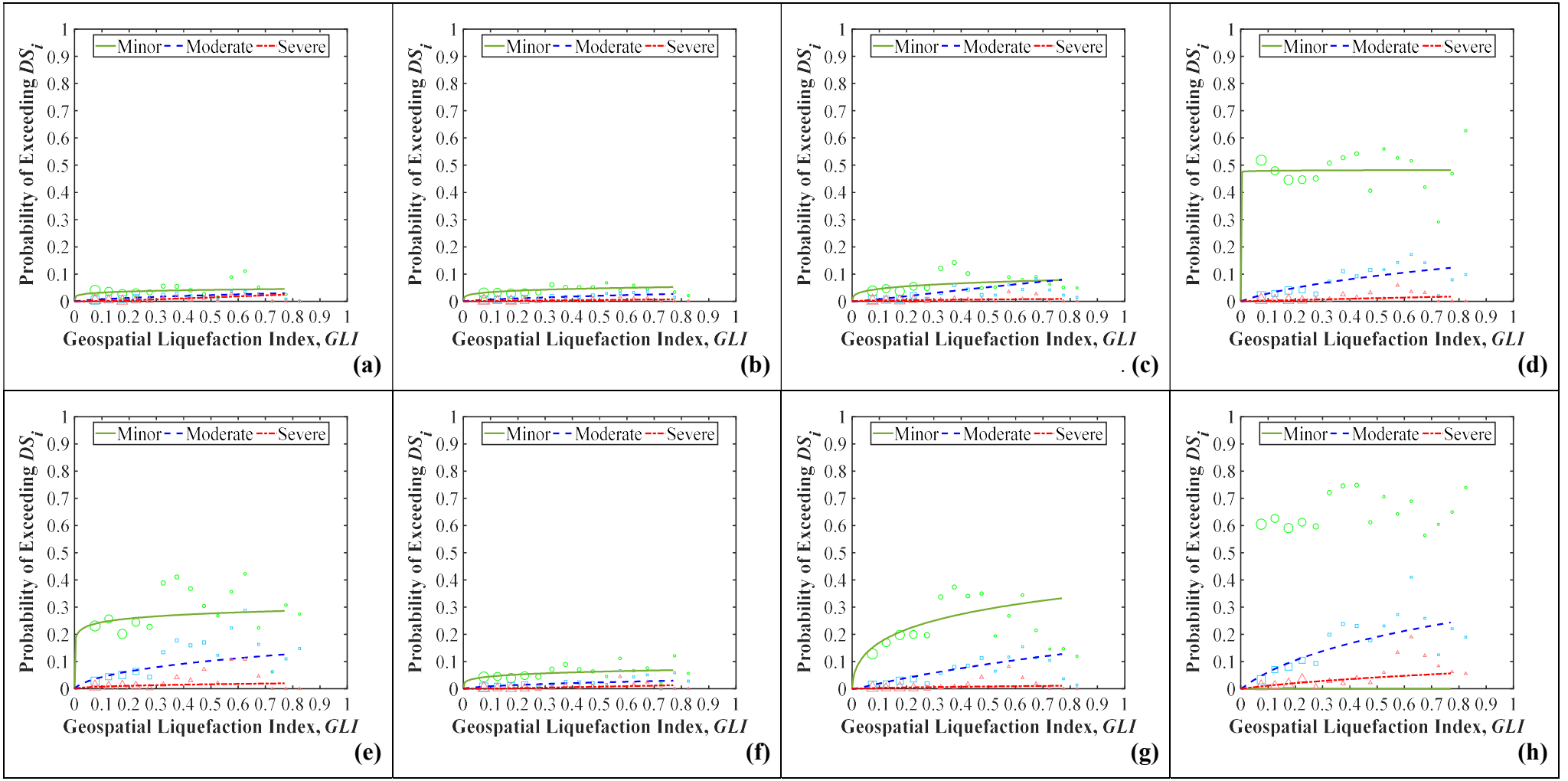

Figure 8 Fragility functions for predicting the probability of damage to Concrete Slab on Grade foundations using regional geospatial model 2015 RGM3: (a) stretching failure; (b) hogging failure; (c) dishing failure; (d) twisting failure; (e) tilting failure; (f) discontinuous foundation failure; (g) global settlement failure; (h) the failure mode with greatest observed severity.

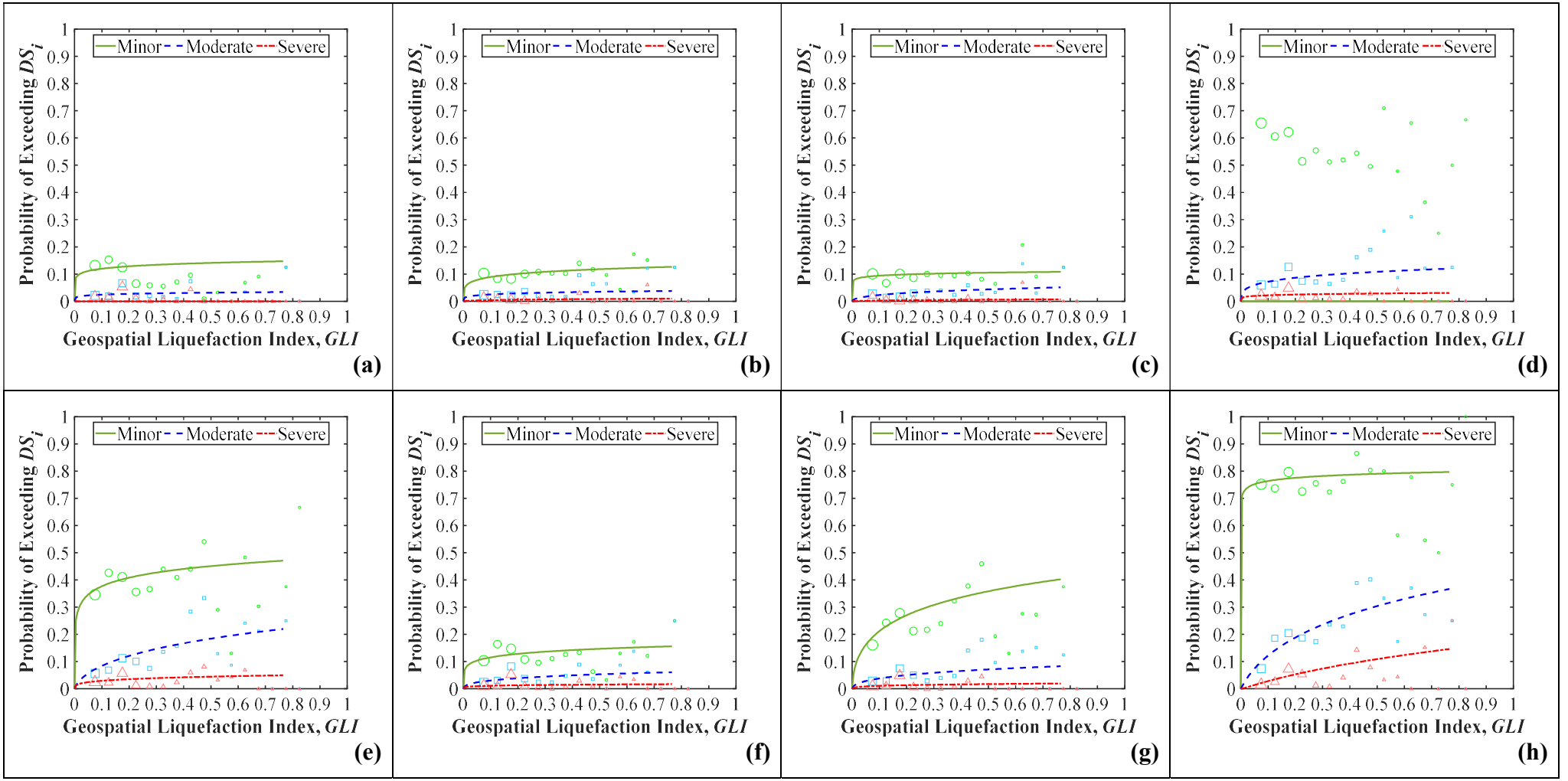

Figure 9 Fragility functions for predicting the probability of damage to Mixed foundations using regional geospatial model 2015 RGM3: (a) stretching failure; (b) hogging failure; (c) dishing failure; (d) twisting failure; (e) tilting failure; (f) discontinuous foundation failure; (g) global settlement failure; (h) the failure mode with greatest observed severity.

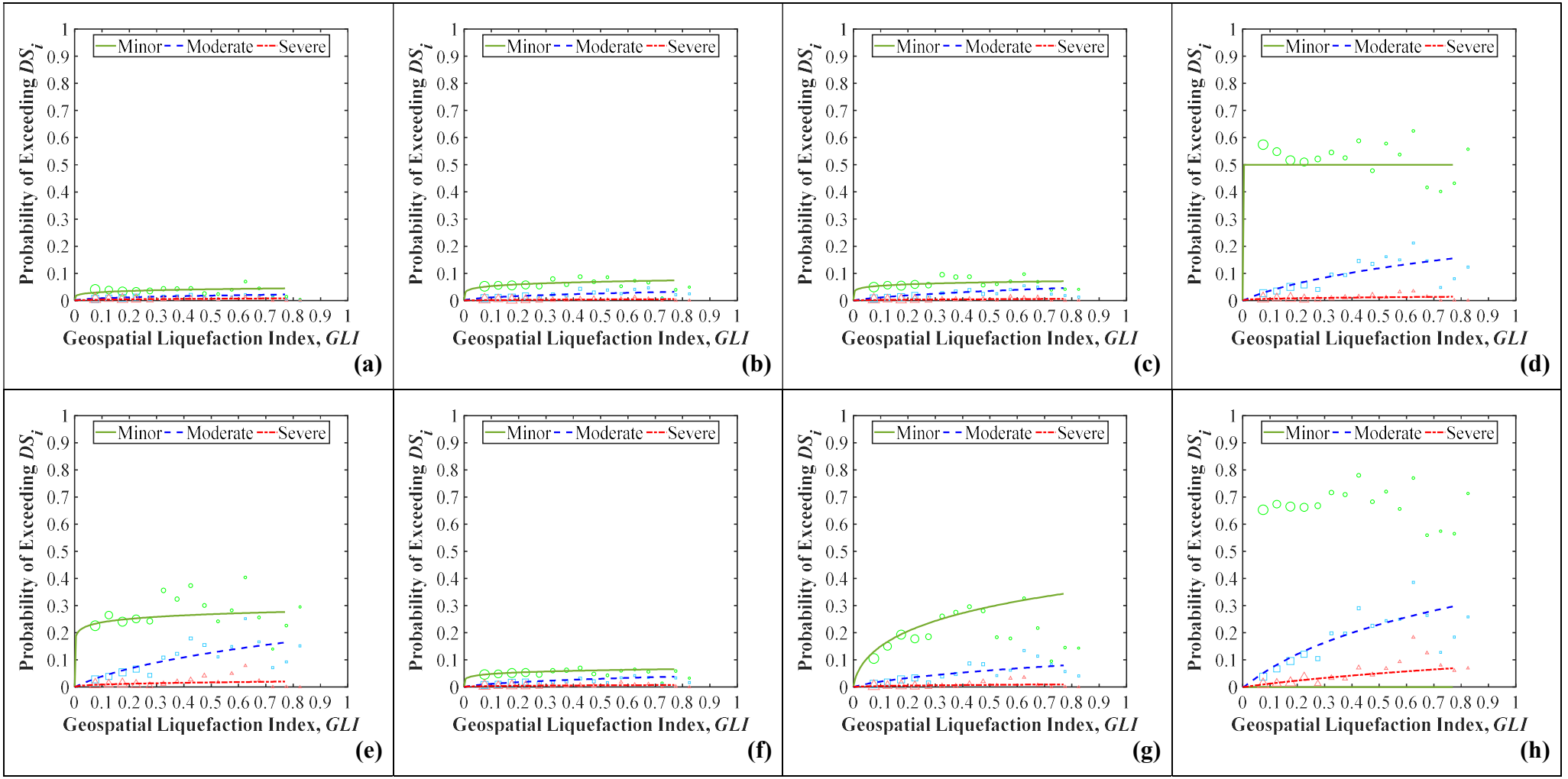

Figure 10 Fragility functions for predicting the probability of damage to shallow foundations (All variants) using regional geospatial model 2015 RGM3: (a) stretching failure; (b) hogging failure; (c) dishing failure; (d) twisting failure; (e) tilting failure; (f) discontinuous foundation failure; (g) global settlement failure; (h) the failure mode with greatest observed severity.

(2) Vulnerability Models: BDR Relations by Foundation Type

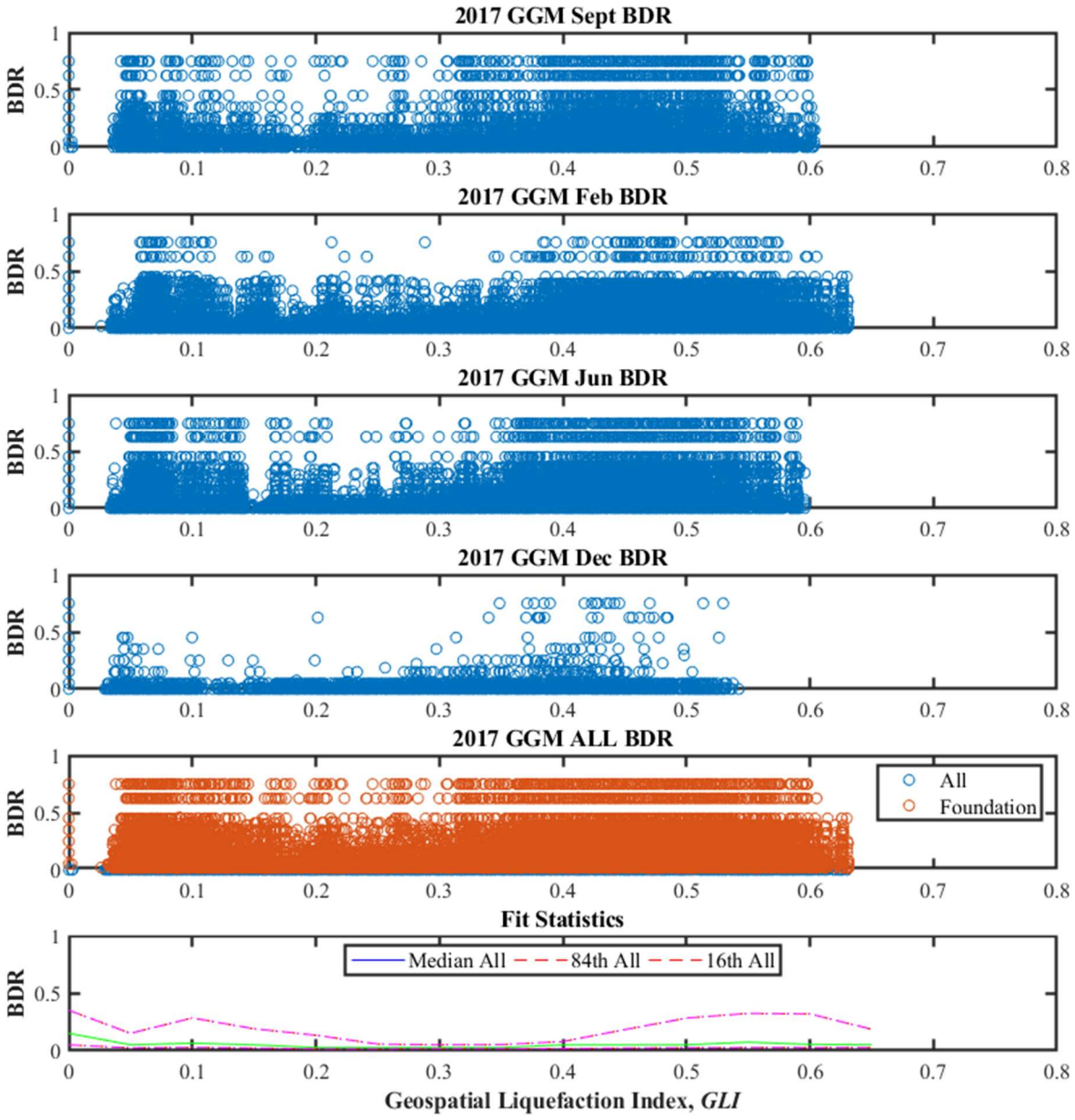

Figure 11 2017 GGM2 Building Damage Ratio data for ALL foundation types.

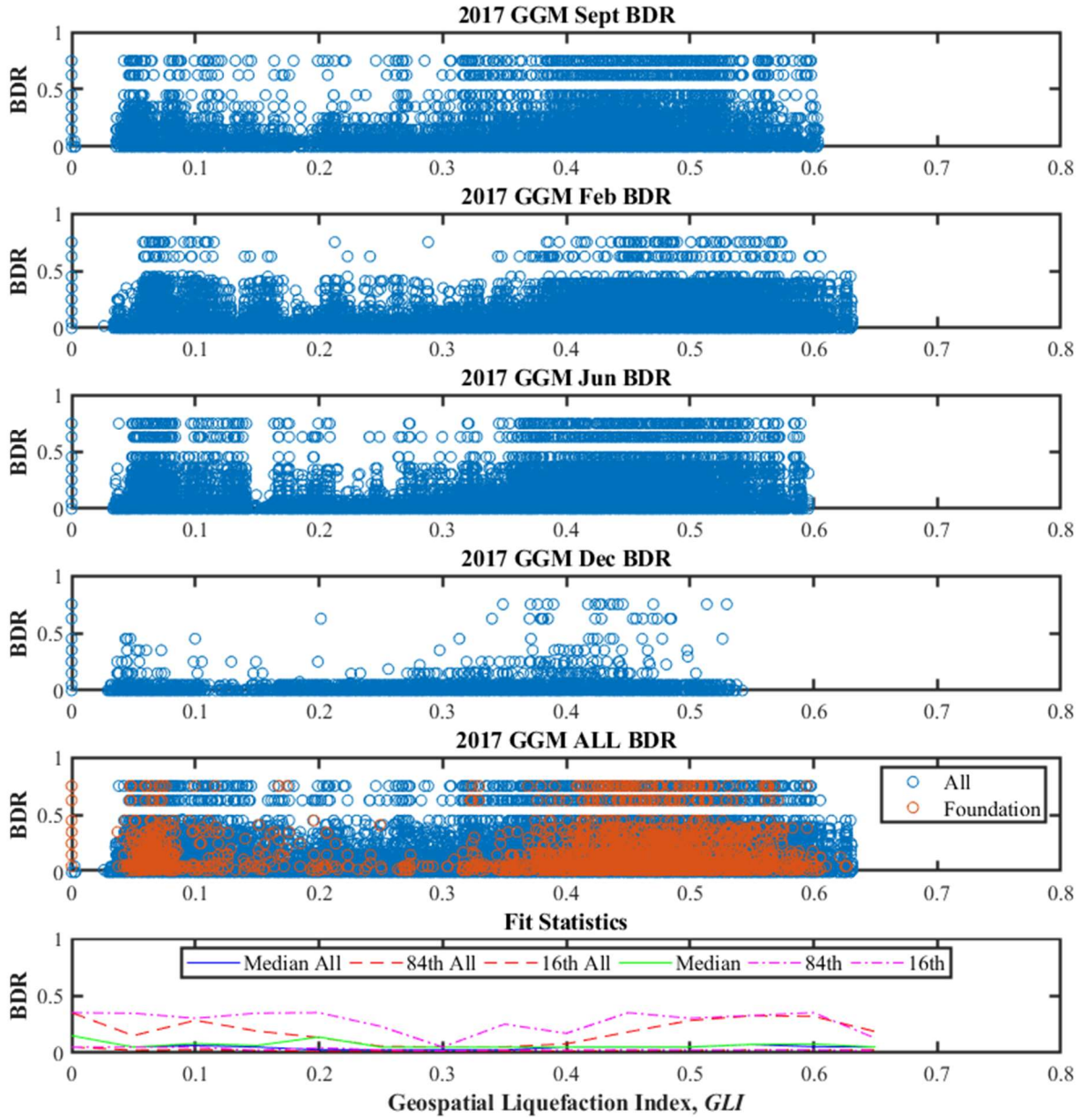

Figure 12 2017 GGM2 Building Damage Ratio data for Timber Floor on Piles foundations.

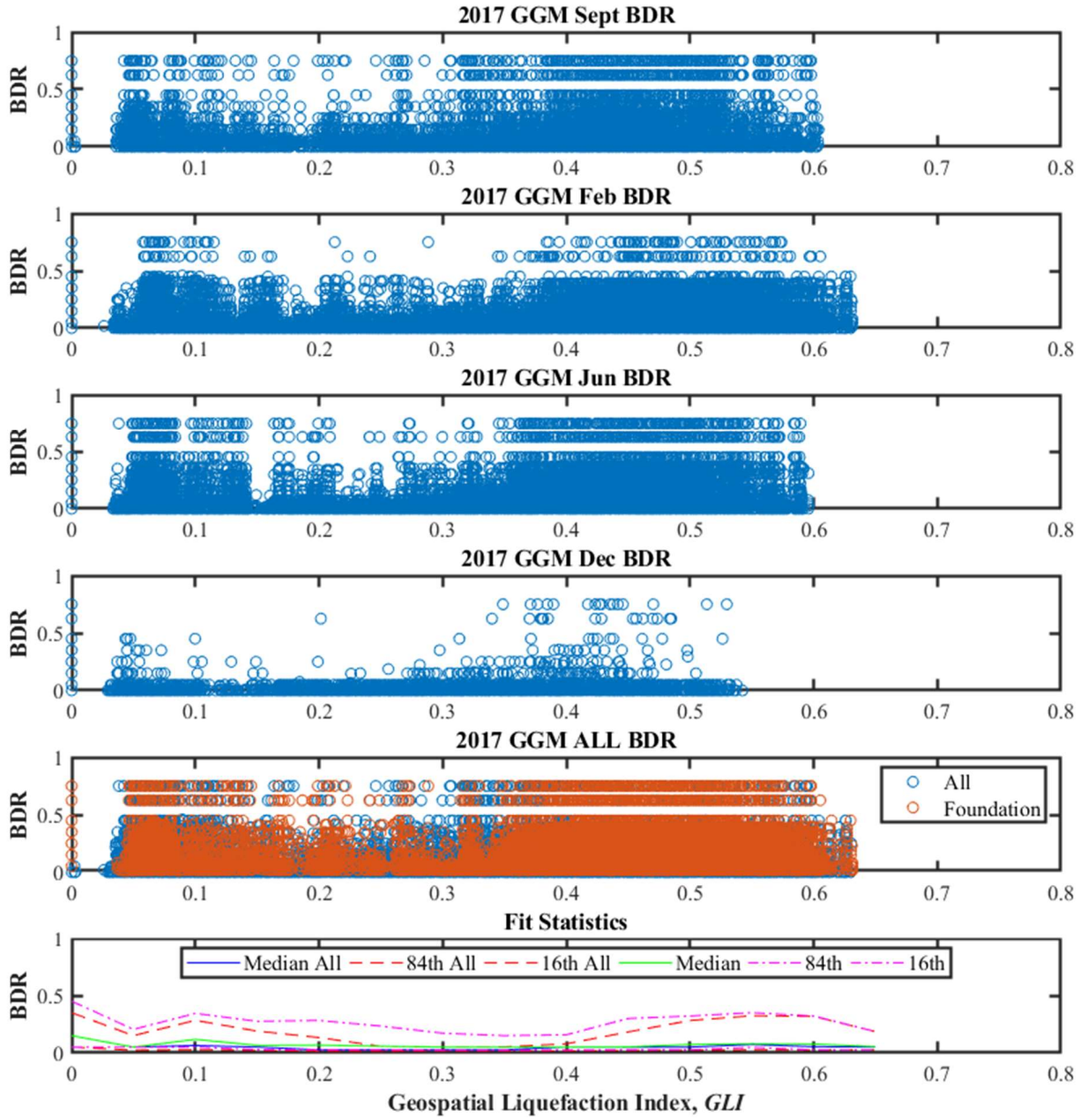

Figure 13 2017 GGM2 Building Damage Ratio data for Timber on Internal Piles with Perimeter Concrete Footing foundations.

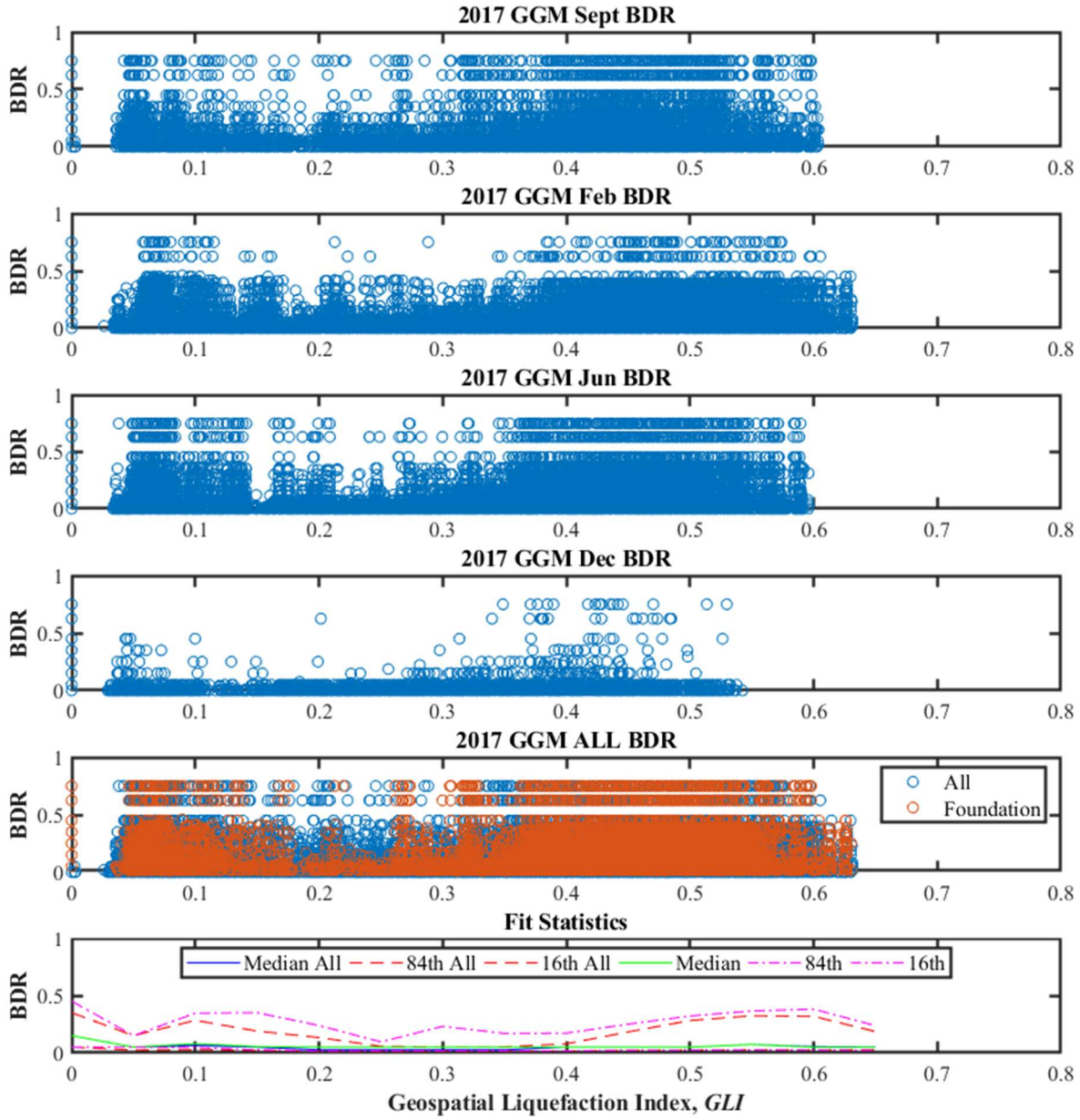

Figure 14 2017 GGM2 Building Damage Ratio data for Concrete Slab on Grade foundations.

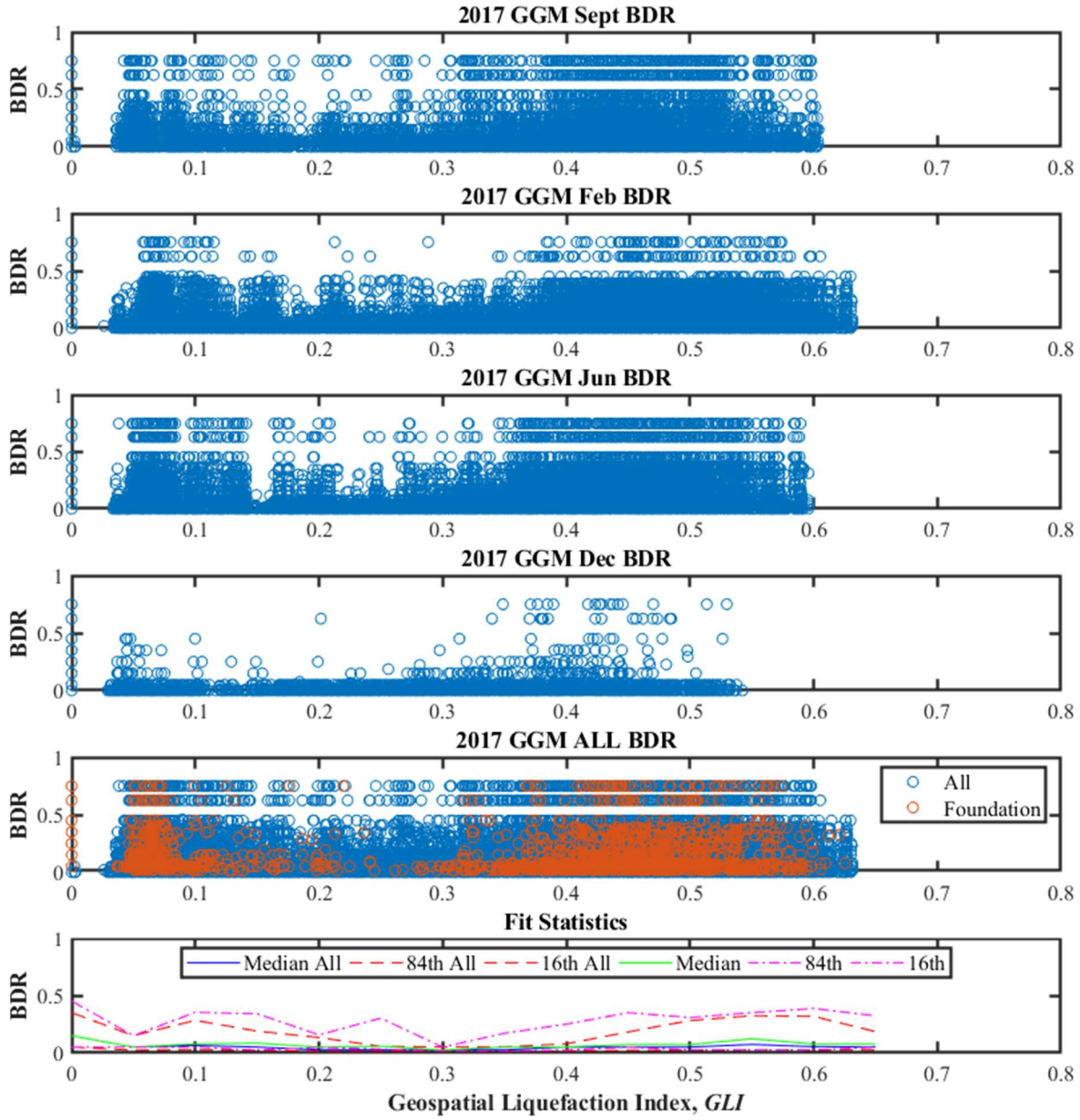

Figure 15 2017 GGM2 Building Damage Ratio data for Mixed foundations.

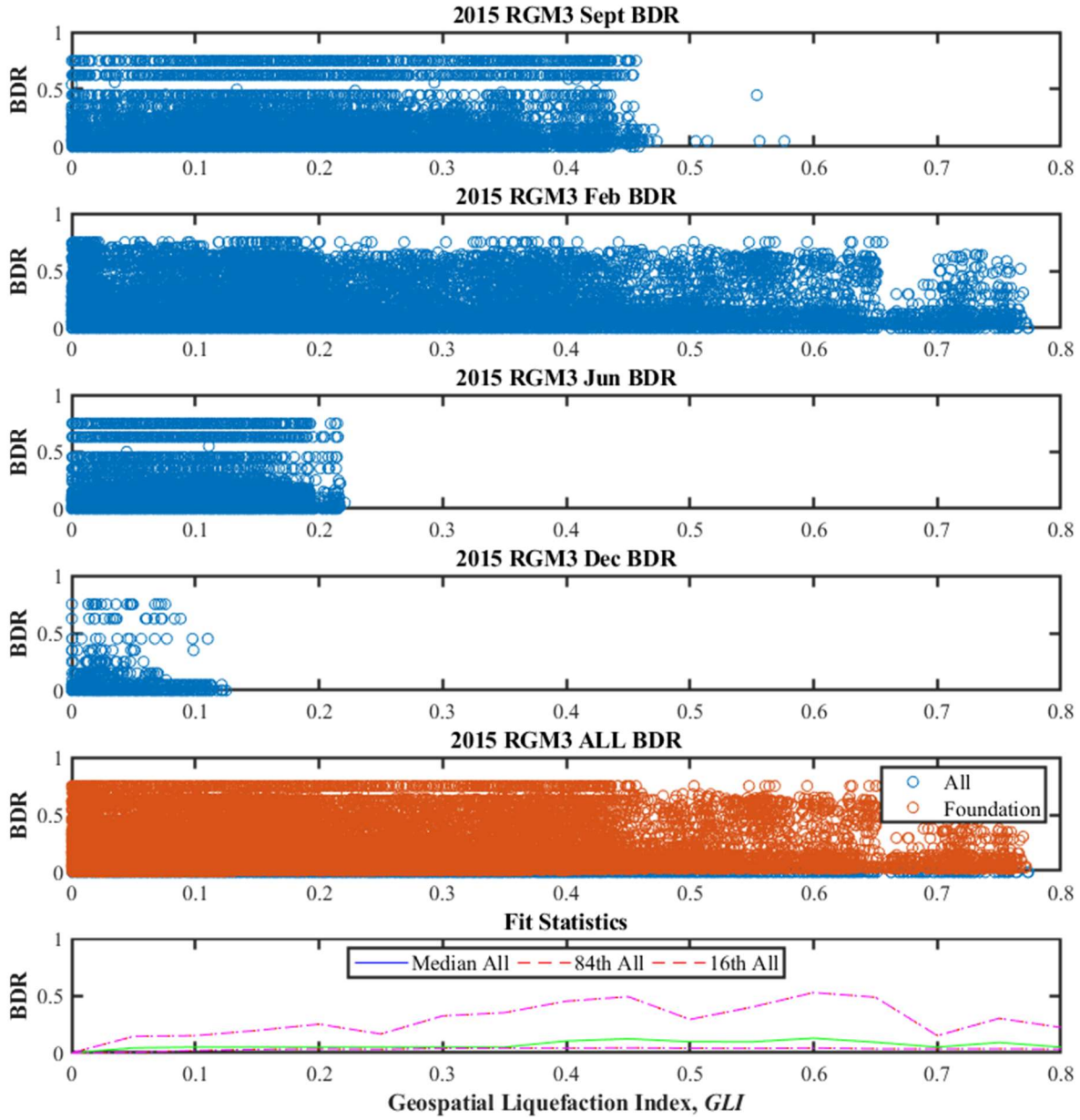

Figure 16 2015 RGM3 Building Damage Ratio data for ALL foundation types.

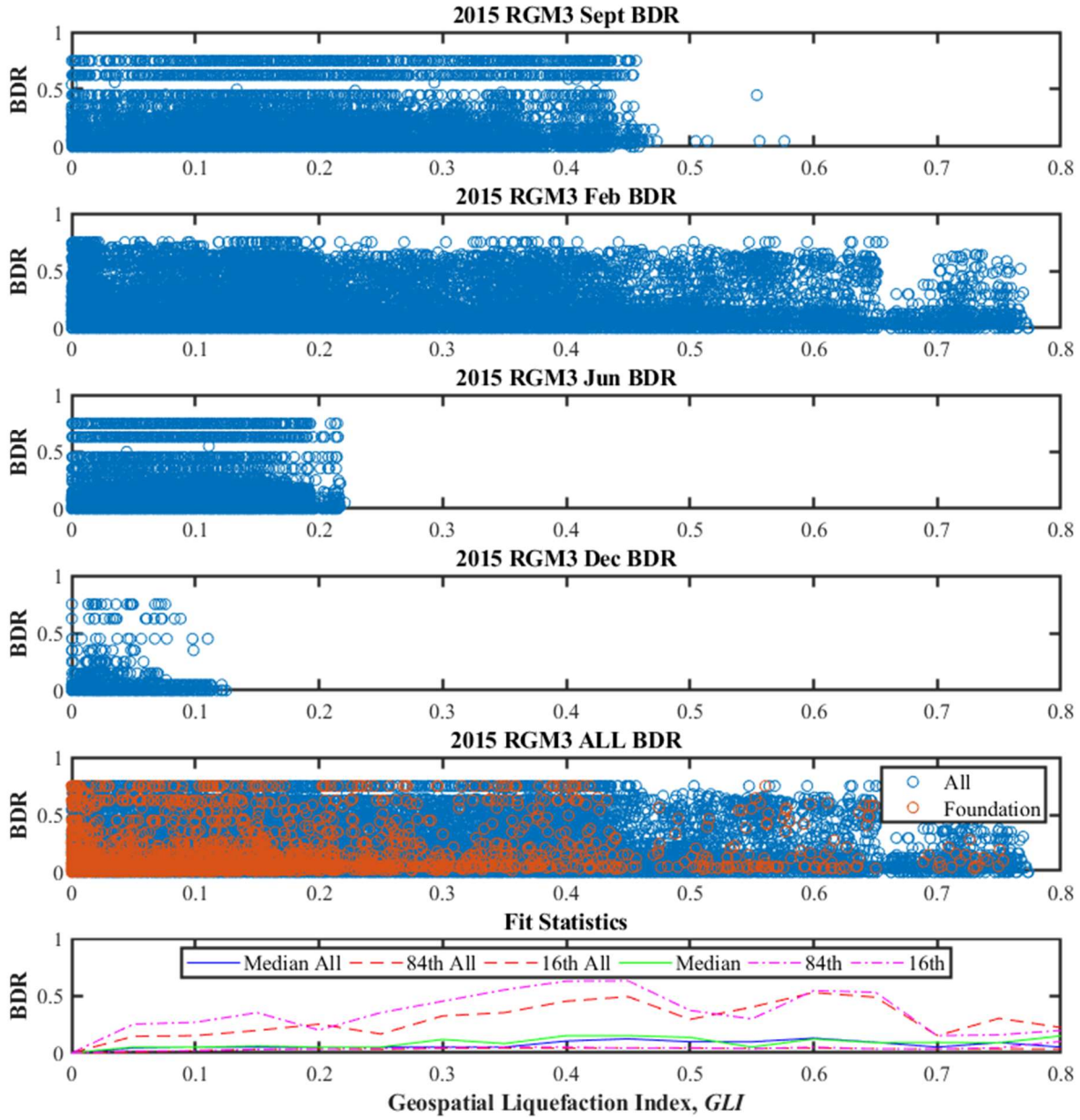

Figure 17 2015 RGM3 Building Damage Ratio data for Timber Floor on Piles foundations.

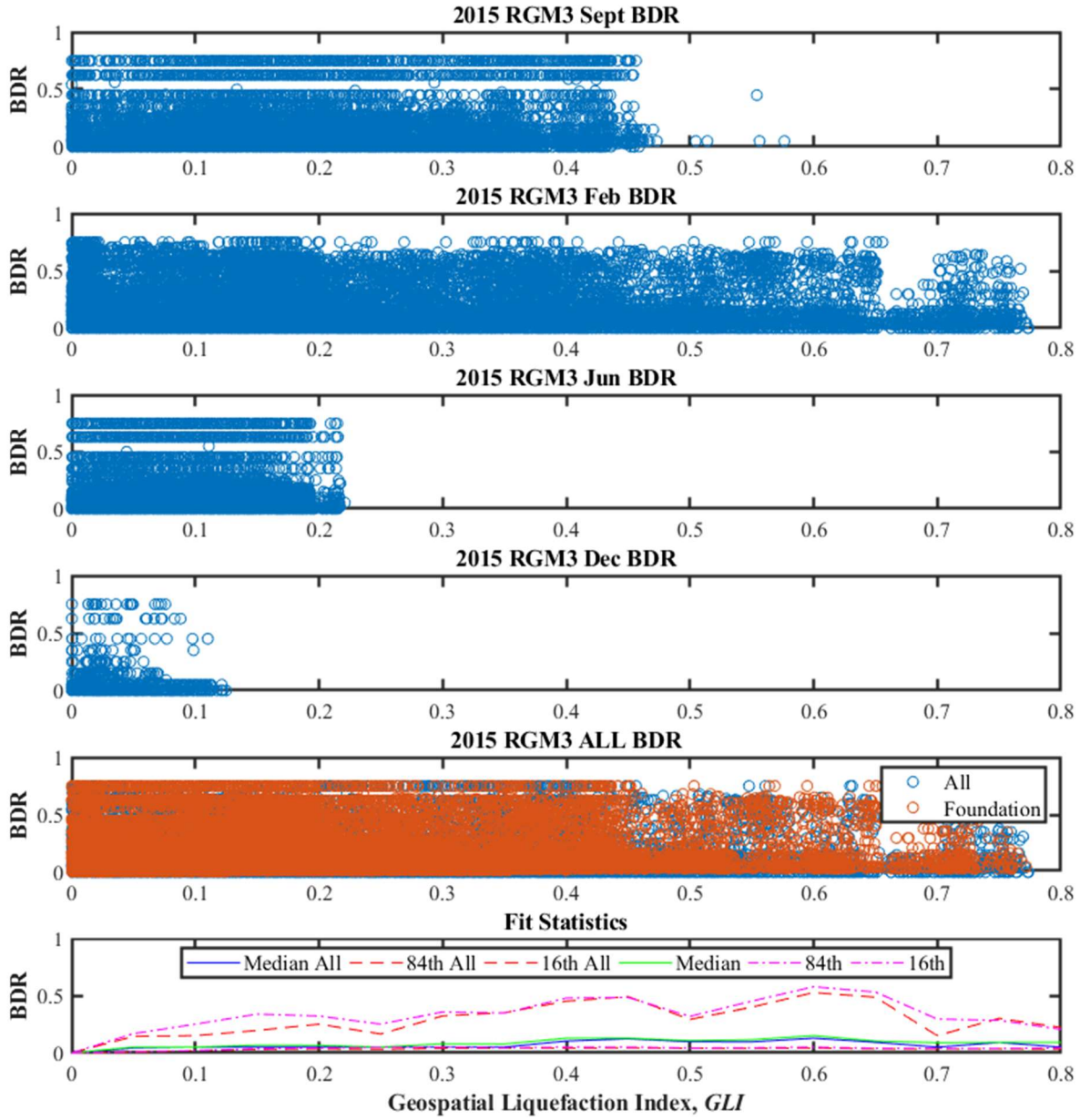

Figure 18 2015 RGM3 Building Damage Ratio data for Timber on Internal Piles with Perimeter Concrete Footing foundations.

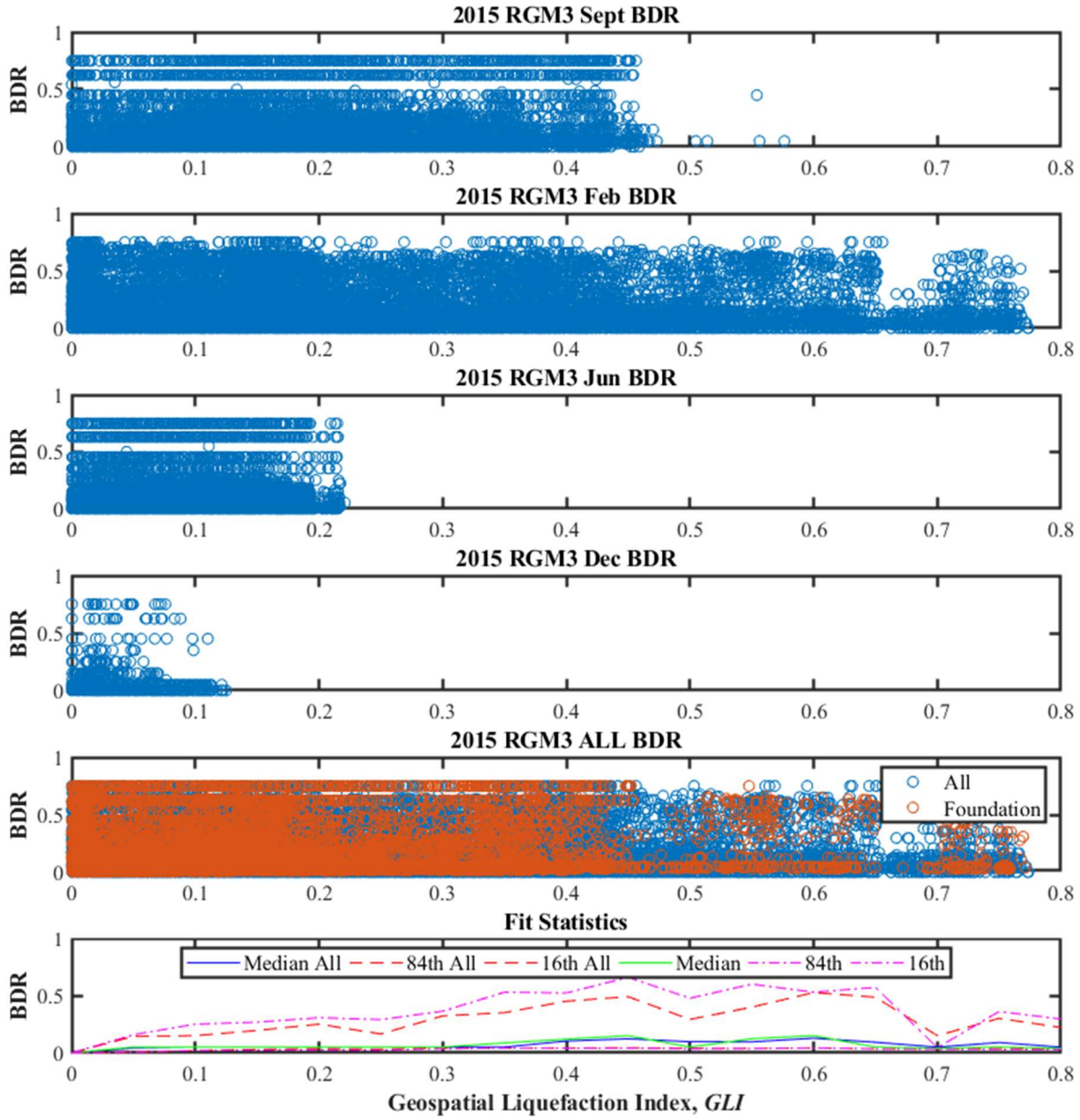

Figure 19 2015 RGM3 Building Damage Ratio data for Concrete Slab on Grade foundations.

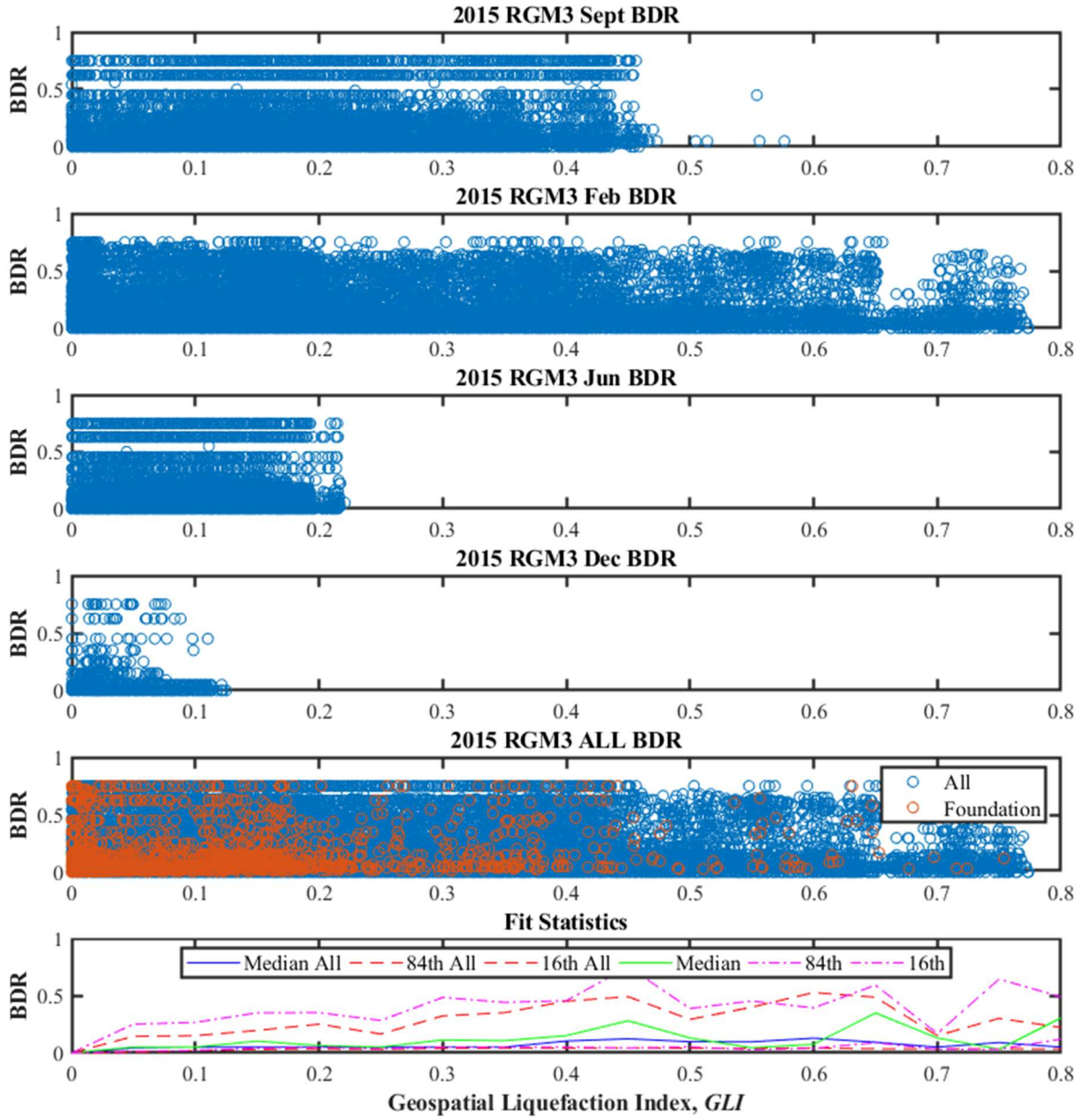

Figure 20 2015 RGM3 Building Damage Ratio data for Mixed foundations.